Effect of Shock-induced Flow Separation in Scramjet Intake at Flight Conditions

submitted in partial fulfillment of the requirements for the degree of
Doctor of Philosophy

By
Singh Rachit Surajprasad
(124010008)

Supervisor
Prof. Krishnendu Sinha

Department of Aerospace Engineering
Indian Institute of Technology Bombay

2020

Approval Sheet

This thesis entitled "Effect of Shock-induced Flow Separation in Scramjet Intake at Flight Conditions" by Singh Rachit Surajprasad is approved for the degree of Doctor of Philosophy.

Examiners

____

____

Supervisor

____

Chairman

____

Date: 03-02-2020

Place: IIT Bombay

Declaration of Authorship

I, Singh Rachit Surajprasad , declare that this report titled, "Effect of Shock-induced Flow Separation in Scramjet Intake at Flight Conditions" represents my ideas in my own words and where others ideas or words have been included, I have adequately cited and referenced the original sources. I also declare that I have adhered to all principles of academic honesty and integrity and I have not misrepresented, fabricated or falsified any idea, data, fact or source in my submission. I understand that any violation of the above will be cause for disciplinary action by the institute and can also evoke panel action from the sources which have thus not been properly cited or from whom proper permission has not been taken when needed.

Singh Rachit Surajprasad
124010008

Date: 03-02-2020

Abstract

Interaction of shock waves with turbulent boundary layers plays an important role in high-speed flows, as they can lead to flow separation, high pressure and heat transfer to the surface. Computational fluid dynamics based on Reynolds-averaged Navier-Stokes equations is routinely used in the design of hypersonic intakes. However, traditional turbulence models employed in the simulation are often inaccurate in the presence of strong shocks. The shock-unsteadiness k-ε model is specifically developed on the basis of shock physics, and is employed here to predict flow separation in hypersonic intakes at flight conditions. A two ramp mixed compression intake is considered at a design Mach number of 6 and flight altitude of 30 km. The focus is on the shock boundary layer interaction occurring at the junction of the two ramps and the resulting flow separation at the corner. The aim is to quantify the effect of flow separation on surface pressure distribution and the pressure-generated lift and drag forces on the hypersonic intake.

The work is presented in three closely-connected parts. First, the performance of the shock-unsteadiness k-ε model in eddy-viscous shock waves is studied at practically relevant conditions. Specifically, the effect of turbulent diffusion terms in the governing equation on the amplification of turbulent kinetic energy is presented. This is to extend the model, originally developed for inviscid interaction, to finite Reynolds numbers encountered in realistic flows. Second, the well-validated shock-unsteadiness model is then applied to shock-boundary layer interaction in compression corner geometry representative of the hypersonic intake. The variation of different canonical parameters, like Mach number, Reynolds number, compression corner angle and ratio of wall to recovery temperature are studied in the parameter range relevant to the intake configuration. Their effect on the size of the separation bubble and the underlying physics is explored. Third, the physical understanding is then used to analyse the effect of different flight and design parameters at on-design and off-design conditions. The flight parameters include flight Mach number, angle of attack, altitude and the design variable of the first ramp length. The variation of separation bubble size is studied and a scaling parameter to explain the effect of different flight parameters. The worst case scenario, with highest deviation in lift and drag from inviscid estimates, is identified.

Keywords : *flow-separation, shock boundary layer interactions, scramjet, compression corner, wall-temperature, Mach number, Reynolds number, flight conditions, hypersonic intakes, turbulence model, Separation bubble.*

Contents

Abstract i

Contents iii

List of Figures v

List of Tables vi

List of Abbreviations vii

List of Symbols ix

1 Introduction 1

1.1 Introduction . . . 1
1.2 Motivation . . . 3
1.3 Problem definition . . . 4
1.4 Objectives . . . 9
1.5 Outline of thesis . . . 9

2 Background 13

2.1 Scramjet geometry and orientation . . . 13
2.2 Shock waves in scramjet intakes . . . 14
2.3 Shock boundary layer interactions . . . 16
2.4 Lift and drag calculation . . . 19
2.5 Supersonic boundary layer data . . . 20
2.6 Recovery temperature . . . 22
2.7 Summary . . . 24

3 Literature review 25

3.1 Introduction . . . 25
3.2 Parameters affecting flow separation . . . 25
3.3 Prediction of separation length . . . 31
3.4 Scaling law for separation length . . . 37

3.5 Shock-turbulence interaction 39
3.6 Summary 42

4 Simulation methodology **43**
4.1 Governing equations 43
4.2 Reynolds-averaged Navier-Stokes equations 44
4.3 Turbulence closure 46
4.4 Numerical method 49
4.5 Boundary conditions 54
4.6 Summary 56

5 Amplification of turbulence across eddy-viscous shock waves **57**
5.1 Introduction 57
5.2 Methodology 59
5.3 Non-conservative formulation 60
5.4 Conservative formulation 64
5.5 Effect of diffusion terms 67
5.6 Analysis of diffusion terms 70
5.7 Summary 73

6 Physics of flow separation due to shock waves **75**
6.1 Introduction 75
6.2 Methodology 75
6.2.1 Computational domain 77
6.2.2 Grid-convergence 78
6.2.3 Validation 79
6.3 Effect of ramp angle 81
6.4 Effect of wall temperature 84
6.5 Effect of Mach number 88
6.6 Effect of Reynolds number Re_δ 91
6.7 Summary 95

7 Effect of flow separation in hypersonic intakes **97**
7.1 Introduction 97
7.2 Effect of flight Mach number 100
7.3 Effect of first ramp length 104
7.4 Effect of angle of attack 108
7.5 Effect of altitude 111

7.6 Overall analysis of scaling parameter 115
7.7 Summary 116

8 Conclusions 119
8.1 Conclusions 119
8.2 Contributions 120
8.3 Future work 121

A Averaging 6
A.1 Reynolds averaging 6
A.2 Favre averaging 7

B Jacobian Matrices 8

C Skin-friction Force in Intake 10
C.1 Introduction 10
C.2 Literature 11
C.3 Predictions 13
C.4 Summary 15

D Effect of flow-properties 16
D.1 Effect of temperature 16
D.2 Effect of density 19
D.3 Effect of pressure 19

E Analysis of diffusion terms 20

Bibliography 25

Acknowledgements 32

List of Figures

1.1 Components of scramjet engine 1
1.2 Schematic of ramp shocks (dotted lines) formed in the intake of a scramjet engine. 2
1.3 Intake of a scramjet engine and zoomed view shows the schematic of the separation bubble formed at the corner between the two ramps. 4
1.4 Schematic of a scramjet intake flow satisfying the shock-on-lip condition. 5
1.5 Canonical parameters affecting flow separtion over a compression corner geometry. 7
1.6 Supersonic flow over a normal shock wave. 8
1.7 Overview of the work. 11

2.1 Shock interacting with boundary layer at the corner in intake of scramjet engine 13
2.2 Schematic of intake of scramjet engine 14
2.3 The typical scramjet flow path [3]. 15
2.4 (a) Schematic and (b) schlieren image [19] of supersonic flow over a compression corner geometry. 15
2.5 (a) Schematic and (b) schlieren image [19] of supersonic flow over a shock impinging on a flat plate. 16
2.6 Weak interaction due to shock interacting with boundary layer [19]. . . . 16
2.7 Strong interaction due to shock interacting with boundary layer and formation of separation bubble [19]. 17
2.8 Pressure distribution for (a) weak interaction and (b) strong interaction [19]. 18
2.9 Schematic of comparison of inviscid vs CFD predicted pressure distribution over two ramp surfaces and pressure P_i acting over a element of length dx_i inclined at angle θ_i 19
2.10 M_t and Re_t variation in supersonic boundary layer. 22
2.11 Heat transfer for different wall-to-recovery temperature ratios [24]. 23

3.1 Wall-pressure distribution showing an increased upstream influence with a plateau and an overshoot in pressure for separated flows in experiments of Elfstrom et al. [29] at M = 9.22. 27
3.2 Schematic of cylinder-flare geometry 28
3.3 Variation of upstream influence with Reynolds number in experiments of Settles et al [33]. 28
3.4 Effect of wall-to-recovery-temperature ratio (s) on wall pressure (top) and skin-friction (bottom) for M = 2.28 simulations of Bernardini et al [38]. . 30
3.5 Pressure distribution as predicted by standard k-ω turbulence models in simulations for supersonic flow over compression ramp by (a) Pasha et al. [45] and (b) Gnoffo et al. [46]. 31
3.6 Surface pressure prediction using standard and shock-unsteadiness modified turbulence model [18] for supersonic flow over a compression corner geometry [17]. 32
3.7 Wall pressure computed using (a) shock-unsteadiness modified Spalart-Allmaras model and (b) shock-unsteadiness k-ω turbulence model is compared with experimental data [50] for 36° flare at Mach 13.1 [51]. 33
3.8 Computed (a) wall pressure and (b) skin friction coefficient compared with experimental data [52] for $\theta = 10^{\circ}$ at M = 5 using standard k–ω and shock- unsteadiness modified k–ω models, ... 34
3.9 (a)Schematic of scramjet intake and (b) pressure contour of flow inside duct where separation is formed [53]. 35
3.10 (a) Pressure and (b) skin-friction distribution over the surface of intake where separation is formed [53]. 36
3.11 Definition of interaction length L_{int} for compression corner geometry . . . 38
3.12 Normalized separation length $L^{\star}$ versus shock-strength $S_e^{\star}$; colors represent the separation state: black - attached; gray - incipient; white - separated 39
3.13 Schematic of evolution of turbulent kinetic energy k across a normal shock (a) before the normalization and (b) after the normalization 41

4.1 Discretization of the domain using cell centers (shown as circle) and cell interfaces (shown as a dotted line). 54
4.2 Boundary conditions applied to inlet, exit/outlet, top and wall at bottom of the computational domain. 55

5.1 Flow over a normal shock obtained by taking the normal components of flow over a oblique shock. 57

5.2 Schematic of evolution of turbulent kinetic energy k across a normal shock. . . . 58
5.3 Schematic of cell-centers and cell-faces at the 1D grid used in RANS simulations. . . . 59
5.4 Evolution of turbulent variables k and ε across a normal shock (located at X = 0) for M = 1.5 (a, b) and M = 2.5 (c, d). . . . 61
5.5 Amplifications in turbulent variables k and ε for a range of Mach numbers. 62
5.6 Effect of grid refinement on evolution in turbulent variables k and ε for M = 2.5. . . . 63
5.7 Effect of grid refinement on amplification of turbulent variables k and ε across a normal shock for a range of Mach numbers. . . . 63
5.8 Evolution of k and ε across a normal shock for M = 1.5 (a, b) and M = 2.0 (c, d). . . . 65
5.9 Amplifications in turbulent quantities k and ε for a range of Mach numbers. 66
5.10 Effect of grid refinement on evolution of k and ε across a normal shock. . 67
5.11 Effect of grid refinement on amplifications in k and ε for a range of Mach numbers. . . . 67
5.12 Effect of diffusion terms on k and ε profile across a normal shock for M = 1.5 (a, b) and M = 2.5 (c, d) . . . 69
5.13 Effect of diffusion terms on k and ε amplification across a normal shock for different Mach numbers. . . . 70
5.14 Effect of grid refinement on k and ε profile across a normal shock for M = 2.5. . . . 70
5.15 Effect of grid refinement on k and ε amplifications across a normal shock at different Mach numbers for simulations done with the turbulent diffusion terms. . . . 71
5.16 Difference in amplification in turbulent kinetic energy $\Delta k_2/k_1$ across shock showing the effect viscous/turbulent diffusion terms . . . 72
5.17 Difference between inviscid and viscous amplifications of the turbulent variables k and ε for a range of Re_t/Re . . . 73
5.18 Difference between inviscid and viscous amplifications of the turbulent variables k and ε for a range of Re_t/Re using different grid points. . . . 74

6.1 Skin-friction and wall-pressure distribution over the compression corner geometry. . . . 76
6.2 Schematic of (a) supersonic flow over compression corner geometry and (b) computational domain with the grid. . . . 77

6.3 (a) Wall pressure and (b) skin-friction distribution for different ramp lengths. Corner shifted to $X = 0$ location. 78
6.4 Wall-pressure and skin-friction distribution for different grids in stream-wise (a,b) direction and in wall-normal (c,d) direction. 79
6.5 Comparison of (a) computed wall-pressure and (b) skin-friction distribution with the experimental data of Settles et al. [48] for $\theta = 24$ degree case. 80
6.6 Comparison of computed (a) wall-pressure and (b) skin-friction distribution with the computational results of Sinha et al. [17] 81
6.7 Variation in (a) wall-pressure distribution, and (b) skin-friction distribution for different ramp angles. 82
6.8 Normalized separation length obtained for ramp angles plotted against the normalized shock-strength using the scaling law proposed by Souverein et al [56], and its best curve fit equation. 83
6.9 (a) Variation in wall-pressure distribution, and (b) movement of the separation and re-attachment points for different wall-to-recovery-temperature ratios. 85
6.10 Normalized separation length obtained for different wall-temperatures plotted against the normalized shock-strength using the scaling law propsed by Souverein et al [56], and its best curve fit equation. 85
6.11 Variation of (a) near-wall viscosity (Pa.s) and (b) near-wall density (kg/m^3) in wall-normal direction for different wall temperatures. 86
6.12 Shifting of the sonic line away from the wall for different wall temperatures. 87
6.13 Variation in (a) wall-pressure distribution, and (b) normalized separation length for different Mach numbers. 89
6.14 Normalized separation length obtained for different Mach numbers plotted against the normalized shock-strength using the scaling law proposed by Souverein et al [56], and its best curve fit equation. 90
6.15 (a) Shifting of sonic lines and (b) changes in near-wall density for different Mach numbers. 90
6.16 Variation in (a) wall-pressure and (b) skin-friction distribution for different Reynolds number Re_δ. 92
6.17 Normalized separation length obtained for different Re_δ plotted against the normalized shock-strength using the scaling law proposed by Souverein et al [56], and its best curve fit equation. 93

6.18 (a) Shifting of the sonic line, (b) the variation in separation length, (c) variation in the displacement boundary layer thickness $\delta^{\star}$ and (d) variation of the normalized separation length for different Reynolds number Re_{δ}. 94

6.19 Canonical parameters affecting the separation length for supersonic flow over a compression ramp geometry. 96

7.1 Schematic of scramjet intake and the flight parameters varied. 98

7.2 Intake of scramjet engine, rotated in clock wise direction such that first ramp is horizontal to incoming flow, showing the weak boundary layer (leading edge) shock formed at the first ramp. 99

7.3 Pressure distribution (inviscid vs CFD) plotted using two different approach: (a) shows the effect of boundary layer shock at first ramp as well as the second ramp shock induced separation and (b) shows only the effect of second ramp shock induced separation. 100

7.4 Variation in (a) wall-pressure distribution, (b) skin-friction distribution, (c) movement of separation and re-attachment points from corner, and (d) normalized separation length for different flight Mach numbers. 102

7.5 Percentage change in lift or drag forces acting on the two ramps for different flight Mach numbers. 104

7.6 (a) wall-pressure distribution and (b) changes in location of separation and reattachment points from the corner for different lengths of first ramp. 106

7.7 Percentage change in lift or drag forces acting on the two ramps for different lengths of first ramp. 107

7.8 Schematic of scramjet intake subjected to positive (up), negative (down) and zero (dotted arrow) angles of attacks. 108

7.9 Variation in (a) wall-pressure distribution and (b) movement of separation and re-attachment points from corner for different angles of attack. 109

7.10 Percentage change in lift or drag forces acting on the two ramps for different angles of attack. 111

7.11 Variation in (a) wall-pressure distribution, (b) skin-friction distribution, and (c) normalized separation length for different altitudes. 113

7.12 Percentage change in lift or drag forces acting on the two ramps for different altitudes. 114

8.1 Schematic of PIV setup for fin induced shock wave boundary layer interaction [72]. 4

C.1 Variation of skin-friction coefficient over the flat plate boundary layer . . 10
C.2 Comparison of analytical (Van Driest) skin-friction with the CFD results over the first ramp. 13
C.3 Contribution of skin-friction generated force to the total force acting on the intake over the two ramps under different flight condtions. M_1 - flight Mach number, L1 - first ramp length, α - angle of attack, and z - altitude. 14

D.1 Supersonic flow separtion over a compression corner geometry. 16
D.2 Variation in (a) wall-pressure distribution, (b) skin-friction distribution, (c) movement of separation and re-attachment points from corner, and (d) normalized separation length - for different temperatures. 17
D.3 Variation of (a) wall-pressure distribution, (b) skin-friction distribution, (c) movement of separation and re-attachment points from corner, and (d) normalized separation length - for different densities. 18

List of Tables

1.1 On and Off-design values used for the study of flight parameters affecting flow separation. 6
1.2 Values of canonical parameters varied to study the effect of flow separation over a compression corner geometry. 8

2.1 Flow variables corresponding to $Re_{t,max}$ values obtained from boundary layer data at different locations on flat-plate. 21

3.1 Details of DNS data corresponding to various Mach number used in validation [12]. 40

5.1 Details of DNS data corresponding to various Mach number used in validation [12]. 60
5.2 Flow parameters from RANS solution of flat-plate boundary layer at different locations (in m) downstream of the plate tip. 72

6.1 Range of flow parameters considered for compression corner simulations to study the effect of given parameter. 76
6.2 Pressure jump across the shock for different ramp angles. 84
6.3 Changes in wall-to-recovery temperature ratio for different wall temperatures. 88
6.4 Different ratios across the shock for different Mach numbers. 91
6.5 Variation of normalized separation length with respect to various parameters. 95

7.1 On and Off-design parameters for the study of flight parameters affecting flow separation. 98
7.2 Effect of varying the flight Mach number M_1 on flow parameters at station-2. 101
7.3 Changes in scaling parameter for different flight Mach numbers. 103
7.4 The second ramp angle θ_2 required for different first ramp lengths to satisfy the shock-on-lip condition 105

7.5 Effect of varying the first ramp length L1 on the conditions at station-2. . 105
7.6 Changes in scaling parameter for different lengths of first ramp. 107
7.7 Conditions at station-1 (free-stream) and station-2 for different angles of attack. 108
7.8 Conditions to be used for ramp simulations to study effect of angle of attack. 109
7.9 Changes in scaling parameter different angles of attack. 110
7.10 The properties of air - pressure, temperature, density - at different altitudes in atmosphere. 111
7.11 The changes in conditions at station-2 with increase in altitide. 112
7.12 Variation in scaling parameter with altitude. 113
7.13 The variation in separation length and the scaling parameter with different flight parameters. 116

List of Abbreviations

DNS	**D**irect **N**umerical **S**imulations
LES	**L**arge **E**ddy **S**imulations
BL	**B**oundary **L**ayer
SBLI	**S**hock Boundary **L**ayer **I**nteractions
STI	**S**hock **T**urbulence **I**nteraction
RANS	**R**eynolds **A**veraged **N**avier **S**tokes
TKE	**T**urbulent **K**inetic **E**nergy
FTCS	**F**orward in **T**ime **C**entered in **S**pace
LHS	**L**eft **H**and **S**ide
RHS	**R**ight **H**and **S**ide
NTP	**N**ormal **T**emperature **P**ressure
SA	**S**palart and **A**llmaras
SU	**S**hock **U**nsteadiness
ISRO	**I**ndian **S**pace **R**esearch **O**rganization
BLT	**B**oundary **L**ayer **T**hickness
SLT	**S**onic **L**ayer **T**hickness
VSL	**V**iscous **S**ub **L**ayer
CFD	**C**omputational **F**luid **D**ynamics

List of Symbols

p	pressure	Pa
E	Energy	J
H	Enthalpy	J
q	Heat/Heat-flux	J
P_0	Stagnation Pressure	Pa
M	Mach Number	
M_t	Turbulent Mach Number	
K_0	Wave Number	
a, c	Speed of sound	$\mathrm{m\,s^{-1}}$
$\dot{m}$	Mass-flow rate	$\mathrm{kg/m^3}$
x, X	Distance along x-direction	m
y, Y	Distance along y-direction	m
L	Intake length	m
H	Intake height	m
H_c	Height of duct/combustor	m
$L1$	Length of first ramp	m
$L2$	Length of second ramp	m
C_f	Skin-friction co-efficient	
T_w	Wall-temperature	$^\circ$K
T_r	Relaxation wall-temperature	$^\circ$K
T_∞	Free-stream temperature	$^\circ$K
X_s	Location of separation point	m
X_r	Location of re-attachment point	m
L_{sep}	Length of separation bubble	m
z	Altitude	km
ρ	density	$\mathrm{kg/m^3}$
τ	shear-stress	$\mathrm{Pa\,s}$
μ	Viscosity	$\mathrm{Pa\,s}$
δ	Boundary layer thickness	m
$\delta^\star$	Displacement boundary layer thickness	m

k	Turbulent Kinetic Energy	J
ε	Dissipation rate	m^2/s^3
λ	Taylor Length Scale	m
κ	Thermal conductivity	$Wm^{-1}K^{-1}$
Re_λ	Reynolds Number based on Taylor micro-scale	
Re_t	Turbulent Reynolds Number	
Re_L	Characteristic Reynolds Number	
Re_δ	Reynolds Number based on δ	
Re_θ	Reynolds Number based on momentum thickness θ	
θ	Ramp angle	$\circ$
β	Shock angle	$\circ$
subscripts		
∞	free-stream	
1	station-1	
2	station-2	
3	station-3	
t	turbulent	
ref	reference	
f	flight	
u	upstream	
d	downstream	

Chapter 1

Introduction

1.1 Introduction

In the hypersonic flight regime, specific impulse is an important performance parameter. Specific impulse is the thrust generated per rate of fuel consumption and is the measure of the efficiency of an engine. The rockets use onboard liquid fuel and liquid oxygen to generate thrust, hence have low specific impulse, and their size/weight increases with an increase in speed or distance to be covered [1]. A scramjet, on the other hand, uses oxygen from the atmospheric air for combustion, thereby eliminating the need to carry liquid oxygen, which leads to an increase in specific impulse. This allows the vehicle to be smaller, lighter, faster, and capable of higher payload capacity [2]. However, scramjets

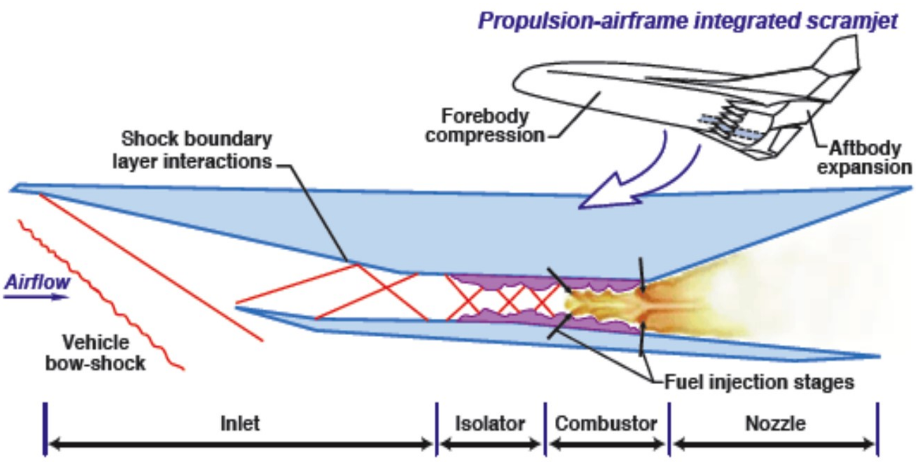

FIGURE 1.1: Components of scramjet engine
[3]

do not have a compressor; instead, they use high speed forward motion (ram-effect) for compressing the incoming air to higher pressure and temperature, enough for combustion, see Fig. 1.1. Hence, it has a limitation that it cannot work at low speeds and needs to be boosted until it achieves required speed.

In 2016, the Indian Space Research Organization (ISRO) successfully tested a scramjet engine in-flight onboard an Advanced Technology Vehicle (ATV) rocket. Two scramjet engines were attached to the rocket on its sides and were operational for a short duration when the ATV rocket reached an altitude of 11 km in the atmosphere [4]. It is predicted that scramjet can achieve a velocity of up to 15 times the speed of sound [2] making any place on earth accessible within 90 minutes in the future [5].

A schematic of the scramjet engine is shown in Fig. 1.2. It mainly consists of (i) an inlet, which compresses the incoming air to high pressure and temperature using shock waves, (ii) combustor, where the combustion takes place leading to the further increase in temperature, and (iii) nozzle, where the flow expands and exits at very high speed producing thrust. Isolator shown in Fig. 1.1, in many cases, is considered as part of inlet/intake.

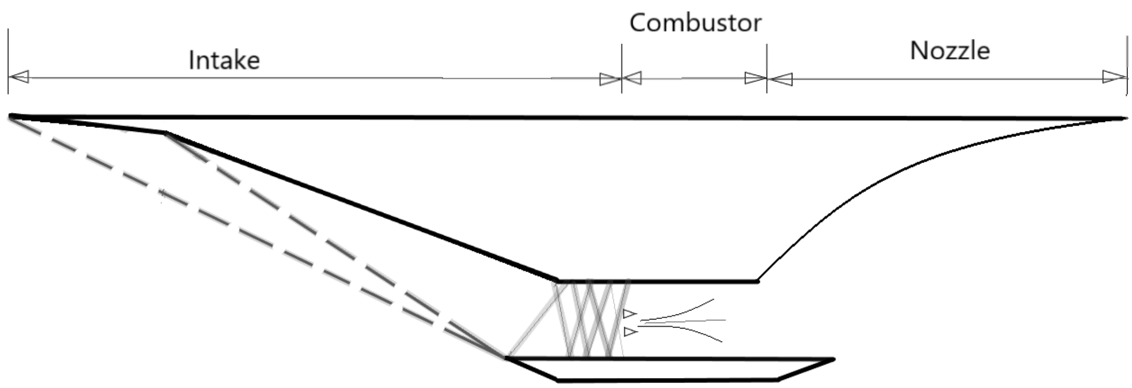

FIGURE 1.2: Schematic of ramp shocks (dotted lines) formed in the intake of a scramjet engine.

When the incoming supersonic flow hits the intake ramp, a shock wave is formed. The shock wave interacts with the boundary layer at the vehicle surface. If the adverse pressure gradient due to the shock is strong, it can lead to local separation and reattachment of the boundary layer. The flow separation can result in severe distortion of the inviscid flow-field around the vehicle. At high Reynolds number, the boundary layer over the vehicle surface is often turbulent. The turbulent fluctuations get amplified across the shock wave and have a significant effect on the extent of the separation.

For simulating such flows, Reynolds Averaged Navier-Stokes (RANS) equations are usually employed and the effect of turbulent fluctuations on the mean flow-field is modeled using turbulence models. The advances in computing power has given rise to advanced tools such as Direct Numerical Simulations (DNS) and Large Eddy Simulations

(LES). Although DNS and LES employ more physics-based representations of the problem, RANS equations solved along with turbulence models is still an efficient and valuable tool for CFD analysis.

In RANS, the averaging of the flow variables introduces the unknown Reynolds stress term, which is modeled using Boussinesq's approximation in terms of eddy viscosity. Such turbulence models based on the Boussinesq's approximation are known as eddy viscosity turbulence model. Other turbulence models, which are not limited by Boussinesq's approximation, such as Reynolds stress turbulence models, have given mixed results. The eddy viscous turbulence models are widely used as it requires solving only one or two extra equations and is computationally economical.

1.2 Motivation

The shock waves interact with the vehicle body leading to flow separation and formation of the separation bubble in the subsonic portion of the boundary layer. Presence of a separation bubble alters the pressure distribution over the intake surface, which alters the intake generated lift, which in turn affects the stability of the vehicle [6], [7], [8]. At the foot of the second ramp shock, originating from the compression corner/ramp, a separation bubble is formed inside the boundary layer, as shown in the schematic in Fig. 1.3 zoomed view. The presence of the separation bubble in the boundary layer becomes critical as it alters the pressure and skin-friction distribution over the surface.

If the lift due to the inlet is L_i and that due to the nozzle is L_n, then the moment due to these two forces should balance each other for stability. However, if the magnitude or location of L_i alters, due to the presence of separation bubble in the intake, and if it does not balance with the moment due to force L_n, then the stability of vehicle becomes difficult. Hence accurate prediction of wall-pressure distribution over the vehicle surface is essential for the control of the vehicle.

The location of the center of pressure (CP) relative to the center of gravity (CG) is an important parameter for the stability and hence the mission. Presence of the separation bubble leads to shifting of the center of pressure relative to CG and thus affecting the stability. Even-though parameters like pitching moment, hinge moment, etc. are mainly dominated by the inviscid phenomenon, the presence of separation bubble can affect it to some extent in adverse conditions. All these modifications, due to changes in wall-pressure and skin-friction distribution over the vehicle surface, change the aerodynamic characteristics and deteriorate the performance of the vehicle. This leads to loss of control surface effectiveness and vehicle instability [6] [7]. Hence, it is important to study

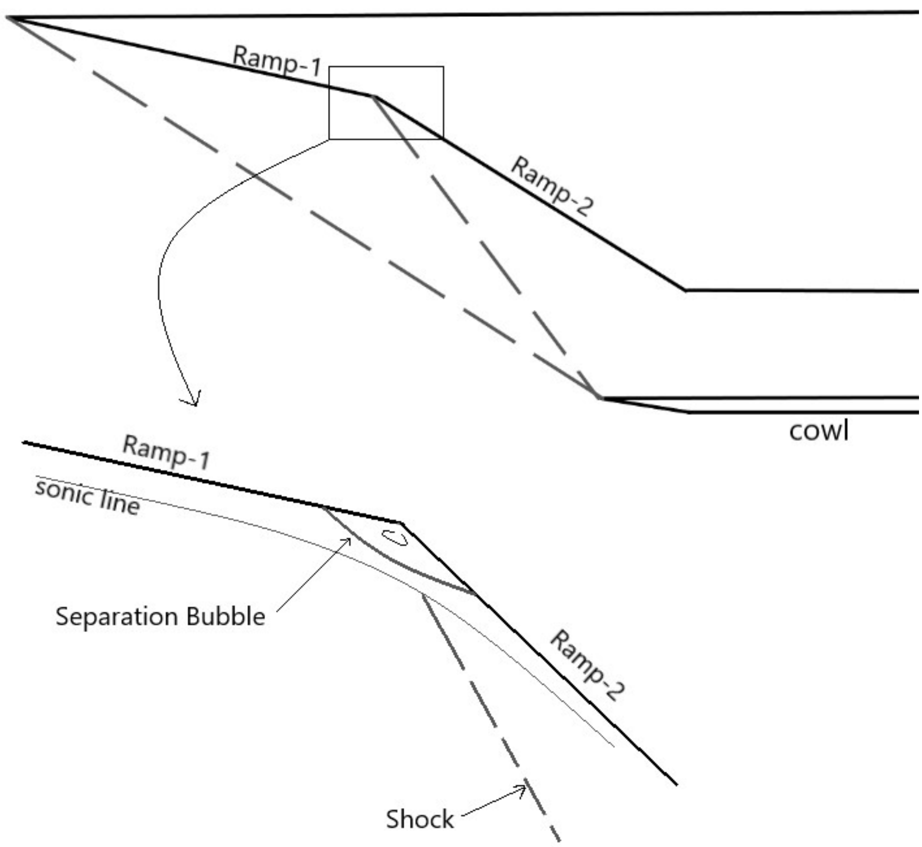

FIGURE 1.3: Intake of a scramjet engine and zoomed view shows the schematic of the separation bubble formed at the corner between the two ramps.

the effect of the separation bubble on intake generated lift and drag for different flight parameters.

1.3 Problem definition

To study the effect of flow separation in scramjet intakes, a geometry and flight conditions corresponding to Mach number M = 6, altitude z = 30 km (where $\rho = 0.01802\ kg/m^3$ and T = 226.55 K) and angle of attack $\alpha = 0$ is considered. The intake length and height are taken to be L = 2.5 m and H = 1.0 m, respectively, as shown in Fig. 1.4. The remaining flow and geometric parameters are calculated using Rankine-Hugoniot relations keeping the shock-on-lip condition (where both the shocks meet at the tip of cowl) satisfied.

The intake consists of two ramps followed by a horizontal portion forming the isolator or duct. The first ramp, of length L_1, is inclined at an angle of θ_1 with the free-stream. The second ramp, of length L_2, is inclined at an angle ϕ_2 with respect to free-stream (or at an angle θ_2 with the first ramp). On the upper side, it consists of a cowl; the tip of cowl

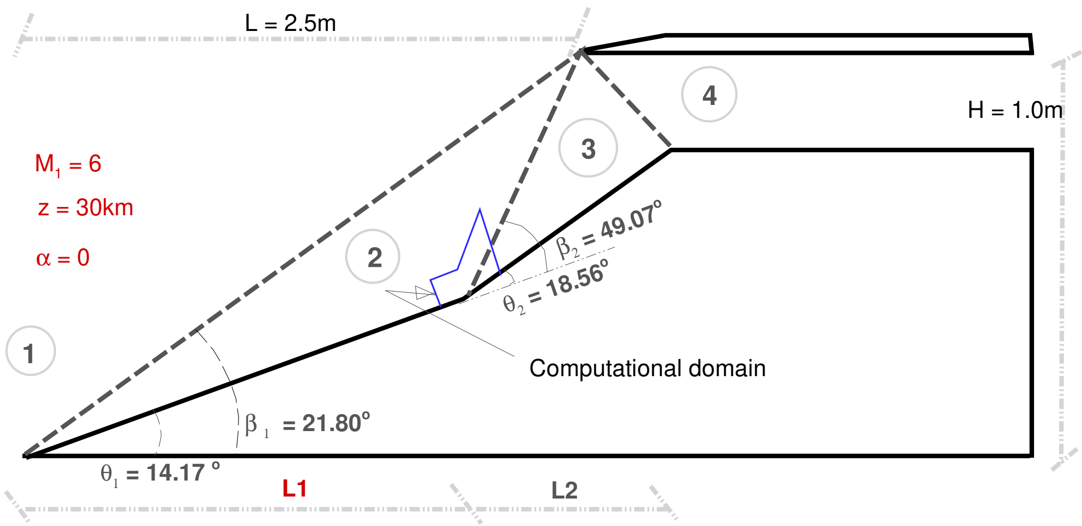

FIGURE 1.4: Schematic of a scramjet intake flow satisfying the shock-on-lip condition.

starts at a distance L = 2.5m from the leading edge. The height of intake (vertical distance between the tip of the cowl and the leading edge of the first ramp) is H = 1.0 m. Based on the above-described flow conditions and geometry, the first ramp angle required to satisfy shock-on-lip condition is θ_1 = 14.179 °, which gives the corresponding first shock angle $\beta_1 = 21.80°$. The value of the second ramp angle depends on the length of the first ramp. In the given schematic, L_1 is assumed to be 2.00 m, which gives the second ramp angle to be $\theta_2 = 18.56°$ in order to satisfy the shock-on-lip condition. Fig. 1.4 shows the values obtained using the shock-on-lip condition.

For a fixed geometry vehicle, the parameters that frequently vary in flight conditions are (i) flight Mach number , (ii) Cruise altitude and (iii) Angle of attack, and all of these three parameters are considered in this study. The fourth parameter, which is more of a design parameter rather than flight parameter, is the variation in first ramp length L_1 and is also covered in this study. This parameter would be more relevant for variable geometry applications. The various flight parameters that can affect the size of the separation bubble are

- Flight Mach number : M_1
- First ramp length : L_1
- Angle of attack : α
- Cruise altitude : z

TABLE 1.1: On and Off-design values used for the study of flight parameters affecting flow separation.

Flight parameter	On-design	Off-design conditions
z (km)	30	26, 28, 30, 32, 34
M_1	6	4, 5, 6, 7, 8
α	0	-4, -2, 0, 2, 4
L_1 (m)	2.00	1.50, 1.75, 2.00, 2.25

The range of on-design and off-design parameters considered for the study are given in Table 1.1. The on-design conditions listed in second column of Table 1.1 are the conditions at station-1 (free-stream), as shown in Fig. 1.4. The range of off-design conditions is obtained by varying the given flight parameter with reference to on-design condition value. The effect of these flight parameters on separation length, which subsequently affects the pressure distribution over the surface and the stability of vehicle, will be studied over this geometry for different on-design and off-design conditions. Further, in order to quantify the effect of separation bubble on intake generated lift and drag, the percentage difference of CFD computed results with the inviscid solution is considered. This percentage difference shows the expected deviations in the aerodynamic characteristics of the vehicle when the flow inside the boundary layer separates, and a separation bubble is formed.

Concerning the flight parameters affecting flow separation, Miller et al. [9] commented that scaling of separation length with respect to different flight conditions is least explored and hence, there is limited understanding in this area. Marini et al. [10] suggested that the effect of wall-to-recovery-temperature ratio should be included in the scaling parameter to characterize the physical phenomenon. Subsequently, an effort is made to include this parameter in scaling of the separation length under different flight conditions.

When a given flight parameter is varied, multiple flow parameters get varied across the shock, which makes the understanding/justification of the observed trend in separation bubble length changes, difficult. For example, as the flight Mach number M_1 at station-1 is varied, the Mach number, pressure, temperature, and density also get varied at station-2. The changes observed in separation length is the cumulative effect of variation due to all these parameters at station-2. Same is the case with other parameters like altitude, angle of attack, and ramp length, where a change in one flight parameter affects multiple post-shock parameters at station-2. Hence, it is important to study the effect of canonical parameters on flow separation. The canonical parameters are individual parameters that affect shock-induced flow separation.

The next task is to identify the list of canonical parameters to be studied so that the changes in separation length with respect to all the flight parameters can be justified. It is seen that by varying flight parameters, the parameters that get varied are - ramp angle θ, Mach number M, Reynolds number Re_δ and flow-properties (pressure, temperature, and density). Based on the above, the following four parameters are considered for the study of canonical parameters affecting flow separation.

1. Ramp angle : θ
2. Mach number : M
3. Reynolds number : Re_δ
4. Wall-to-recovery temperature ratio : T_w/T_r

The first three canonical parameters are directly taken from list of parameters being affected by the flight parameters. The fourth parameter - wall-to-recovery-temperature ratio T_w/T_r - is one of the most important parameters in separation length analysis as it not only considers the effect of wall-temperature but also of outer flow temperature. T_w is the wall-temperature and T_r is the recovery temperature given as $T_r = T(1+\frac{\gamma-1}{2}M^2)$.

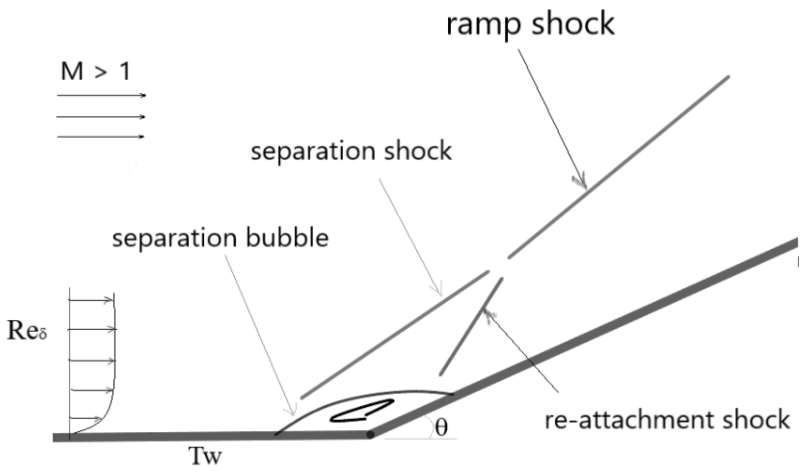

FIGURE 1.5: Canonical parameters affecting flow separtion over a compression corner geometry.

To study the effect of canonical parameters, on flow separation, a compression corner geometry (see Fig. 1.5) is considered. The compression corner is part of the scramjet intake shown in Fig. 1.3. The problem of shock boundary layer interaction is commonly studied in literature over this geometry, and hence, is considered as a model problem for the present study. The conditions at station-2 of scramjet intake (see Fig. 1.4) are taken as the upstream conditions for compression corner geometry. Using the conditions at station-1 in Fig. 1.4 and ramp angle θ_1, the conditions at station-2 are computed using the Rankine-Hugoniot relations, as given in second column of Table 1.2. To study, the effect of a given canonical parameter, the given parameter is varied in the range as given in the last column of Table 1.2. For example, to study the effect of Mach number, the Mach number (see schematic in Fig. 1.5) is varied (range given in Table 1.2) keeping all other parameters constant. Similarly, to study the effect of ramp/deflection angle, only ramp angle is varied keeping all other parameters constant. The wall temperature is varied as T_w = 200, 300, 400, 500 and 600 K which gives the ratio T_w/T_r = 0.12, 0.18, 0.24, 0.29, and 0.35, respectively, as listed in Table 1.2.

TABLE 1.2: Values of canonical parameters varied to study the effect of flow separation over a compression corner geometry.

Canonical parameter	Reference value	Range of parameter considered
θ	18.56	5, 10, 15, 18.56, 20, 25
M	4.097	3.0, 3.5, 4.097, 4.5, 5.0
Re_δ	1.1E+5	9.5E+4, 1.0E+5, 1.1E+5, 1.2E+5
T_w/T_r	0.24	0.12, 0.18, 0.24, 0.29, 0.35

The simplicity of compression corner geometry allows us to do a controlled study whereby only one parameter is varied at a given time, and leads to enhancement of understanding of the physics of flow separation. This understanding will further help in justifying/predicting the trend in separation length changes under different flight conditions. If the physics of flow separation with the canonical parameters are well understood, then a proper scientific explanation can be given to justify/predict the separation bubble length changes under different flight conditions. Accordingly, a parametric study is performed to study the effect of canonical parameters on flow separation.

An accurate prediction of separation length is important to quantify its effect on the aerodynamic characteristics of the surface. Shock-wave affects the turbulence in the supersonic boundary layer, which in turn affects the predicted separation length and the wall pressure distribution over surface. The complexity of the physics makes the analysis difficult. However, the problem of turbulence interacting with a normal shock-wave is a similar problem, rich in physics and does involve complex physics due to boundary layer, shear-layer or flow separation at wall. This problem of turbulence interacting with normal shock-wave is frequently studied in literature ([11], [12], [13], [14], [15], [16]). Homogeneous isotropic turbulence interacting with a normal shock-wave is considered as a model problem, as shown in Fig. 1.6. A standing normal shock-wave is located inside the domain, and as the incoming supersonic flow passes through the shock, the turbulence in the flow interacts with the shock-wave and gets amplified across it. Availability of DNS

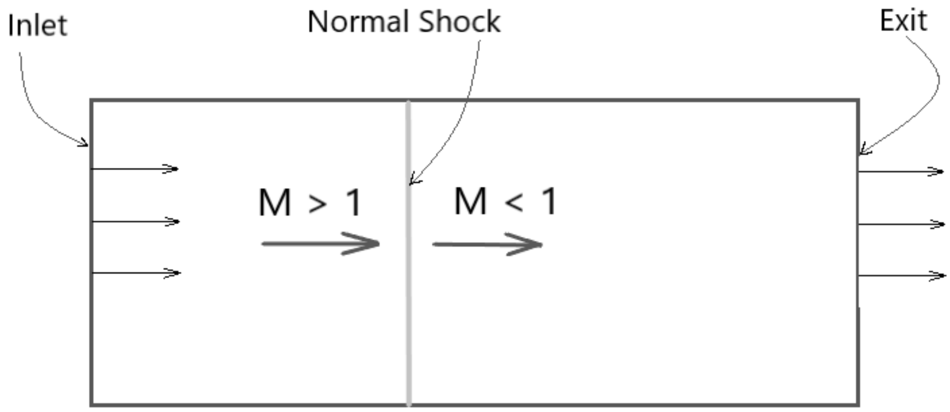

FIGURE 1.6: Supersonic flow over a normal shock wave.

data and theoretical estimates for a range of shock strength make it an ideal problem to test turbulence models.

1.4 Objectives

The objective is to compute the changes in the separation length for different flight parameters, scale it with a possible non-dimensional scaling parameter, and analyze its effect on the intake generated lift and drag. In order to justify the observed trend in separation length changes with different flight parameters, the understanding of the separation length changes with canonical parameters is necessary. Hence, the changes in separation length with the canonical parameters is studied over a compression corner geometry and physics behind the observed trend is analyzed in detail. Reliable prediction of shock-induced flow separation depends on the accuracy of the turbulence model used in the numerical simulation. In this work, the shock unsteadiness turbulence model [17], specifically developed for high-speed flows, is used for prediction flow separation in scramjet intakes. The model is based on inviscid analysis [18], representative of infinite Reynolds number. It is extended to an eddy viscous shock waves at realistic Reynolds number encountered in practical situations.

1.5 Outline of thesis

This thesis is divided into eight chapters, five appendices, and a bibliography. The first four chapters provide a background for the area of work carried out, whereas the results are presented in the subsequent three chapters. The conclusions of the work is presented in the last chapter, followed appendices and a bibliography.

The second chapter presents the details of the scramjet geometry, shock waves inside the intake and flow separation. The physics behind the flow separation over the compression ramp (also known as compression corner) is discussed and how it affects the distribution of different wall-parameters. The methodology for the computation of intake generated lift and drag is discussed. The variation of turbulent quantities inside supersonic boundary layer is discussed along with the concept of recovery temperature.

The literature survey is presented in the third chapter. The literature related to changes in separation length with different parameters is discussed followed by prediction of separation length. The standard turbulence models give inaccurate predictions for flows with high compression, whereas the modified turbulence models give comparatively better predictions. The impovement in predictions with the shock unsteadiness turbulence model is presented and the various geometries (compression corner, shock impingement, cylinder flare and scramjet intakes) where the model is sucessfully applied is discussed. The empirical relation available for the scaling of the separation length in turbulent flows involving shock boundary layer interactions is discussed. The literature related to the problem of shock-turbulence interaction is discussed in detail at the end.

The fourth chapter presents the overall simulation methodology - governing equations, turbulence models, numerical method, and boundary conditions used. The problem is mathematically modeled using the Navier-Stokes equation, which consists of the equation for mass, momentum, and energy. Since the flow is turbulent, the averaging leads to the unknown Reynolds stress, which is modeled in terms of k and ε and to solve it two more equations are required. These equations are discretized over the grid using finite volume method (FVM), and the numerical methods used to solve the discretized equation are presented.

Results are presented in three chapters. A schematic of the three parts is shown in Fig. 1.7, where shock waves interacting with the boundary layer on the intake of a scramjet engine is connected to the shock boundary layer interaction occurring in a compression corner geometry. The interaction of an oblique shock at the corner can be converted into a normal shock interaction, by coordinate transformation. The interaction of turbulence with a normal shock is a fundamental problem that helps in model development and comparison with DNS data.

The fifth chapter describes the results obtained for canonical shock turbulence interaction, Where the amplification of turbulence across a normal shock is studied. It is shown that numerical and physical modeling error can lead to large unrealistic level of turbulence behind a shock wave. Previously developed models are used, specifically the shock

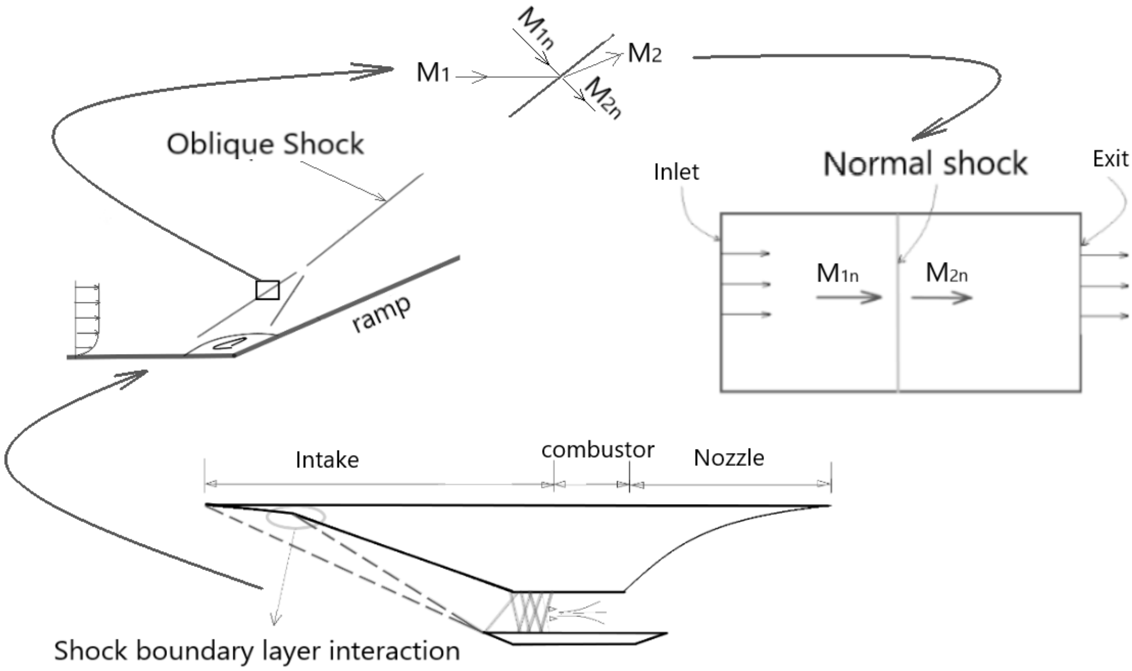

FIGURE 1.7: Overview of the work.

unsteadiness model of Sinha et al. [18], which is based on the physics of shock turbulence interaction. The model was developed in the said limit, i.e. for infinite Reynolds number. It is applied to normal shocks at finite values of Reynolds numbers encountered in realistic flows. This is a key step to extending the model to real life applications, and is next applied to compression corner simulations.

In the sixth chapter, the results related to effect of canonical parameters on flow separation is studied for a compression corner geometry that represents the corner between the two intake ramps of the scramjet engine. The variations in separation bubble length with respect to each of the canonical parameters (ramp/deflection angle, wall-to-recovery temperature, Mach number, and Reynolds number Re_δ) are analyzed. The values of the canonical parameters are taken from the off-design conditions of the flight parameters of the scramjet intake. The results are compared with those available in the literature. The near-wall flow-field is analyzed to understand the physics of separation. Moreover, the empirical relation available in the literature, for scaling of flow separation bubble length, is applied to present results and evaluated for each of the canonical parameters considered.

In the seventh chapter, the variation in separation length with different flight parameters, for both on-design and off-design conditions is studied. The observed trend in changes in separation length is analyzed based on the understanding/conclusions drawn from the study of separation length with the canonical parameters. Further, the effect of the separation bubble on intake lift and drag is studied at each of the flight parameters and the worst-case scenario, where the percentage difference is maximum, is identified. Finally, the wall-to-recovery-temperature ratio and the pressure ratio across the oblique shock are analyzed with separation length changes for each of the flight parameters to propose a scaling parameter for separation length studies.

The eighth chapter summarizes the conclusions and contribution of the present work along with the recommended future work. This is followed by appendices and bibliography for a reference.

Chapter 2

Background

In this chapter, the geometry of scramjet and other relevant concepts related to present work is discussed. The scramjet geometry and orientation is discussed in section 2.1. The shock waves inside a scramjet vehicle is discussed in section 2.2. The concept of shock interacting with boundary layer and flow separation is discussed in section 2.3. The methodology used for computation of intake generated lift and drag is discussed in section 2.4. The variation of turbulent quantities inside a supersonic boundary layer is discussed in section 2.5 whereas the concept of recovery temperature is discussed in section 2.6

2.1 Scramjet geometry and orientation

Fig. 2.1 shows the schematic of scramjet vehicle consisting mainly of the inlet, combustor, and nozzle. The shock boundary layer interaction occurs at the corner between the two ramps whereby flow separates leading to formation of separtion bubble at the corner. Fig. 2.2 shows the schematic of the intake of the above scramjet engine. In the computations, the intake is assumed to be in this position by turning the vehicle upside down; the cowl

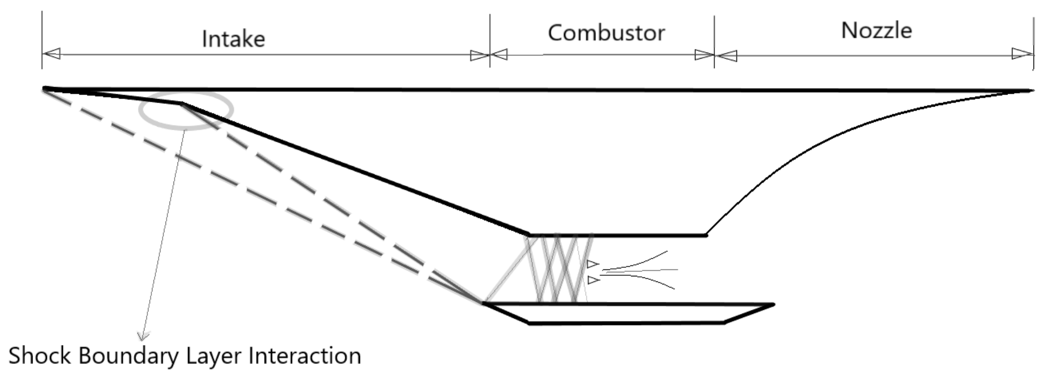

FIGURE 2.1: Shock interacting with boundary layer at the corner in intake of scramjet engine

is now at the top, whereas the ramps are at the lower part. The positive angle of attack corresponds to the case where incoming flow hits the inner ramp surface, as shown by an arrow with a dotted line in the schematic. Similarly, for the negative angle of attack, the incoming flow hits the outer vehicle surface. In this configuration, the lift generated by intake would be negative as it points towards the negative y-direction, whereas in actual vehicle geometry lift generated by intake would always be positive. Hence only the absolute values of lift are discussed in the study.

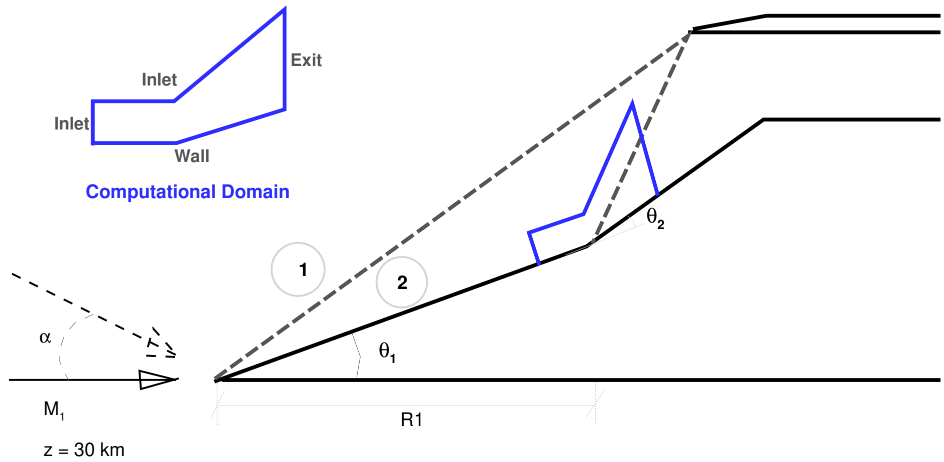

FIGURE 2.2: Schematic of intake of scramjet engine

2.2 Shock waves in scramjet intakes

Scramjet is a typical hypersonic vehicle that cruises at high speeds using the shock waves, as shown in Fig. 2.3. It is difficult to understand these interactions over a full three-dimensional vehicle geometry due to its complexity in interactions, and hence various canonical 2D and 3D geometries, which act as a small part of the vehicle, are studied frequently to understand the flow physics in-depth. Compression corner and an Impinging shock (shock impinging on a flat-plate) are two commonly studied two-dimensional canonical geometries.

Fig. 2.4a shows the schematic of supersonic inviscid flow over a compression ramp which consists of flat-plate and ramp. The flat-plate is parallel to flow while the ramp is inclined at an angle with respect to the incoming flow. The ramp acts as an obstruction to the supersonic flow over the flat-plate, and this leads to the formation of single oblique shock from the corner. There is a sudden jump in flow properties (pressure, temperature, density, and Mach number) across the shock, and this jump can be calculated using the

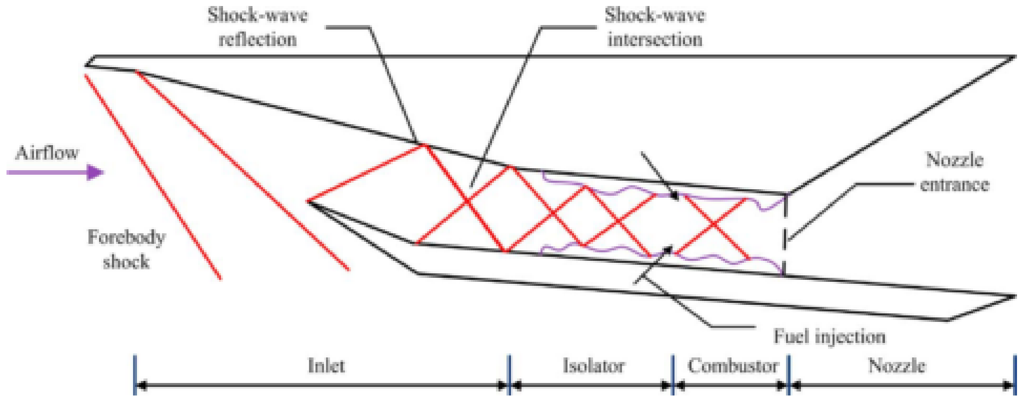

FIGURE 2.3: The typical scramjet flow path [3].

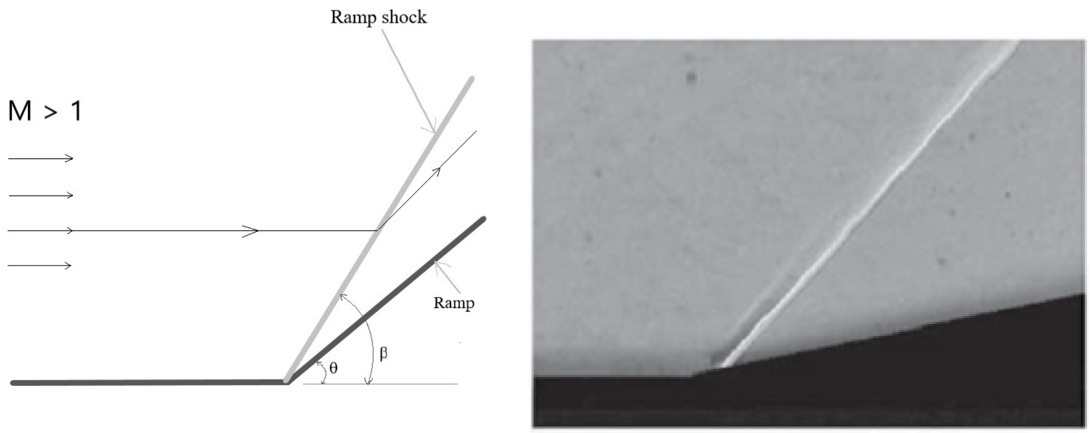

(a) (b)

FIGURE 2.4: (a) Schematic and (b) schlieren image [19] of supersonic flow over a compression corner geometry.

Rankine-Hugoniot relations of gas dynamics. Fig. 2.4b shows the schlieren image of the supersonic flow over a ramp.

Fig. 2.5a shows the schematic of supersonic flow over an impinging shock. It consists of the flat-plate parallel to the incoming flow and a shock generator above it inclined at an angle θ with respect to the flow. The incoming air flows through the passage between the flat-plate and shock-generator. In this case, the shock-generator acts as a ramp to the supersonic flow over the flat-plate, and this leads to the formation of an oblique shock from the corner of the shock-generator. This oblique shock, known as the incidence shock or the impinging shock, hits the flat-plate and gets reflected to form a reflected shock, as shown in the Fig. 2.5b.

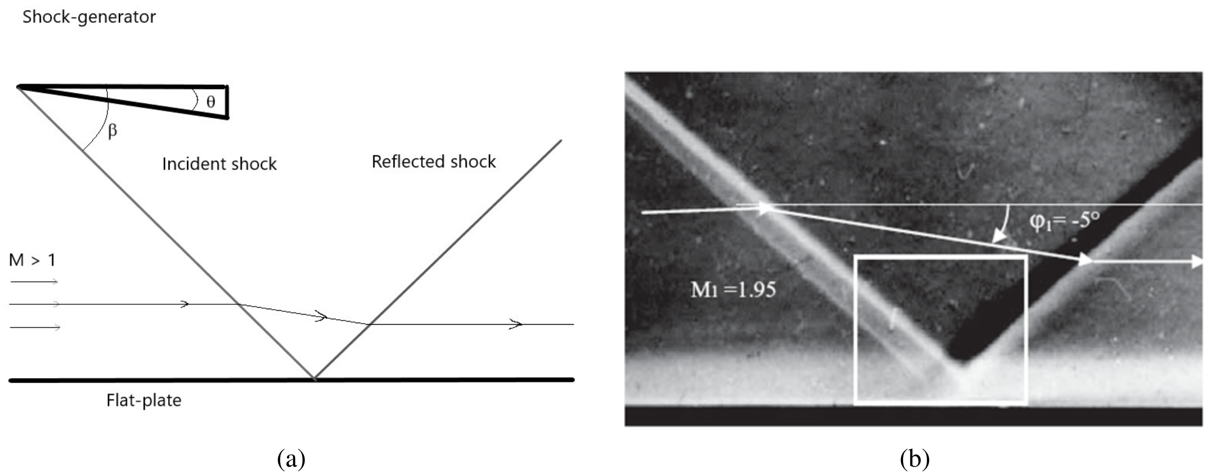

FIGURE 2.5: (a) Schematic and (b) schlieren image [19] of supersonic flow over a shock impinging on a flat plate.

2.3 Shock boundary layer interactions

The interaction of shock with the boundary layer is a complex phenomenon. Most of the current understanding is based on experimental work and computational predictions by various researchers in the past. Based on the strength of interaction, the interaction can be classified into two categories [19]: weak interactions, where no separation bubble is formed and the strong interactions, where flow reversal takes place leading to the formation of the separation bubble.

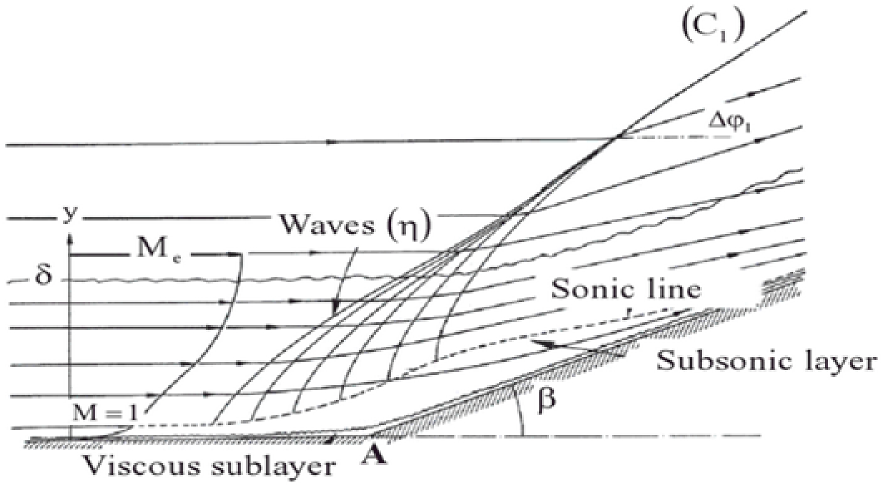

FIGURE 2.6: Weak interaction due to shock interacting with boundary layer [19].

Weak Interactions

Ideally, for an inviscid flow, when a shock is formed due to obstruction (compression corner), there is a sudden jump in pressure across the shock. However, for viscous flows, the pressure rise is gradual and distributed over a region due to the boundary layer formation. In the boundary layer, this pressure gradient is distributed upstream and downstream the point where ideally the shock would hit or from where it would have formed. Hence a pressure rise is seen upstream of the corner A and is known as upstream influence. The adverse pressure gradient imposed by the shock leads to thickening of the subsonic channel in the boundary layer, which acts as a ramp for flow upstream of the corner. The swelling of the subsonic channel leads to the formation of continuous compression waves which coalesce to form shock C1 in the outer flow, as shown in Fig. 2.6.

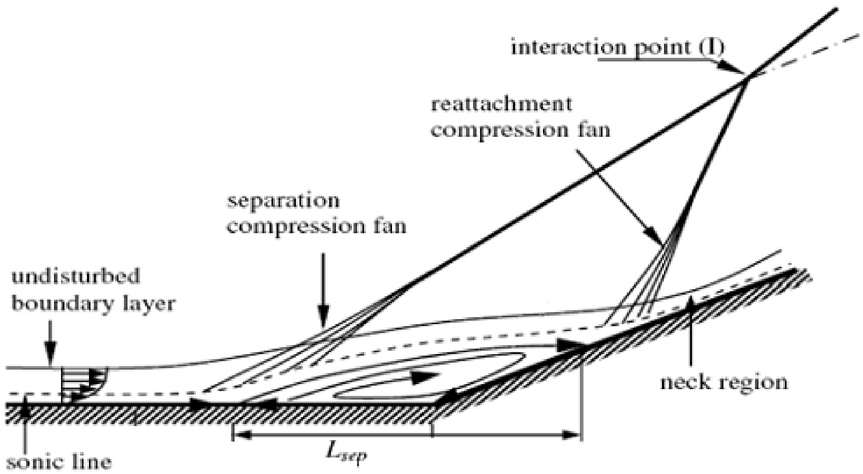

FIGURE 2.7: Strong interaction due to shock interacting with boundary layer and formation of separation bubble [19].

Strong Interactions

If the pressure rise associated with ramp shock is very high, then it will lead to separation of flow, and a separation bubble will be formed in the subsonic boundary layer. Flow separation will occur at point located upstream of corner, and reattachment of the flow will occur at a point located downstream of the corner, as shown in Fig. 2.7. The fluid inside the separation bubble keeps re-circulating. The re-circulating bubble is always located below the sonic streamline, and this acts as dividing streamline separating the re-circulating flow from the outer flow. The formation of the separation bubble leads to swelling of the subsonic boundary layer, which acts as a ramp for the upstream flow. This swelling of the subsonic boundary layer induces compression waves that coalesce to form the separation shock (shown as compression fan in Fig. 2.7). On the downstream side, the reattachment of separation bubble and the ramp again act as a ramp, where the reattachment compression waves/fan coalesce to form the reattachment shock. The separation shock and the reattachment shock together coalesce to form the ramp sock in the outer inviscid region of the flow (see Fig. 2.7). Since the viscous solution deviates strongly from the inviscid solution due to the formation of the separation bubble, such behavior is said to be of strong interaction.

Role of the Boundary Layer

The boundary layer consists of an outer part which is supersonic and a near-wall viscous part which is subsonic. As the shock hits the boundary layer, the pressure rise caused by the shock is transmitted upstream of the subsonic part of the boundary layer. So the distribution of the wall pressure is spread over a distance. *For weak interactions [19]*, the

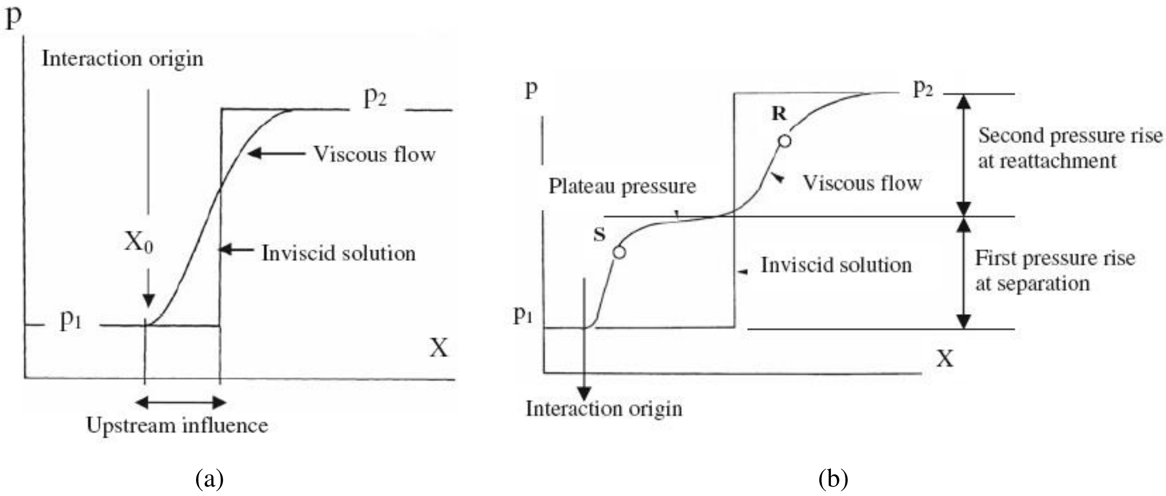

FIGURE 2.8: Pressure distribution for (a) weak interaction and (b) strong interaction [19].

order of the spreading of wall pressure is equal to the boundary layer thickness. Hence the actual solution does not deviate much from the inviscid solution. Thus, the viscous effects can be neglected, and the inviscid solution can be considered as the solution. *For strong interactions [19]*, a high rise in pressure induces greater retardation in near-wall velocity where P_0 is very low - i.e., in the boundary layer near to the wall. With further increase in pressure (flow moving further toward adverse pressure gradient condition), the near-wall velocity decreases till a point is reached when the flow adjacent to wall stagnates, and flow separates. This flow stagnation leads to the reversal of the flow and the formation of the separation bubble. This separation bubble acts as an obstruction to the outer supersonic flow in the boundary layer and acts as a ramp. Consequently, the wall pressure distribution exhibits a steep pressure rise and plateau at the separation point. A second pressure rise, steeper than the previous one, is seen near the reattachment point. Here the actual pressure distribution deviates considerably from the inviscid solution, as shown in Fig. 2.8. This deviation shows that viscous effects play an important role and can no longer be neglected in establishing the actual solution.

2.4 Lift and drag calculation

Fig. 2.9 shows the schematic of distribution of pressure forces over the two ramps - solid lines denote the inviscid pressure jump and dash lines correspond to that computed using CFD results. The inviscid pressure P_1 and P_2 over the first and second ramp, respectively, remain the same throughout the ramp length. However, the pressure distribution computed using CFD deviates from the inviscid values due to the presence of the separation bubble at the corner.

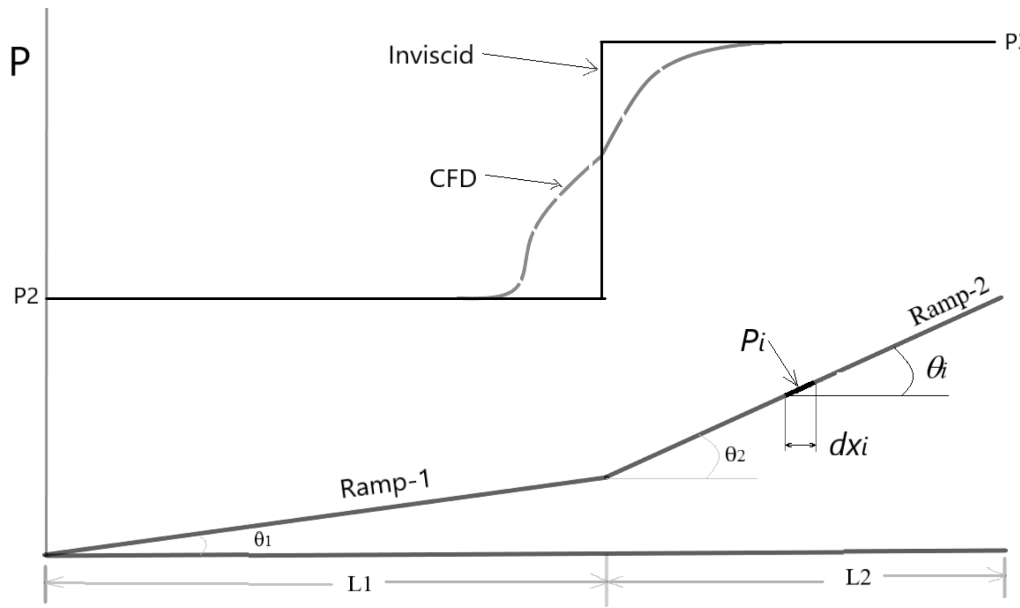

FIGURE 2.9: Schematic of comparison of inviscid vs CFD predicted pressure distribution over two ramp surfaces and pressure P_i acting over a element of length dx_i inclined at angle θ_i .

The inviscid force acting on two ramps is given as

$$F_{Inviscid} = P_2\, L_1 / cos\theta_1 + P_3\, L_2 / cos\theta_2 \tag{2.1}$$

where L_1 and L_2 are the horizontal components of lengths of first and second ramp respectively. The free-stream pressure is P_1 and the pressure acting over the first ramp is P_2

whereas that acting over the second ramp is P_3. The firs ramp is inclined at an angle of θ_1 whereas the second ramp is inclined at an angle of θ_2.

The total CFD force is computed by integrating the pressure P_i, acting on a grid cell at i^{th} location, over the two ramps. The length of the grid cell along x-axis is dx_i and its length along the surface is $dx_i\ cos\theta_i$. Thus, the total CFD computed force acting on the two ramps is given as

$$F_{CFD} = \sum_{1}^{n} P_i\ dx_i / cos\theta_i \tag{2.2}$$

where P_i is pressure acting at given cell i and $dx_i\ cos\theta_i$ is the distance along the surface over which the pressure P_i acts. In order to compute the lift and drag due to the above forces, the components of the force are taken in horizontal direction (drag force F_x) and in vertical direction (lift force F_y) as given below.

$$F_y = F_{CFD}\ cos\theta_i \tag{2.3}$$

$$F_x = F_{CFD}\ sin\theta_i \tag{2.4}$$

where θ_i is ramp angle at a given location which is constant for a given ramp. The inviscid lift and drag forces are calculated using the same equations as above by taking the horizontal and vertical components of the inviscid force.

2.5 Supersonic boundary layer data

The turbulence (or turbulent) Reynolds number was found to be an important parameter for the study of the effect of turbulent diffusion terms, and is discussed in brief. The shear-stress acting between different layers of the fluid is a function of shear-strain ($\partial u / \partial x$) and molecular viscosity (μ) of the fluid. The shear-stress is given as

$$\tau = \mu \frac{\partial u}{\partial x} \tag{2.5}$$

As far as mean flow is concerned, the net effect of turbulence is is to augment the laminar viscosity and replace it with eddy viscosity [20]. Eddy-viscosity accounts for the viscosity generated due to eddies in the turbulent flow. Eddy viscosity is a property of turbulence and of flow. Reynolds stress is modeled using Boussinesq eddy viscosity assumption and is related to the eddy-viscosity of the flow as given below [21]

$$R_{ij} = \mu_t \left[2S_{ij} - \frac{2}{3}\frac{\partial u_k}{\partial x_k}\delta_{ij} \right] - \frac{2}{3}\rho k \delta_{ij} \tag{2.6}$$

$$\mu_t = c_\mu \rho k^2/\varepsilon \tag{2.7}$$

All eddy-viscosity based turbulence model are based on the assumption that the Reynolds stresses are proportional to mean velocity gradients and eddy-viscosity. This assumption is also known as Boussinesq viscosity assumption. The turbulent Reynolds number based on dissipation length scale is defined as [22]

$$Re_t = c_\mu \frac{k^2}{\varepsilon \nu} \tag{2.8}$$

Using the relation for dissipation length scale as $l = c_\mu \rho \frac{k^{\frac{3}{2}}}{\varepsilon}$, the above can be re-written as

$$Re_t = \frac{\mu_t}{\mu} \tag{2.9}$$

Thus, the turbulence Reynolds number can is also be defined as ratio of eddy-viscosity to molecular viscosity.

TABLE 2.1: Flow variables corresponding to $Re_{t,max}$ values obtained from boundary layer data at different locations on flat-plate.

M	M_t	$Re_{t,max}$	Re	Location (x, m)
2.437	0.115	2.16×10^3	1.51×10^6	2.50
2.384	0.117	1.82×10^3	1.25×10^6	2.02
2.412	0.120	1.43×10^3	9.95×10^5	1.51
2.411	0.122	1.02×10^3	7.33×10^5	1.03
2.384	0.129	6.25×10^2	4.63×10^5	0.58
2.338	0.142	1.89×10^2	1.53×10^5	0.15

Fig. 2.10 shows the variation of Re_t and M_t along y-direction at different x-locations along the plate. Table 2.1 shows the numerical value of these turbulent quantities at different x-locations along the flat plate, along with the Mach number and the Reynolds number, at the corresponding locations. The free-stream conditions are taken as ρ_1 = 0.825 kg/m3, u_1 = 570 m/s, and T_1 = 100 °K. As shown in Fig. 2.10a, the turbulent Mach number increases from zero values at the wall to small values outside the boundary layer. The turbulence Reynolds number Re_t increases from a zero value at the wall to a maximum in the boundary layer and drops back to zero value outside the boundary layer edge, as shown in Fig. 2.10b. The peak value of these turbulent quantities increases along the x-direction, i.e., as the x-location increase the peak value of the turbulent quantities increases.

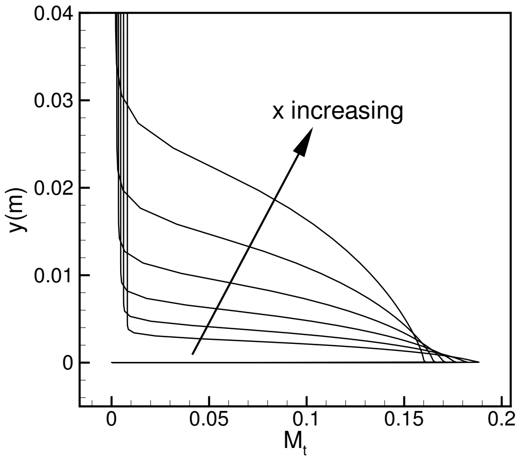

(a)

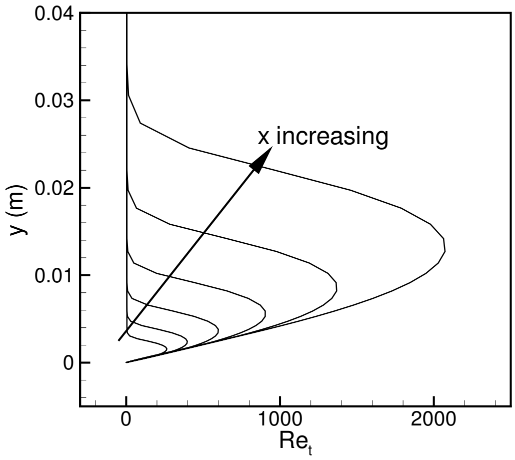

(b)

FIGURE 2.10: M_t and Re_t variation in supersonic boundary layer.

2.6 Recovery temperature

In order to measure the stagnation temperature in high-speed flows, the probes are designed such that they offer minimum obstruction to the incoming flow. Ideally, if the flow reaches stagnation point isentropically without any heat exchange between probe and surrounding, then the probe indicates the stagnation temperature given as [23]

$$T_o = T_\infty + \frac{u_\infty^2}{2c_p} \tag{2.10}$$

where c_p is specific heat of fluid at constant pressure, u_∞ and T_∞ are free-stream velocity and temperature, respectively. However, when the fluid flows over the probe, a boundary layer is likely to be formed, resulting in velocity gradient, shear stress, and heat dissipation within the boundary layer. So the temperature measured by the probe is above the stagnation temperature. At the same time, the temperature gradient in the boundary layer leads to heat loss from the probe. The opposite trend of these two phenomena tend to cancel each other, and the Prandtl number is used to take into account of this effect. Since the Prandtl number for gases is Pr < 1, the heat conduction dominates, and the measured temperature is generally below the stagnation temperature. If the probe is insulated, there will be no heat exchange and probe temperature will be the adiabatic wall temperature T_{aw}. This deviation in probe reading is expressed by a factor called recovery coefficient given as,

$$r = \frac{T_{aw} - T_\infty}{T_o - T_\infty} \tag{2.11}$$

and the recovery temperature is given as

$$T_r = T_\infty \left(1 + r\frac{\gamma - 1}{2} M_\infty^2\right) \tag{2.12}$$

The recovery co-efficient r depends on the characteristic of flow near surface, flow-regime and thermal properties of the medium. At the stagnation point in the flow, the value of r is equal to unity. For laminar boundary layers, the value of $r = \sqrt{Pr}$ and for turbulent boundary layer flows, it is given as $r = Pr^{1/3}$.

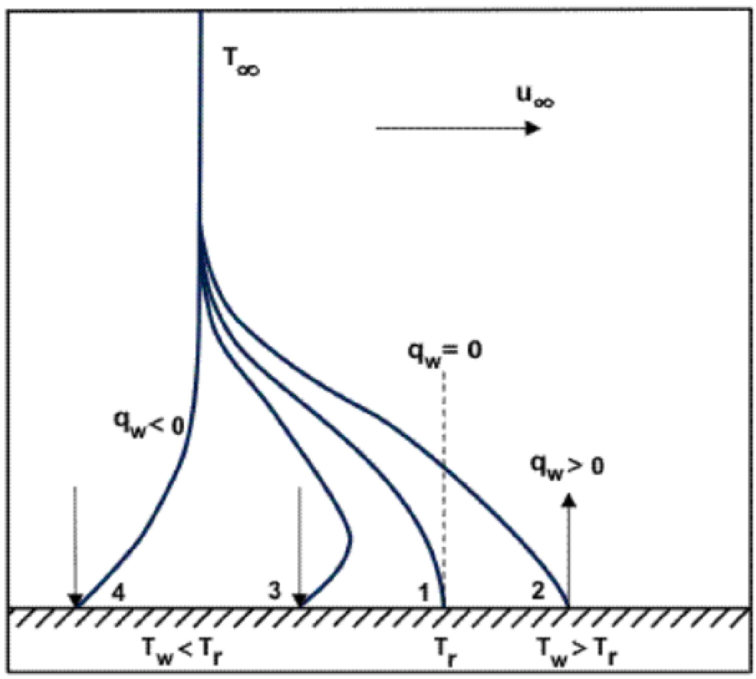

FIGURE 2.11: Heat transfer for different wall-to-recovery temperature ratios [24].

Wall-to-recovery-temperature ratio is the ratio of wall temperature to recovery temperature. This ratio is used to designate the direction of heat flow between the surface/wall and the free-stream. If the wall temperature is less than the recovery temperature ($T_w < T_r$) as shown in curve-3 and curve-4 of Fig. 2.11, there would be heat-transfer from surrounding to the surface. If the wall temperature is greater than the recovery temperature ($T_w > T_r$), the surface walls will dissipate heat to the surrounding. However, if the wall temperature is equal to recovery temperature ($T_w = T_r$) as shown by curve-1 in Fig. 2.11, there will be no heat transfer between the wall and surrounding.

2.7 Summary

The geometry of scramjet and its orientation with respect to present work is discussed. There are multiple shock-waves formed inside the scramjet geometry, and the compression corner geometry is considered as model problem to study the shock-induced separation at the corner of intake. The interaction of shock with the boundary layer at the corner leads to flow separation and formation of separation bubble, which affects the intake generated lift and drag. The methodology for computation of intake generated lift and drag is discussed followed by discussion on variation of turbulent properties inside a supersonic turbulent boundary layer. The concept of recovery temperature and wall-to-recovery-temperature ratio is discussed at the end.

Chapter 3

Literature review

3.1 Introduction

The effect of various parameters on shock-induced flow separation, in supersonic and hypersonic flows, had been studied extensively in 1960s and 1970s. Renewed interest in hypersonic air vehicles has led to more research in this area in the recent years. The literature available in the years of 1960s and 1970s were mostly based on experiments due the limitation of computational resources available at that time. Most of the research articles, based on computational simulations, were published in the last two decades. The effect of different parameters on separation length is discussed in section 3.2. The discussion related to modification of standard turbulence models, which leads to improvement in separation length, is discussed in section 3.3. The discussion related to shock turbulence interaction is covered in section 3.5. Finally, the scaling of the separation for shock interacting with turbulent boundary layer is covered in section 3.4.

3.2 Parameters affecting flow separation

Needham and Stollery [25] did experiments for a range of Mach numbers and for different Reynolds number to study its effect on flow separation for wedge-compression corner (see schematic in Fig. 2.4) and shock-impinging over flat plate geometry. They found that as the Reynolds number increases the extent of separation increases for laminar flow regimes while opposites holds true when transition is located in the reattachment region. With respect to Mach number, it was seen that as the Mach number increases the separation gets delayed and extent of the separation gets reduced. J. Lewis [26] did experimental investigation to study the effect of Reynolds number for both cold and adiabatic wall cases in wedge-compression corner flows. They found that flows that remained laminar exhibited upstream movement of the separation with increasing Reynolds number while the turbulent flows were found to have a three-fold effect as the Reynolds number increases

(i) the extent of separation increases (ii) pressure gradient in the reattachment region increases and (iii) there is an overshoot in pressure jumps in the post-shock region. Further, they found that compared to the adiabatic case, as the wall is cooled, there is the less upstream influence and pressure rise shifts towards the corner, thereby indicating shrinkage of separation.

Holden [27] did an similar experiment to study the effect of different parameters on flow separation over wedge-compression corners and found that as the Mach number (M = 14, 16 and 20) increases the extent of separation region decreases and as the Reynolds number increases the separation length increases for laminar flows, similar to that found by Needham and Stollery [25]. F. Spaid et al. [28] did an experimental study on the interaction of turbulent boundary layer with the compression corner at M = 2.9 for different wall-to-recovery-temperature ratios and different Reynolds number. From their study, they found that the effect of wall-cooling was to decrease the separation length relative to the adiabatic flow and to increase the incipient separation angle. *Incipient separation angle refers to a state wherein the flow is on the verge of separation but has not yet separated. A slight increase in ramp angle would lead to separation of the flow [28],[29],[30].* Another way to look at this is with respect to attached flows - for a given temperature and ramp angle if the flow is in incipient separation then reducing the wall-temperature would make the flow fully attached, and to take it back to incipient separation the ramp angle has to increase.

Elfstrom [29] did experimental investigation on turbulent shock boundary layer interaction at the wedge-compression corner using pressure measurements along the wall for different ramp angles, wall temperature, and Reynolds numbers. They found that as ramp angle increases the upstream influence increases, which rapidly develops a plateau of increasing length, as shown in Fig. 3.1. They further observed that for flows close to incipient separation, the effect of an increase in T_w/T_r ratio is small but promotes earlier separation, and for well-separated flows this effect is almost negligible. However, the magnitude of pressure overshoot increases with the increasing T_w/T_r ratio. Raising the Re_δ increased both the extent of separation region and the magnitude of overshoot in pressure whereas the incipient separation angle reduces slightly. Coleman and Stollery [31] did a similar experimental study for turbulent flows over a compression corner with heat-transfer measurements along the wall for the same experimental setup. They found that the flow separation behaves in the same manner, as predicted by Elfstrom, with different wall temperatures. Both concluded that as the Re_δ increases the extent of the separation region increases and the incipient separation angle reduces.

Law [30] did an experimental investigation of turbulent boundary layer separation ahead of the compression corner at M = 3 and found that the separation distance, when

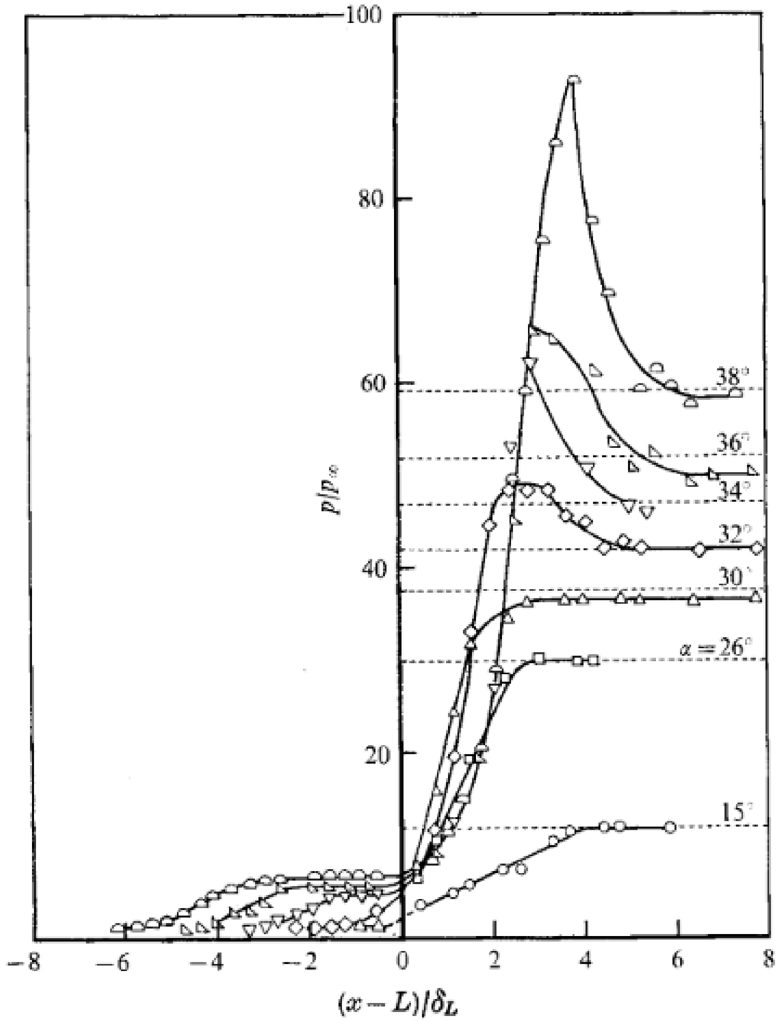

FIGURE 3.1: Wall-pressure distribution showing an increased upstream influence with a plateau and an overshoot in pressure for separated flows in experiments of Elfstrom et al. [29] at M = 9.22.

normalized by the boundary layer thickness, decreases with increasing Re_δ for a fixed ramp angle and the incipient separation angle increases with an increase in Re_δ. Roshko and Thomke [32] did an experimental investigation on the separation of the turbulent boundary layer over flare geometry (see schematic in Fig. 3.2) and found that the separation length, normalized by the boundary layer thickness, decreases as the Reynolds number Re_δ increases.

Settles et al. [33] carried our experiments on flow separation of turbulent boundary layer over compression ramp (see schematic in Fig. 2.4) and found that as the Reynolds number Re_δ increases, the upstream influence decreases as shown in Fig. 3.3. Katzer [34] did a numerical analysis of an oblique shock interacting with an adiabatic flat plate (see schematic Fig. 2.5) for a range of Mach numbers and Reynolds numbers. It was

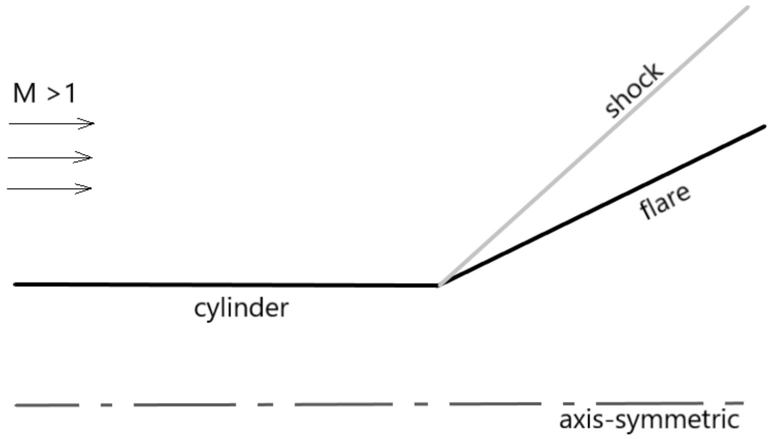

FIGURE 3.2: Schematic of cylinder-flare geometry

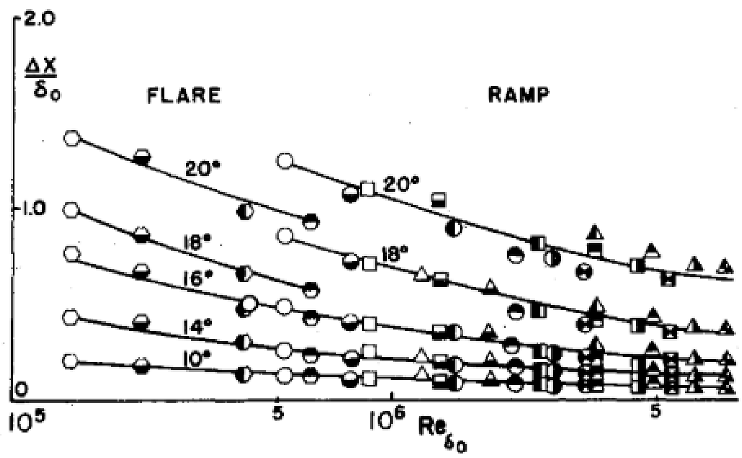

FIGURE 3.3: Variation of upstream influence with Reynolds number in experiments of Settles et al [33].

found that increasing the Reynolds number increases the length of the separation bubble. Concerning Mach number, their findings were consistent with the above researchers.

Marini et al. [10] studied the effect of ramp angle and wall-temperature on separation length using CFD simulations for flow over a compression ramp. The separation length was found to increase with increase in wall-temperature and ramp angle. Further, Marini et al. [10] suggested that the effect of wall-to-recovery-temperature ratio should be included in the scaling parameter to better characterize the physical phenomenon. Ciani [35] studied the effect of wall temperature for M = 6 turbulent flow over a 10 degree compression ramp for three different wall temperatures - 300 K, 400 K, and 500 K. The experiments were performed for three different Reynolds number corresponding to 11 bar, 21 bar and 31 bar at 300 K temperature and they concluded that a destabilizing effect is caused by increasing the wall temperature which leads to flow separation. Morgan et al. [36] carried out a parametric investigation of oblique shock impinging on a supersonic turbulent boundary layer (see schematic Fig. 2.5) to study the effect of ramp angle and Reynolds number. It was found that stronger shock, due to increased ramp angle, leads to wider interaction region and with respect to changes in Reynolds number, the separation length was found to be not much affected. Morgan et al. [36] commented that - *Although there have been a number of previous computational studies that look at OS-TBLI (Oblique shock turbulent boundary layer interactions), very few of these focus on simulating more than a single set of flow conditions, and those that do generally vary more than one flow parameter at a time, which makes it difficult to associate trends with particular flow parameters*. Miller et al. [37], commented that the behavior of separation length with respect to different flight conditions is least explored and hence there is a limited understanding in this area .

Jaunet et al. [39] did an experimental investigation on impact of wall temperature for M = 2.3 flow over a shock impinging on a flat plate (see schematic Fig. 2.5). They highlighted that the interaction length increases significantly as the wall temperature increases mainly due to changes in the wall incoming conditions i.e. the changes in the displacement thickness and the friction co-efficient of the upstream boundary layer. John et al. [40] studied the laminar boundary layer separation in the presence of ramp induced shock waves (see schematic in Fig. 2.4) for different Mach numbers and different wall temperatures using CFD. It was found that the incipient separation angle is a direct function of free-stream Mach number, and it decreases with increasing Mach number. Further, they observed that the size of the separation bubble decreases as the Mach number increases because higher free-stream Mach number means higher kinetic energy of the flow with same internal energy which leads to smaller separation bubble. As the wall temperature increases, the boundary layer thickness increases, and since thicker boundary layer are more susceptible to separation, earlier separation is seen as the wall temperature increases. Further, they added that the present investigations reveal little evidence that total-to-wall temperature ratio would be a more relevant quantity for separation bubble studies. Zhang [41] did a numerical investigation to study the effect of wall temperature on flow separation, and their findings were similar to that found by the above researchers.

Bernardini [38] did DNS to investigate the effect of wall temperature on the behavior of oblique shock-wave/turbulent boundary layer interactions for a free-stream Mach number of 2.28 and wedge angle of 8 degrees. They concluded that wall cooling leads to a considerable reduction in the interaction scales and the length of the separation bubble while the opposite holds for wall heating case. Vishwas [42] observed that the increasing Mach number delays the separation and advances the reattachment of the separated flow.

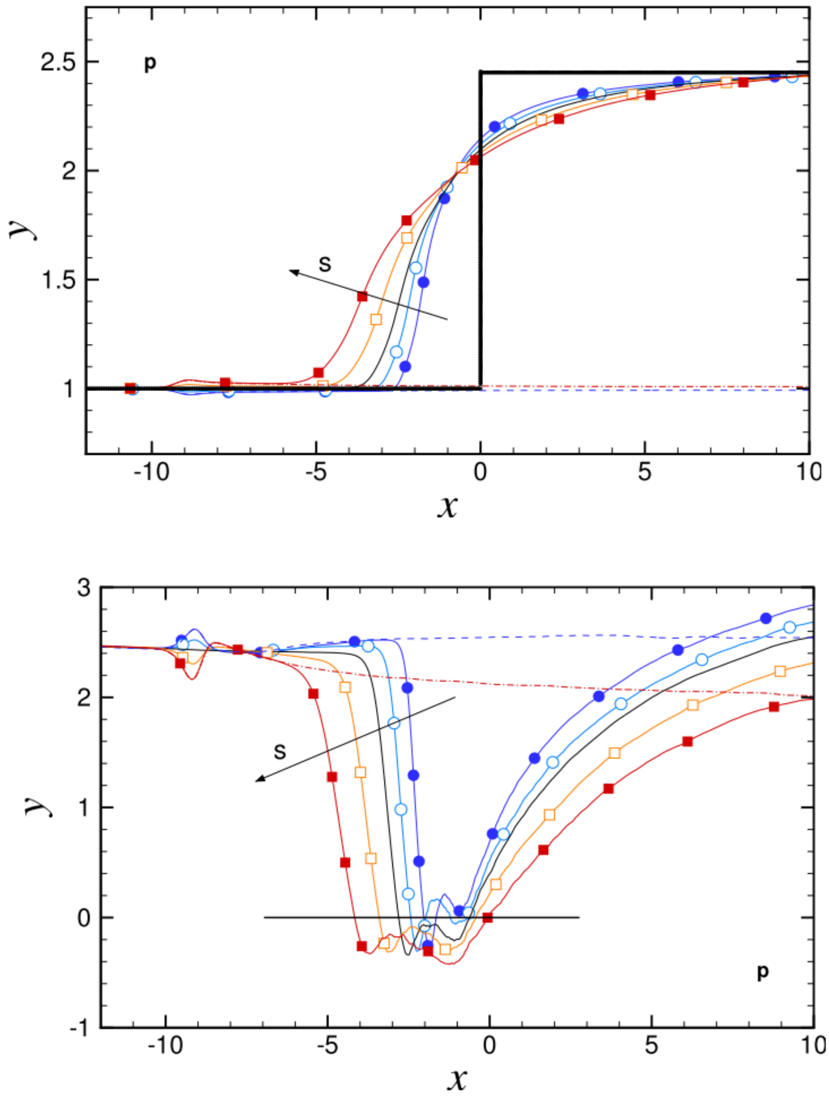

FIGURE 3.4: Effect of wall-to-recovery-temperature ratio (s) on wall pressure (top) and skin-friction (bottom) for M = 2.28 simulations of Bernardini et al [38].

No reasoning was given behind the observed trend. Davis et al [43] commented - Separation length should increase with increasing flap deflection (ramp angle θ) , or equivalently, with increasing reattachment pressure ratio p_3/p_2. There is no consistency in published results for the dependence of L_{sep} on Re_{x1}. Pasha [44] did a parametric study of changes in separation length concerning various parameters. Concerning Reynolds number, they observed that the size of separation length increases with increase in Reynolds number Re_δ. From their study of the effect of Mach number, they observed the same trend as previous researchers but the observed trend was not justified with any reasoning and the author commented - more investigations required to understand this behavior.

3.3 Prediction of separation length

CFD Simulations of high-speed turbulent flows, involving shock-wave/turbulent boundary layer interactions, are usually carried out using the Reynolds-averaged Navier-Stokes (RANS) framework. In this methodology, the flow variables are split into mean and fluctuating components. The mean flow-field is computed whereas the turbulent fluctuations

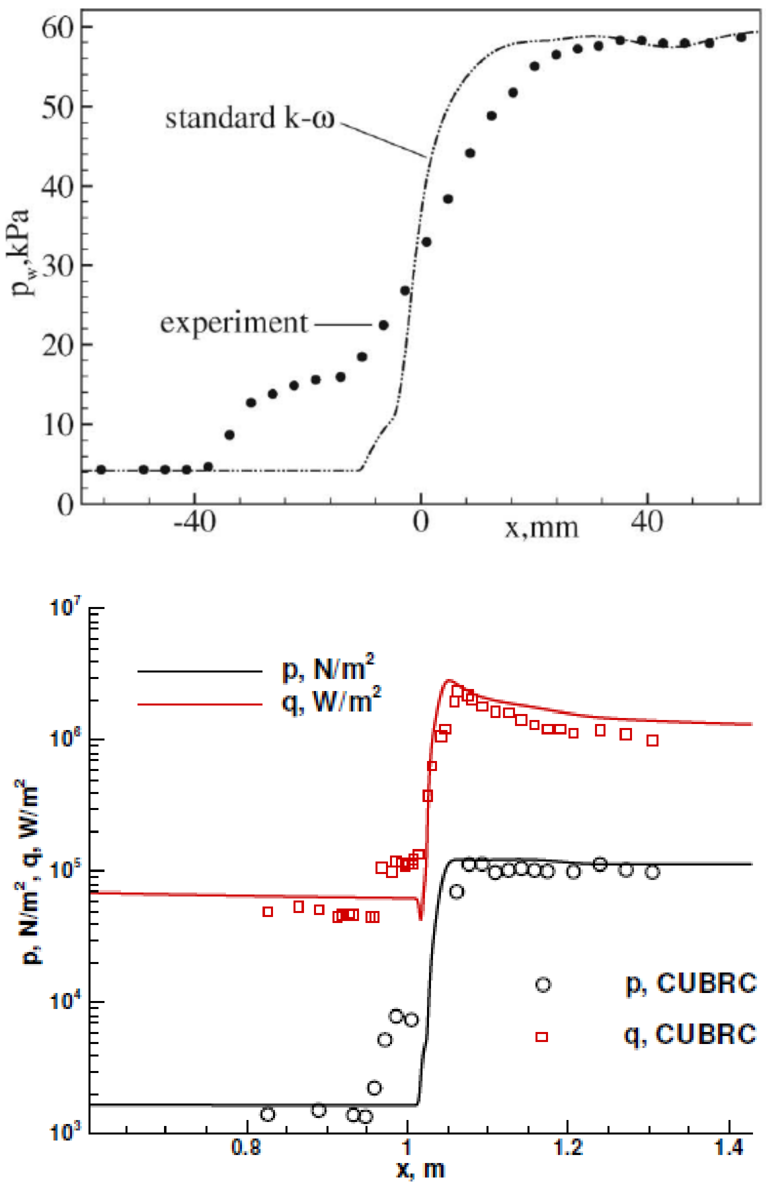

FIGURE 3.5: Pressure distribution as predicted by standard k-ω turbulence models in simulations for supersonic flow over compression ramp by (a) Pasha et al. [45] and (b) Gnoffo et al. [46].

are solved using the turbulence model. For flows involving strong interaction of the shock wave with the boundary layer, the boundary layer separates and a separation bubble is formed inside the boundary layer. The turbulence models, in their standard form, are unable to accurately predict the separation length, wall pressure and peak heat transfer rates. For example, in supersonic flow over a compression corner geometry, the standard k-ε turbulence model under-predict the separation length, i.e., the predicted separation point is far downstream of that observed in experiments whereas the predicted reattachment point is far upstream of that in experiments [18]. [47]. Fig. 3.5 shows the pressure distribution as predicted using standard k-ε and k-ω turbulence model. The pressure rise upstream of corner indicates the start of flow separation. In Fig. 3.5a the computational predictions obtained using standard turbulence models is compared with the experimental data of Settles et al. [48] for 24 degree compression case. Whereas in Fig. 3.5b, the computational predictions are compared with the experimental data of Holden et al. [49]. As seen, the standard turbulence model do not accurately predict the separation length.

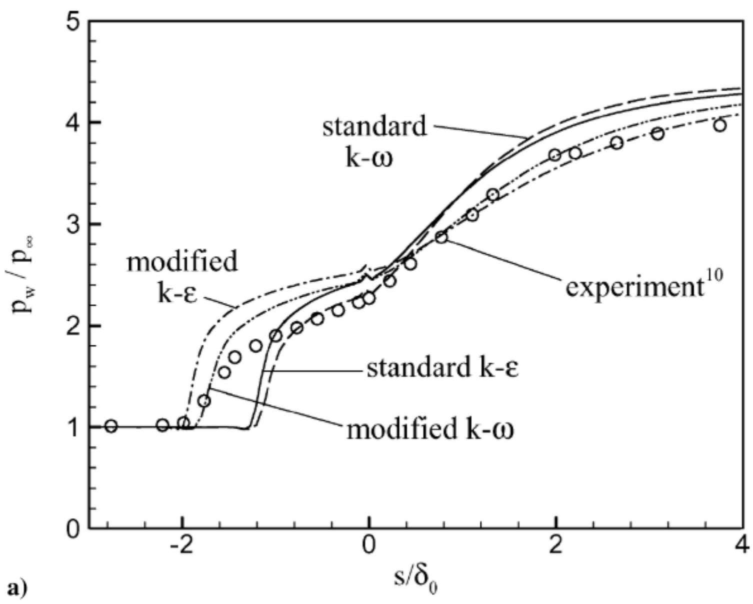

FIGURE 3.6: Surface pressure prediction using standard and shock-unsteadiness modified turbulence model [18] for supersonic flow over a compression corner geometry [17].

The standard turbulence models were developed for incompressible flows, and hence are bound to give inaccurate results for flows involving strong pressure gradients like shock waves. Several modifications have been proposed to improve the performance of the standard turbulence models for compressible flows, e.g., the realizability constraint, compressibility correction, rapid compression correction, length scale modification. These modifications are mostly empirical and they give improvement for the application over which it was tested under given test conditions.

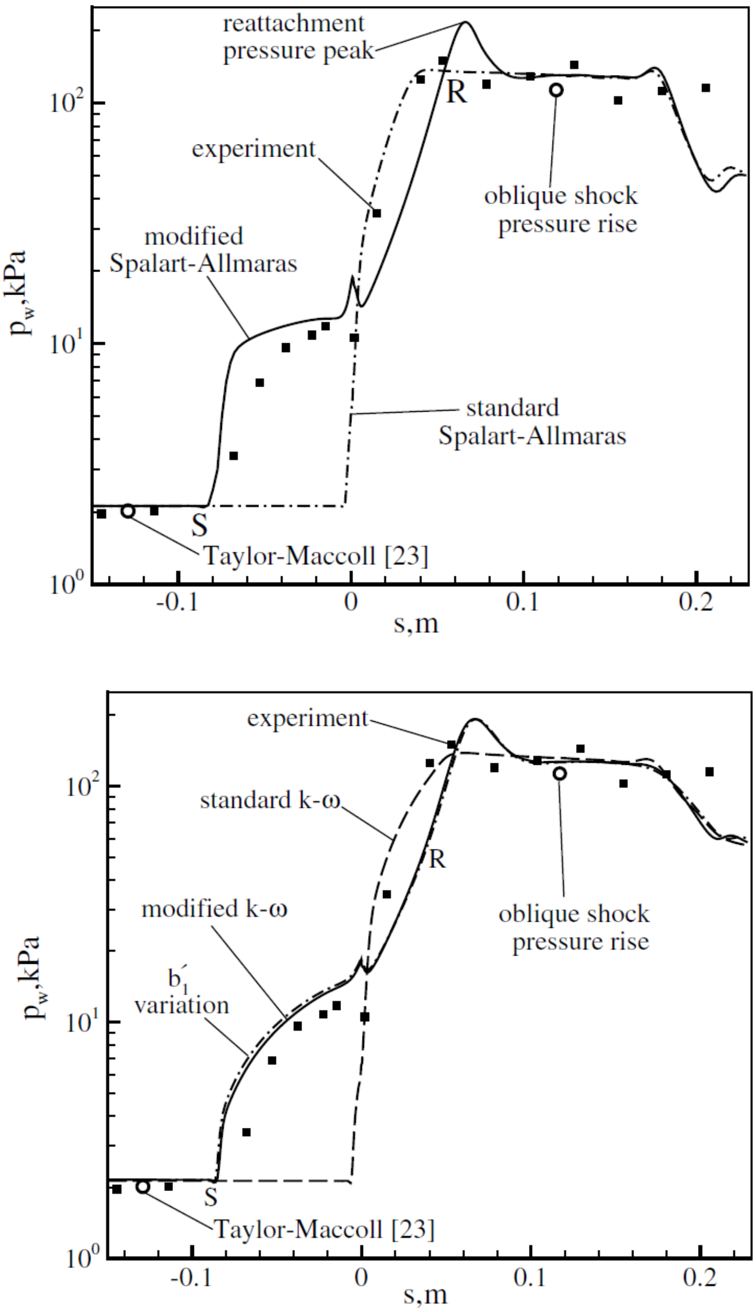

FIGURE 3.7: Wall pressure computed using (a) shock-unsteadiness modified Spalart-Allmaras model and (b) shock-unsteadiness k-ω turbulence model is compared with experimental data [50] for 36° flare at Mach 13.1 [51].

Sinha et al. [18] suggested an improvement to the k-ε turbulence model based on the study of the physics of unsteady motion of the shock wave. The flow-field generated by the interaction of shock wave with a turbulent boundary layer is inherently unsteady. The standard turbulence models do not account for the unsteady motion of the shock wave, and hence, for flows involving strong shock-wave/turbulent boundary layer interactions, the performance is poor. The shock-unsteadiness correction is discussed in detail in section 4.3 of chapter 4.

Fig. 3.6 shows the prediction of wall pressure distribution, for supersonic flow over a compression corner geometry, obtained using standard and shock-unsteadiness modified

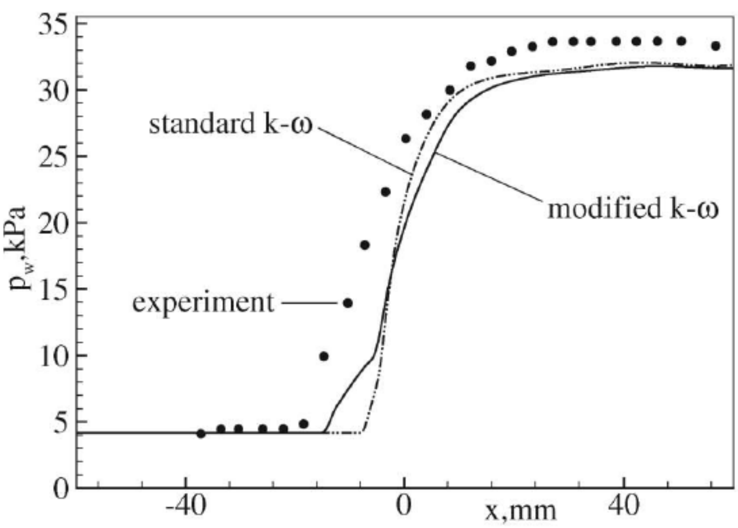

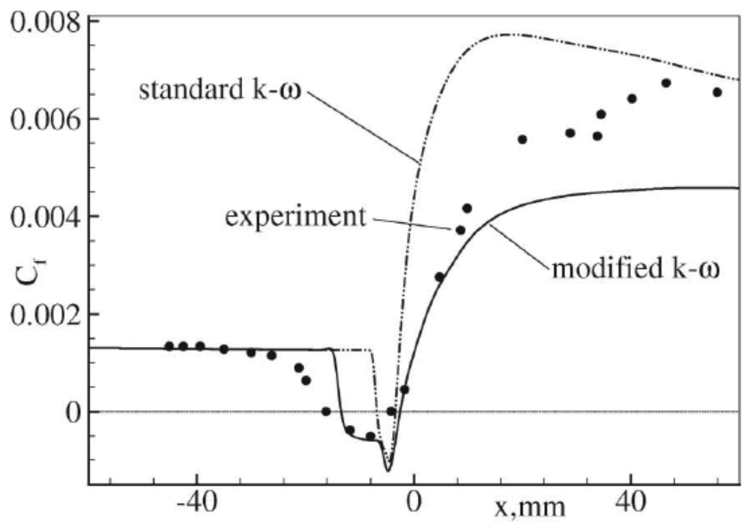

FIGURE 3.8: Computed (a) wall pressure and (b) skin friction coefficient compared with experimental data [52] for θ = 10° at M = 5 using standard k–ω and shock- unsteadiness modified k–ω models, .

turbulence models [17]. The standard k-ε and k-ω turbulence models under-predict the separation length as the predicted pressure rise is much downstream of the experimental data. With the application of shock-unsteadiness modification, the predicted pressure rise is much closer to the experimental data leading to better prediction of separation length as compared to the standard turbulence model.

Fig. 3.7 shows the comparison of computed pressure [51] with the experimental data [50] for M = 13.1 flow over a 36° flare geometry (see schematic in Fig. 3.2). The computed pressure data obtained using the shock-unsteadiness corrected Spalart-Allmaras model is shown in Fig. 3.7a. The separation length predicted by Spalart-Allmaras model is very small as compared to the experimental data. With the application of shock-unsteadiness modified Spalart-Allmaras model, the predictions are much closer to the experimental data. The pressure data obtained using the shock-unsteadiness corrected k-ω model is shown in Fig. 3.7b. As observed, the prediction using the shock-unsteadiness

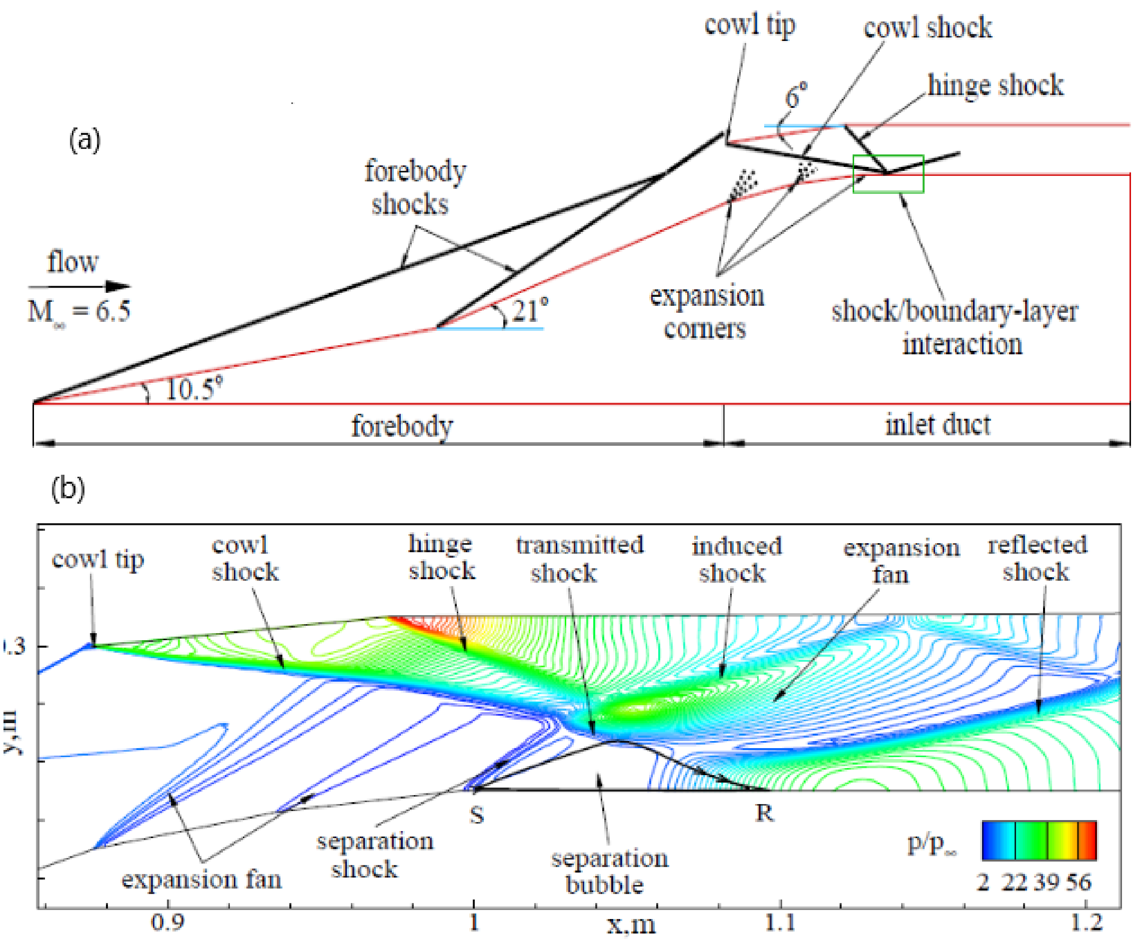

FIGURE 3.9: (a)Schematic of scramjet intake and (b) pressure contour of flow inside duct where separation is formed [53].

corrected k-ω model is closer the experimental data as compare to that predicted using the standard model.

Fig. 3.8 shows the comparison of computational predictions [44] with experimental data [52] for M = 5 flow with shock impinging (shock generator angle θ = 10°; see schematic in Fig. 2.5) on the flat plate. The pressure rise obtained using the modified k-ω turbulence model is much closer to the experimental data [52] as compared to the standard k-ω turbulence model. From the skin-friction coefficient plot, it is seen that the separation length predicted using the modified k-ω turbulence model is closer to the experimental data as compared to the standard k-ω turbulence model.

Pasha et al. [53] applied the shock unsteadiness modified Spalart-Allmaras turbulence

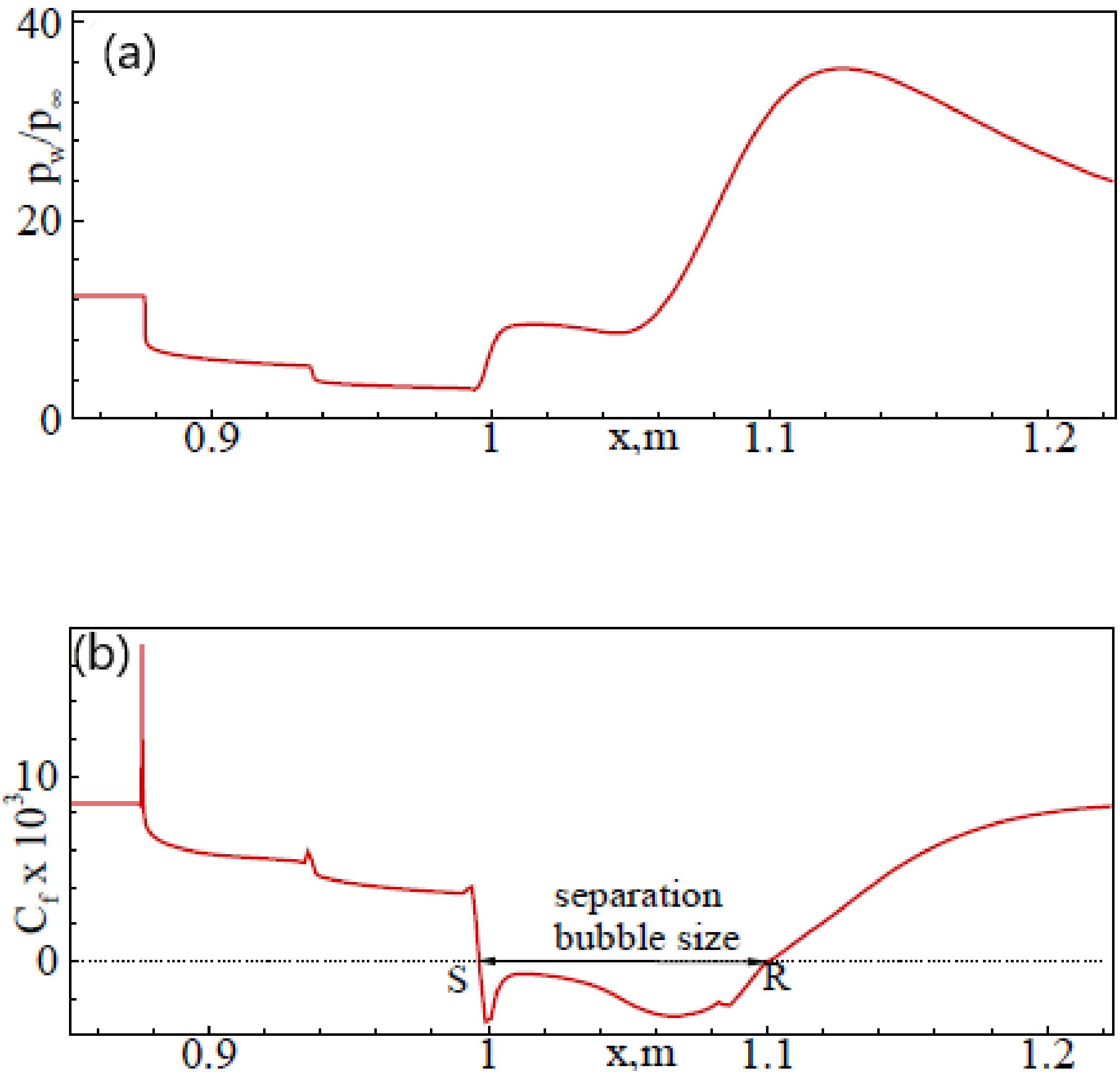

FIGURE 3.10: (a) Pressure and (b) skin-friction distribution over the surface of intake where separation is formed [53].

model for simulating the flow over a scramjet intake and predicted the separation length inside the duct. The model prediction was validated with the experimental data at M = 5 flow. Fig. 3.9a shows the schematic of scramjet intake for M = 6.5 flow. The geometry consists of two fore body ramps of 10.5° and 21° respectively, followed by three expansion corners, each of 7°, leading to the inlet duct. A separation bubble is formed inside the duct just after the expansion corner, highlighted by a square. The flow-field predictions of this region is discussed. Fig. 3.9b shows the pressure contour over the region, highlighted by square in Fig. 3.9a, which spans from X =0.9 at the expansion corner to X = 1.2 inside the duct. The cowl shock and hinge shock impinge on the turbulent boundary layer on the vehicle wall and form a re-circulation region. A separation shock is formed at the separation point and a shear layer develops over the separation bubble. Intersection of the separation and incident shocks generate the induced and transmitted shock waves. The flow turns over the separation bubble to generate an expansion fan. The compression waves generated by flow reattachment coalesce to form the reflected shock. There are multiple reflections of shocks and expansion waves in the duct. The surface pressure and skin-friction coefficient along the inlet bottom wall is shown in Fig. 3.10a and 3.10b, respectively. Pressure rises at flow separation, remains approximately constant along the separation bubble and rises to peak values in the reattachment region. The skin friction data shows a large negative region between the separation (S) and reattachment (R) points. The separation bubble is 104 mm long in the stream-wise direction and extends to about one third of the duct height.

3.4 Scaling law for separation length

Several empirical relations or scaling laws have been developed in the past which relate the interaction length (upstream influence or separation length) with the shock-strength. All these scaling laws give the relation between the normalized separation length and normalized shock-strength. However, all these empirical relations are for flows with laminar interaction [25], [34], [54], [55]. Souverin et al. [56] commented that normalization in the scaling laws given in literature is not satisfactory and show a disparity of upto 500%. Based on conservation of mass properties, Souverin et al. [56] proposed a modified normalization wherein the normalized interaction length ($L^\star$) and normalized shock strength ($S_e^\star$) is given as:

$$L^\star = \frac{L_{int}}{\delta^\star} \frac{sin\beta sin\theta}{sin(\beta-\theta)} \tag{3.1}$$

$$S_e^{\star} = \frac{2k}{\gamma}\frac{(P_2/P_1 - 1)}{M_e^2} \tag{3.2}$$

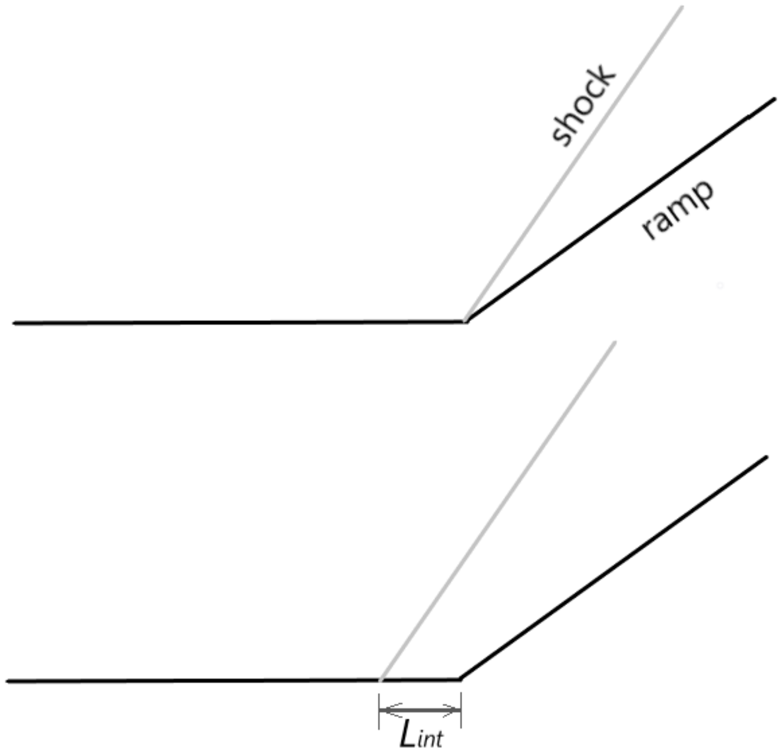

FIGURE 3.11: Definition of interaction length L_{int} for compression corner geometry

where L_{int} is the observed upstream shift of shock wave from the inviscid case due to swelling of the boundary layer (see Fig. 3.11) . $\delta^{\star}$ is displacement thickness upstream of the interaction, β is shock angle and θ is deflection or ramp angle. $S_e^{\star} < 1$ is the normalized interaction strength where P_2/P_1 is the pressure jump across the shock, M_e^2 is free-stream or edge Mach number and k is a constant with value of $k = 3$ for Re_θ < 1e+5 and $k = 4$ for Re_θ > 1e+5. Re_θ is a Reynolds number based on momentum thickness. The scaling law is applicable for turbulent interactions.

$$y = ax^b \tag{3.3}$$

Further, if $L_{int} < 1$ then flow is attached. If $1 < L_{int} < 2$ then flow is in incipient separation, and if $L_{int} > 2$ then flow is fully separated. Similarly, if $S_e^{\star} < 1$ then flow is attached and if $S_e^{\star} > 1$ then the flow is separated. Souverin suggests plotting $L^{\star}$ with $S_e^{\star}$ as it would collapse the data along a single line irrespective of Mach number, Reynolds number or geometry type (reflection or ramp shock) as shown in Fig. 3.12 where symbols

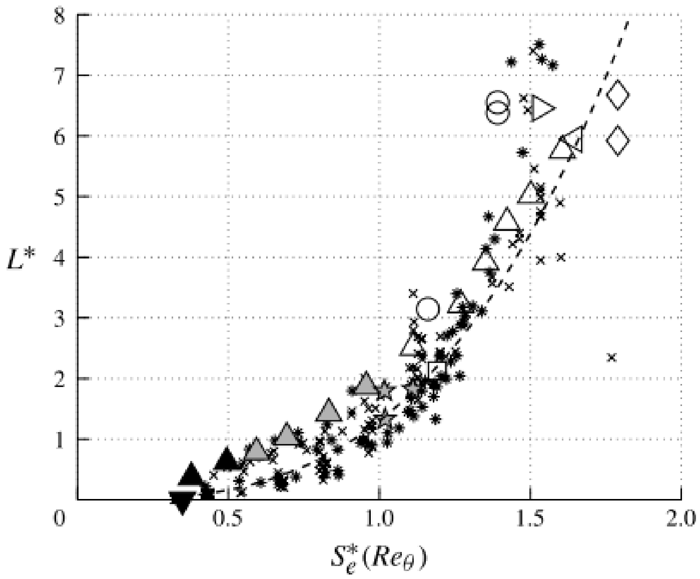

FIGURE 3.12: Normalized separation length $L^{\star}$ versus shock-strength $S_e^{\star}$; colors represent the separation state: black - attached; gray - incipient; white - separated

correspond to different experiments [56]. All the data is found to scattered over a line, and best fit line was found to follow the Eq. 3.3, where a = 1.3 and b = 3 are constants. All the data found to follow this equation irrespective of geometry (compression ramp or incidence shock reflection).

3.5 Shock-turbulence interaction

In aerospace applications involving shock interacting with boundary layer, the flow separates leading to formation of separation bubble in the boundary layer. Presence of the separation bubble alters the surface properties thereby affecting the aerodynamic characteristics of the vehicle. Hence, accurate prediction of separation length is important. The complexity of the problem makes the analysis for model improvement difficult. However, the problem of the turbulence interacting with normal shock wave is a similar problem, rich in physics and does not involve complexities due to boundary layer, shear-layer or flow-separation at wall. This problem of turbulence interacting with normal shock wave is frequently studied in literature for model improvement.

The problem of normal shock wave interacting with turbulence has been studied by various researchers ([11], [12], [13], [14], [15], [16]) in literature. In the present work, the work done by Larsson et al. [12] is considered for the study of shock-turbulence interaction problem. Larsson et al. [12] presents DNS of shock interacting with turbulence for the analysis of different turbulent quantities (like Reynolds stresses, turbulent length scale, etc.) across a normal shock. The results presented in Chapter-5 make use of the DNS data for validation and comparison of the results. The details are discussed in brief in following subsections.

In the DNS simulations of Larsson et al [12], the domain length in x, y and z-direction were 4π, 2π and 2π respectively. In x-direction the domain ranged from [-1.96, 10.61].

TABLE 3.1: Details of DNS data corresponding to various Mach number used in validation [12].

M	M_t	Re_λ	Re_L	DNS source
1.5	0.22	40	5.56×10^2	Larsson & Lele [12]
2.0	0.22	40	7.48×10^2	
2.5	0.22	40	9.35×10^2	Larsson & Lele [12]
3.0	0.22	40	1.12×10^3	Larsson & Lele [12]
3.5	0.22	40	1.31×10^3	
4.25	0.22	40	1.59×10^3	Larsson & Lele[12]
4.7	0.22	40	1.76×10^3	

In order to facilitate comparison with linear analysis, the stream-wise co-ordinate was scaled by the wave number (κ_0 = 4) of most energetic wave, having a wavelength of $L^\star$ = κ_0, (superscript $\star$ indicates the quantity is dimensional) upstream of the shock. Thus, the domain length after the normalization was equal to $X = X^\star/L^\star = X^\star\kappa_0$ = [-7.84, 42.12]. Further, the stream-wise coordinate was shifted such that the nominal position of the shock was at X = 0 with inflow occurring at approximately at $X \simeq$ -8 and outflow at $X \simeq 42$. The DNS data sets were available for different mach numbers ranging from M = 1.05 to M = 6.0 with different turbulent Mach numbers M_t (equal to 0.05, 0.16, 0.22, 0.27, 0.31, 0.38 depending on the Mach number) and different Reynolds number based on Taylor micro-scale Re_λ (which is either 40 or 75). Table 3.1 shows the list of data sets that were used for the validation study. All the values listed here correspond to conditions just upstream of the shock.

Fig. 5.2a shows the evolution of turbulent kinetic energy across a normal shock located at X = 0 location. The location just upstream of shock is designated by subscript 1 and accordingly the TKE at this location is k_1. Similarly, the location just downstream of shock is designated by subscript 2 and the TKE at this location is designated as k_2. The location at the inlet of the domain is denoted by subscript 0 and thus the TKE at this location is k_0. Same notation is followed for the other turbulent variable ε i.e., ε_1 is before shock, ε_2 is after shock and ε_0 at the inlet of domain. Fig. 5.2b shows the profile of TKE normalized by k_1 i.e., k/k_1 vs X. Subsequently, the value of TKE at location just

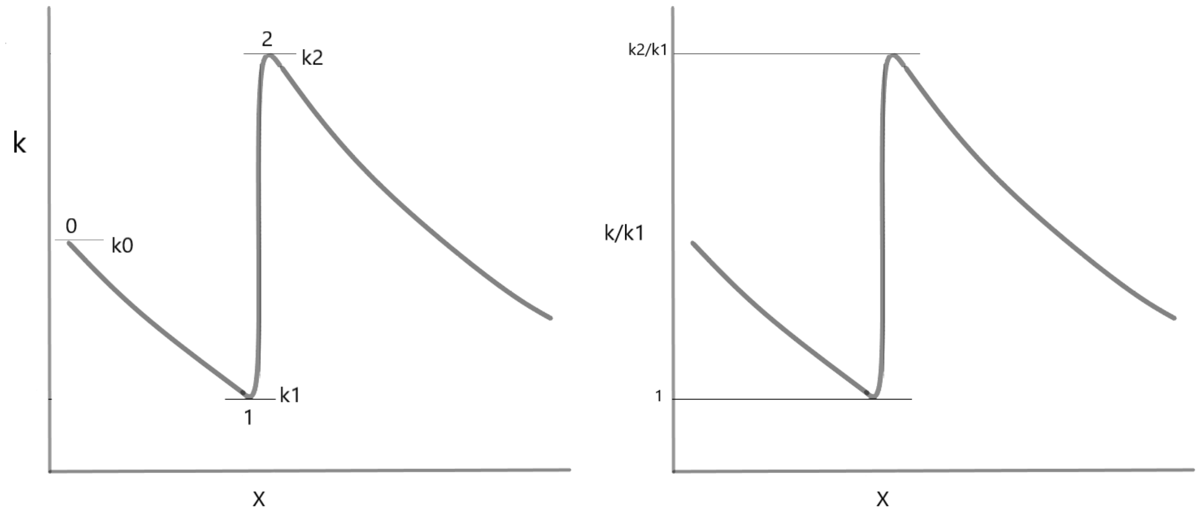

(a) Before normalization (b) After normalization

FIGURE 3.13: Schematic of evolution of turbulent kinetic energy k across a normal shock (a) before the normalization and (b) after the normalization

upstream of shock is unity and value of TKE at just downstream of shock corresponds to amplification of TKE across the shock and is given by k_2/k_1.

Using the values given in Table 3.1 which correspond to conditions just upstream of the shock, the turbulent variables k_1 and ε_1 can be computed using the following relations [21],

$$k = \frac{1}{2} M_t^2 a^2 \tag{3.4}$$

$$\varepsilon = \frac{10 \nu k}{\lambda^2} \tag{3.5}$$

$$Re_\lambda = \frac{\bar{\rho} u_{rms} \lambda}{\mu} \tag{3.6}$$

Now, the above computed values can be extrapolated to the inlet of the domain, and these extrapolated values will be the initial condition for the simulations. The initial conditions, k_0 and ε_0 at the inlet, can be extrapolated using the relations given by [47]

$$k_1 = k_0 \left(1 + \frac{x'}{\bar{u} n} \frac{\varepsilon_0}{k_0}\right)^{-n} \tag{3.7}$$

$$\varepsilon_1 = \frac{\varepsilon_0}{n} \left(1 + \frac{x'}{\bar{u} n} \frac{\varepsilon_0}{k_0}\right)^{-n-1} \tag{3.8}$$

where n is the index given by $n = 1/(C_2 - 1)$. The average values of turbulent quantities k and ε (in y-z plane of DNS data) were computed at each location in stream-wise direction. These averaged values were used for comparison of present results obtained using RANS simulations. The domain range in RANS simulations was approximately similar to that in DNS i.e., inflow at approximately X = -8 and outflow at X = 42. Since the objective of the current study is to analyze the amplification of turbulent quantities across a normal shock, the y- and z-direction were not considered in the RANS simulations.

3.6 Summary

The changes in separation length with different flow parameters, and scaling of separation length for flows involving shock interacting with boundary layer in turbulent regime are discussed. The inverse relation between Mach number and separation length is known but the reasoning behind it is not clear or well understood. There is no consistency in the published results regarding the dependence of separation length on Reynolds number Re_δ. The separation length predictions, using the standard and modified turbulence model, are discussed. The modified turbulence models give better predictions as compared to the standard turbulence models. The shock unsteadiness k-ε and k-ω have shown good potential in predicting separation length in compression ramp and oblique shock impingement cases. They have been tested for a variety of Mach numbers in the supersonic and hypersonic range. The shock unsteadiness model will be used in this thesis for predicting shock induced flow separation in compression ramp and scramjet intake configurations. The scaling of separation length for flow involving shock interacting with turbulent boundary layer is discussed. Finally, the problem of shock-turbulence interaction is covered along with the discussion of the relevant turbulent quantities.

Chapter 4

Simulation methodology

In this chapter, the equations governing the motion of fluid followed by the turbulence model used for closure are discussed. This is followed by the numerical method used to solve the equation and the boundary conditions used in the simulations.

4.1 Governing equations

The basic governing equations are continuity (4.1), momentum (4.2) and energy (4.3) equation as given below [21]

$$\frac{\partial \rho}{\partial t} + \frac{\partial (\rho u_i)}{\partial x_i} = 0 \tag{4.1}$$

$$\frac{\partial (\rho u_i)}{\partial t} + \frac{\partial (\rho u_j u_i)}{\partial x_j} = -\frac{\partial p}{\partial x_i} + \frac{\partial (t_{ji})}{\partial x_j} \tag{4.2}$$

$$\frac{\partial}{\partial t}\left[\rho\left(e + \tfrac{1}{2}u_i u_i\right)\right] + \frac{\partial}{\partial x_j}\left[\rho u_j\left(h + \tfrac{1}{2}u_i u_i\right)\right] = -\frac{\partial q_{L,j}}{\partial x_j} + \frac{\partial}{\partial x_i}(u_i t_{ij}) \tag{4.3}$$

where ρ, u_i, t, x_i, t_{ij}, e, h and $q_{L,j}$ are the density, velocity vector, time, coordinate vector, viscous stress tensor, internal energy, enthalpy, and laminar heat flux vector, respectively. The fluid considered is assumed to be a Newtonian fluid so that the viscous stress can be considered to be proportional to the traceless strain tensor. Viscous stress tensor characterizes the specific properties of the fluid when subjected to mechanical stress and is modeled as given below.

$$t_{ij} = 2\mu S_{ij} - \zeta \frac{\partial u_k}{\partial x_k}\delta_{ij} \tag{4.4}$$

where ζ is modeled assuming Stokes hypothesis as $\zeta = -\frac{2}{3}\mu$ and $S_{ij} = \frac{1}{2}\left(\frac{\partial u_i}{\partial x_j} + \frac{\partial u_j}{\partial x_i}\right)$ being the strain rate tensor. The dynamic viscosity, which is a function of temperature, can be modeled using Sutherland's Law given by

$$\mu = \mu_{ref}\left(\frac{T_{ref}+S}{T+S}\right)\left(\frac{T}{T_{ref}}\right)^{\frac{3}{2}} \tag{4.5}$$

where T_{ref} = 110.3° K is the reference temperature and μ_{ref} = 1.716E-5 kg/m.s is the reference viscosity and S = 110.56 K is the constant in the equation. Heat flux is modeled using the Fourier's law of heat conduction and is given as,

$$q_{L,j} = \kappa\frac{\partial T}{\partial x_j} \tag{4.6}$$

κ being thermal conductivity of the fluid and can be expressed as κ = μc_p/Pr. Symbol c_p is the specific heat at constant pressure and Pr is the Prandtl number. In order to close the system, the fluid considered is assumed to be a calorically perfect gas, which gives an additional relation

$$p = \rho RT \tag{4.7}$$

Assuming the fluid to be caloricaly perfect gas, the specific heats become constant and are related to the internal energy and specific enthalpy as given below.

$$e = c_v T \tag{4.8}$$

$$h = c_p T \tag{4.9}$$

where c_p and c_v are the heat capacity at constant pressure and constant volume respectively. The heat capacities are related by following relations: $c_p - c_v = R$ and $c_p/c_v = \gamma$. The specific gas constant R is equal to 287.058 J/kg.K for air. The heat capacity ratio γ, which is constant for air, is equal to 1.4.

4.2 Reynolds-averaged Navier-Stokes equations

For turbulent motion, the flow variable in the governing equations are split into its mean, and fluctuating component which can be Reynolds averaged or Favre-averaged. Reynolds averaging is an averaging procedure carried out over a variable quantity in a turbulent flow. The average is usually taken over a time period T and is given as

$$\bar{\phi}(x,t) = \frac{1}{T}\lim_{T\to\infty}\int_t^{T+t}\phi(x,t)dt \tag{4.10}$$

$\bar{\phi}$ represents the Reynolds-averaged quantity and ϕ is instantaneous quantity at a given location and time. The Favre-averaging is based on density weighted time averaging and is given as

$$\widetilde{\phi}(x,t) = \frac{1}{\bar{\rho}} \lim_{T\to\infty} \int_{t}^{T+t} \rho(x,t)\ \phi(x,t)\ dt \tag{4.11}$$

$\widetilde{\phi}$ represents the Favre-averaged quantity. The averaging procedure is discussed in detail in Appendix-A. The variables in the Navier-Stokes equations are split into the Favre-averaged as well as Reynolds-averaged mean and fluctuating quantities (see Appendix-A for details). The Reynolds averaging the equations is carried out to get the Reynolds-averaged Navier-Stokes equations given as following [57]:

$$\frac{\partial \bar{\rho}}{\partial t} + \frac{\partial}{\partial x_i}(\bar{\rho}\widetilde{u}_i) = 0 \tag{4.12}$$

$$\frac{\partial}{\partial t}(\bar{\rho}\widetilde{u}_i) + \frac{\partial}{\partial x_j}(\bar{\rho}\widetilde{u}_j\widetilde{u}_i) = -\frac{\partial \bar{p}}{\partial x_i} + \frac{\partial}{\partial x_j}\left[\bar{t}_{ji} - \overline{\rho u_j'' u_i''}\right] \tag{4.13}$$

$$\begin{aligned}\frac{\partial}{\partial t}(\bar{\rho}E) + \frac{\partial}{\partial x_j}(\bar{\rho}\widetilde{u}_j H) =& \frac{\partial}{\partial x_j}\left[-q_{L,j} - \overline{\rho u_j'' h''}\right] + \frac{\partial}{\partial x_j}\left[\widetilde{u}_i(\bar{t}_{ji} - \overline{\rho u_i'' u_j''})\right] \\ &+ \frac{\partial}{\partial x_j}\left[\overline{t_{ji}u_i''} - \overline{\rho u_j'' \tfrac{1}{2} u_i'' u_i''}\right]\end{aligned} \tag{4.14}$$

The quantities E and H are total energy and total enthalpy respectively, and include the kinetic energy of fluctuating turbulent field,viz., [21]

$$E = \widetilde{e} + \frac{1}{2}\widetilde{u}_i\widetilde{u}_i + \tfrac{1}{2}\overline{u_i'' u_i''} \quad \textit{and} \quad H = \widetilde{h} + \frac{1}{2}\widetilde{u}_i\widetilde{u}_i + \tfrac{1}{2}\overline{u_i'' u_i''} \tag{4.15}$$

After averaging, the continuity equation remains the same, the momentum equations has one extra term, and the energy equation has four extra terms.

- $-\overline{\rho u_i'' u_j''} = \tau_{ij}$ is the Reynolds stress tensor term

- $-\overline{\rho u_i'' h_j''} = q_{t,j}$ is the turbulent heat flux term

- $\frac{1}{2}\overline{u_i'' u_i''} = k$ is the turbulent kinetic energy

- $\overline{\rho u_j'' \frac{1}{2} u_i'' u_i''}$ is the turbulent transport of TKE

- $\overline{t_{ji} u_i''}$ is the molecular diffusion of TKE

The turbulent heat flux is assumed to be proportional to temperature gradient (Gradient diffusion hypothesis) [21]

$$\overline{\rho u_i'' h_j''} = q_{T,j} = -\frac{\mu_t c_p}{Pr_t}\frac{\partial \widetilde{T}}{\partial x_j} = -\frac{\mu_t}{Pr_t}\frac{\partial \widetilde{h}}{\partial x_j} \tag{4.16}$$

where Pr_t is the turbulent Prandtl number and is equal to $Pr_t = 0.89$. The turbulent transport and the molecular diffusion of TKE are together modeled as given below [21].

$$\overline{t_{ji} u_i''} + \overline{\rho u_i'' u_i'' u_j''} = \frac{\partial}{\partial x_j}\left[(\mu + \frac{\mu_t}{\sigma_k})\frac{\partial k}{\partial x_j}\right] \tag{4.17}$$

wher μ_t is the eddy-viscosity and $\sigma_k = 1.0$ is the constant in the equation.

4.3 Turbulence closure

The averaging of Navier-Stokes equations introduces an unknown Reynolds stress term in the equation. The Reynolds stress is modeled using the Boussinesq assumption in terms of eddy-viscosity.

The Reynolds stress equation models solve the transport equation for the Reynolds stress $R_{ij} = -\overline{\rho u_i'' u_j''} = -\tau_{ij}/\rho$ and is given as [21], [58], [59]

$$\frac{DR_{ij}}{Dt} = D_{ij} + P_{ij} + \pi_{ij} + \omega_{ij} - \varepsilon_{ij} \tag{4.18}$$

This equation can be summarized as: Rate of change of R_{ij} + Transport of R_{ij} by convection = Transport of R_{ij} by diffusion + Rate of production of R_{ij} + Transport of R_{ij} due to turbulent pressure-strain interactions + Transport of R_{ij} due to rotation + Rate of dissipation of R_{ij}. The six partial differential equations represent the six independent Reynolds stresses. Only the production term P_{ij} is closed and does not require any modeling while the other terms are unclosed and require a closure model. Reynolds stress models account for the directional effects of the Reynolds stresses and the complex interactions in turbulent flows. They offer significantly better accuracy than eddy-viscosity based turbulence models, but (i) are computationally expensive, (ii) require high-quality mesh, and (iii) require more number of equations to be solved. Due to their complexity, the understanding of Reynolds stress models is limited. The Reynolds stress can be related to mean velocity gradients and eddy viscosity using the gradient diffusion hypothesis.

$$-\overline{\rho u_i'' u_j''} = \tau_{ij} = 2\mu_t \left(S_{ij} - \frac{1}{3}\frac{\partial \widetilde{u}_k}{\partial x_k}\delta_{ij} \right) - \frac{2}{3}\bar{\rho} k \delta_{ij} \tag{4.19}$$

where μ_t is the turbulent viscosity, S_{ij} is the mean rate of strain tensor and δ_{ij} is the kronecker delta. The eddy viscous turbulence models have a limitation that they fail to take into account - the anisotropy in normal stresses, the streamline curvature effects, secondary/swirling flows and three dimensional flows. However, the eddy viscous turbulence models are widely used as it requires solving only one or two extra equations and is computationally economical. The modeling of the Reynolds stress creates a new unknown - turbulent viscosity μ_t which is modeled in terms of two new variables turbulent kinetic energy k and rate of the dissipation of turbulent kinetic energy ε. So two more equations are needed to solve these two unknowns along with the RANS equations for turbulence closure, and is discussed in the following section.

The equation for the standard k-ε model of Launder and Sharma [60] is given

$$\begin{aligned} \frac{\partial}{\partial t}(\bar{\rho} k) + \frac{\partial}{\partial x_j}(\bar{\rho} k \widetilde{u_j}) =& P_k + D_k + \frac{\partial}{\partial x_j}\left[\left(\mu + \frac{\mu_t}{\sigma_k} \right) \frac{\partial k}{\partial x_j} \right] \\ & - 2\mu \left(\frac{\partial \sqrt{k}}{\partial x_j} \right)^2 \end{aligned} \tag{4.20}$$

$$\begin{aligned} \frac{\partial}{\partial t}(\bar{\rho}\varepsilon) + \frac{\partial}{\partial x_j}(\bar{\rho}\varepsilon\widetilde{u_j}) = & P_k \frac{\varepsilon}{k} C_{\varepsilon_1} + D_k \frac{\varepsilon}{k} C_{\varepsilon_2} f_2 + \frac{\partial}{\partial x_j}\left[\left(\mu + \frac{\mu_t}{\sigma_\varepsilon} \right) \frac{\partial \varepsilon}{\partial x_j} \right] \\ & + 2\,\frac{\mu \mu_T}{\bar{\rho}} \left(\frac{\partial^2 \widetilde{u}_i}{\partial x_j \partial x_j} \right) \end{aligned} \tag{4.21}$$

where $P_k = -\overline{\rho u_i'' u_j''}\dfrac{\partial u_i}{\partial x_j}$ is the production term and $D_k = -\rho\varepsilon$ is the dissipation term.
The eddy viscosity is modeled as $\mu_t = c_\mu f_\mu \dfrac{\bar{\rho} k^2}{\varepsilon}$ where

$$f_\mu = exp\left[\frac{-3.4}{(1+0.02R_t)^2} \right]; \quad R_t = \frac{\bar{\rho} k^2}{\mu\varepsilon}; \quad f_2 = 1 + 0.3e^{-R_t^2};$$

The constants are given by $C_{\varepsilon_1} = 1.44$, $C_{\varepsilon_2} = 1.92$, $\sigma_k = 1.0$, $\sigma_\varepsilon = 1.3$ and $c_\mu = 0.09$.
The mechanisms in the k and ε equations can be summarized as

Rate of change of k or ε + Transport of k or ε by convection = Production of k or ε + Dissipation of k or ε + Diffusion of k or ε + low Reynolds number correction for k or ε

The shock motion, caused by the upstream turbulent fluctuations, results in a damping of the TKE at the shock wave. Sinha et al. [18] studied this mechanism using linear interaction analysis and proposed the following modification for the net production of TKE at the shock wave:

$$P_k = -\overline{\rho u_i'' u_j''} \frac{\partial u_j}{\partial x_i} c_0 \tag{4.22}$$

Here shock-unsteadiness correction $c_0 = 1 - b_1'$ is added to the production term where b_1' is the damping factor given by

$$b_1' = max(0, 0.4(1 - e^{1-M_{1n}})) \tag{4.23}$$

The value of b_1' is zero in subsonic region whereas in supersonic regions it reaches an asymptotic value of 0.4 for high Mach numbers. In order to match the value of k in the shock to that prescribed in Eq. 4.22, μ_t is replaced by $c_\mu' \mu_t$ where c_μ' is given as

$$c_\mu' = 1 - f_s \left[1 + (b_1'/\sqrt{3})/\zeta c_\mu f_\mu\right] \tag{4.24}$$

where $\zeta = Sk/\widetilde{\varepsilon}$ and $\widetilde{\varepsilon} = \varepsilon + 2\nu(\partial\sqrt{k}/\partial x_j)^2$ is the total dissipation rate obtained by adding the low Reynolds number term in the k-equation to the turbulent diffusion rate [60]. The term f_s is an empirical relation that defines the regions of shock wave in terms of S_{ii}/S:

$$f_s = \frac{1}{2} - \frac{1}{2} tanh(5S_{ii}/S + 3) \tag{4.25}$$

such that f_s = 1 in regions of high compression and is equal to 0 otherwise. This model, proposed for decaying homogeneous shock-turbulence interaction, was subsequently applied for shock-boundary layer interaction cases [17]. The size of the separation bubble mainly depends on the turbulence in the boundary layer flows subjected to an adverse pressure gradient. The separation bubble length predicted by the standard k-ε turbulence model is always smaller than that observed in experiments due to the over-prediction of the turbulent kinetic energy across the shock wave [18]. By implementing the shock-unsteadiness modification to the standard models, the turbulent kinetic energy across the shock wave gets damped, and hence the separation bubble is well-predicted as compared to standard models and is closer to available experimental data [17].

4.4 Numerical method

In order to solve the governing equations, the computational domain is discretized into required number of grid points, and the governing equations are simplified to algebraic form. These discretized governing equations can be obtained by different techniques like - finite volume method, finite element method, or finite difference method. The discussion here is restricted to finite volume method.

Finite Volume Formulation

The governing equations can be written in vector form as given below

$$\frac{\partial U}{\partial t} + \frac{\partial F'}{\partial x} + \frac{\partial G'}{\partial y} = S \tag{4.26}$$

$$U = \begin{pmatrix} \rho \\ \rho u \\ \rho v \\ \rho E \\ \rho k \\ \rho \varepsilon \end{pmatrix} \quad F_I = \begin{pmatrix} \rho u \\ \rho u^2 + p \\ \rho uv \\ (\rho E + p)u \\ \rho uk \\ \rho u\varepsilon \end{pmatrix} \quad G_I = \begin{pmatrix} \rho v \\ \rho uv \\ \rho v^2 + p \\ (\rho E + p)v \\ \rho vk \\ \rho v\varepsilon \end{pmatrix} \tag{4.27}$$

where

$$\begin{aligned} F' &= F_I + F_V \\ G' &= G_I + G_V \\ F &= F' + G' \end{aligned} \tag{4.28}$$

$$F_v = \begin{pmatrix} 0 \\ t_{xx} + \tau_{xx} \\ t_{xy} + \tau_{xy} \\ (t_{xx} + \tau_{xx})\tilde{u} + (t_{xy} + \tau_{xy})\tilde{v} + (\kappa + \kappa_t)\dfrac{\partial T}{\partial x} + (\mu + \sigma_k \mu_t)\dfrac{\partial k}{\partial x} \\ (\mu + \sigma_k \mu_t)\dfrac{\partial k}{\partial x} \\ (\mu + \sigma_\varepsilon \mu_t)\dfrac{\partial \varepsilon}{\partial x} \end{pmatrix} \tag{4.29}$$

$$G_v = \begin{pmatrix} 0 \\ t_{xy} + \tau_{xy} \\ t_{yy} + \tau_{yy} \\ (t_{xy} + \tau_{xy})\tilde{u} + (t_{yy} + \tau_{yy})\tilde{v} + (\kappa + \kappa_t)\dfrac{\partial T}{\partial y} + (\mu + \sigma_k \mu_t)\dfrac{\partial k}{\partial y} \\ (\mu + \sigma_k \mu_t)\dfrac{\partial k}{\partial y} \\ (\mu + \sigma_\varepsilon \mu_t)\dfrac{\partial \varepsilon}{\partial y} \end{pmatrix} \tag{4.30}$$

$$S = \begin{pmatrix} 0 \\ 0 \\ 0 \\ 0 \\ P_k C_0 + D_k \\ P_k \dfrac{\varepsilon}{k} C_1 + D_k \dfrac{\varepsilon}{k} C_2 \end{pmatrix} \tag{4.31}$$

where U is a vector of conservative variables. F_I and G_I are the vector of convective terms in the x-direction and y-direction respectively while F_V and G_V being the vector of viscous terms in the x-direction and y-direction respectively. S is a vector containing the turbulent source terms. In conservative form, the governing equations can be written as

[61]

$$\frac{\partial U}{\partial t} + \vec{\nabla}.\vec{F} = 0 \tag{4.32}$$

$$\int\int\int \frac{\partial U}{\partial t} dV + \int\int\int \vec{\nabla}.\vec{F} dV = 0 \tag{4.33}$$

$$\frac{\partial}{\partial t}(U_{ij}V_{ij}) + \oiint \vec{F}.(\hat{n} dS) = 0 \tag{4.34}$$

$$\frac{\partial U_{ij}}{\partial t} = -\frac{1}{V_{ij}} \sum_{4faces} \vec{F}\vec{S}_{face} \tag{4.35}$$

$$\begin{aligned}\frac{\partial U_{ij}}{\partial t} = \frac{1}{V_{ij}}[&\vec{F}_{i+1/2,j}S_{i+1/2,j} + \vec{F}_{i-1/2,j}S_{i-1/2,j} + \\ &\vec{G}_{i,j+1/2}S_{i,j+1/2} + \vec{G}_{i,j-1/2}S_{i,j-1/2}]\end{aligned} \tag{4.36}$$

The side vector $\vec{S}$ and area vector V_{ij} is computed as given below

$$\begin{aligned} S_{i+1/2,j} &= +(y_{i+1,j+1} - y_{i+1,j})\hat{i} - (x_{i+1,j+1} - x_{i+1,j})\hat{j} \\ S_{i-1/2,j} &= -(y_{i,j+1} - y_{i,j})\hat{i} - (x_{i,j+1} - x_{i,j})\hat{j} \end{aligned} \tag{4.37}$$

$$\begin{aligned} V_{ij} = &|(x_{i,j} - x_{i+1,j})y_{i+1,j+1} + (x_{i+1,j} - x_{i+1,j+1})y_{i+1,j} + (x_{i+1,j} - x_{i,j})y_{i+1,j}| + \\ &|(x_{i,j} - x_{i+1,j+1})y_{i,j+1} + (x_{i+1,j+1} - x_{i,j+1})y_{i,j} + (x_{i,j+1} - x_{i,j})y_{i+1,j+1}| \end{aligned} \tag{4.38}$$

The convective fluxes ($\vec{F_I}$ and $\vec{G_I}$) are computed using the low-dissipation Steger-Warming method while the viscous components ($\vec{F_V}$ and $\vec{G_V}$) are computed using the central difference method.

Convective Fluxes

The convective terms which dominate the inviscid region are hyperbolic and are solved using the Steger-Warming flux-splitting method [62]. The governing equations in vector form can be written as,

$$\frac{\partial U}{\partial t} + \frac{\partial F}{\partial x} = 0 \tag{4.39}$$

where U is a vector of conservative variables and F is a vector of convective variables in x-direction given as

$$F = \begin{pmatrix} \rho u \\ \rho u^2 + p \\ \rho v \\ (\rho E + p)u \end{pmatrix} \tag{4.40}$$

Since the convective fluxes are homogeneous in the vector of conservative variables, the flux vector can be linearized to express it in terms of Jacobian matrices. Accordingly, the Eq. 4.39 can be re-written as

$$\frac{\partial U}{\partial t} + \frac{\partial F}{\partial U}\frac{\partial U}{\partial x} = 0 \tag{4.41}$$

where $\frac{\partial F}{\partial U}$ = A is the Jacobian matrix and is computed as given in the Appendix-B. The next step is to split the fluxes into the positive moving and negative moving components. For the Steger-Warming method, the sign (positive/negative) of the eigenvalues of the Jacobian is used for this purpose. To calculate the eigenvalues and eigenvectors of the Jacobian, first, the Jacobian matrice is broken into components that will make the task easier. In Eq. 4.41, the Jacobian $\frac{\partial F}{\partial U}$ can be written as

$$\frac{\partial F}{\partial U} = \frac{\partial F}{\partial V}\frac{\partial V}{\partial U} \tag{4.42}$$

where V is vector of primitive variables and these primitive variables are not unique but chosen for convenience.

$$V = \begin{pmatrix} \rho \\ u \\ v \\ p \end{pmatrix} \tag{4.43}$$

Further the Jacobian can also be re-written as,

$$\frac{\partial F}{\partial U} = \frac{\partial F}{\partial V}\frac{\partial V}{\partial U} = \frac{\partial U}{\partial V}\frac{\partial V}{\partial U}\frac{\partial F}{\partial V}\frac{\partial V}{\partial U} \tag{4.44}$$

where $\frac{\partial U}{\partial V}$ and $\frac{\partial V}{\partial U}$ are transformation matrices between primitive and conservative variables and are denoted by S^{-1} and S, respectively. This transformation is made because the remaining matrix $\frac{\partial F}{\partial V}\frac{\partial V}{\partial U}$ is easier to diagonalize than A. Using linear algebra, the term $\frac{\partial U}{\partial V}\frac{\partial V}{\partial U}\frac{\partial F}{\partial V}\frac{\partial V}{\partial U}$ can now be diagonalized as

$$A = S^{-1}C^{-1}\Lambda CS \tag{4.45}$$

where Λ is the diagonal matrix of eigenvalues of the system while C^{-1} and C are the left and right eigen matrices. The diagonal matrix Λ can be split into Λ^{+} and Λ^{-} based on the sign of the eigenvalues.

$$\begin{aligned} A =& S^{-1}C^{-1}\Lambda^{+}CS + S^{-1}C^{-1}\Lambda^{-}CS \\ =& A^{+} + A^{-} \end{aligned} \tag{4.46}$$

where Λ^{+} and Λ^{-} are split eigenvalue matrices consisting only of positive and negative eigenvalues respectively. A^{+} and A^{-} are the corresponding positive and negative Jacobian. The expression for these matrices is given in Appendix-B. The flux vector can now be split into positive (F^{+}) and negative (F^{-}) components, based on the sign of eigen values, as given below,

$$\begin{aligned} F =& AU \\ =& (A^{+} + A^{-})U \\ =& A^{+}U + A^{-}U \\ =& F^{+} + F^{-} \end{aligned} \tag{4.47}$$

The total inviscid flux through each cell-face can now be expressed as the sum of positive flux and negative flux components from the cell center, as given below (see Fig.

4.1),

$$
\begin{aligned}
F_{i+1/2} =& F^{+}_{i+1/2} + F^{-}_{i+1/2} \\
=& (A^{+}_{i,j} + A^{-}_{i+1,j})U \\
=& A^{+}_{i,j} U_{i,j} + A^{-}_{i+1,j} U_{i+1,j} \\
=& S^{-1}_{i,j} C^{-1}_{i,j} \Lambda^{+}_{i,j} C_{i,j} S_{i,j} U_{i,j} + S^{-1}_{i+1,j} C^{-1}_{i+1,j} \Lambda^{-}_{i+1,j} C_{i+1,j} S_{i+1,j} U_{i+1,j}
\end{aligned}
\tag{4.48}
$$

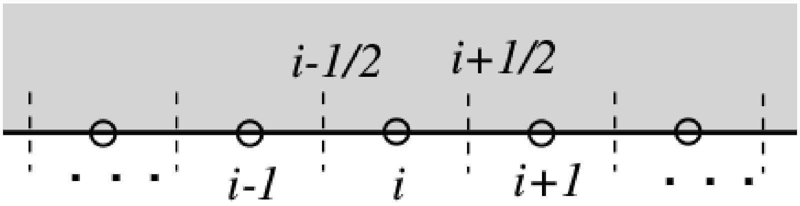

FIGURE 4.1: Discretization of the domain using cell centers (shown as circle) and cell interfaces (shown as a dotted line).

Using the same method as described above, the flux in y-direction $G_{i+1/2}$ can be expressed as given below,

$$
G_{i+1/2} = S^{-1}_{i,j} C^{-1}_{i,j} \Lambda^{+}_{i,j} C_{i,j} S_{i,j} U_{i,j} + S^{-1}_{i,j+1} C^{-1}_{i,j+1} \Lambda^{-}_{i,j+1} C_{i,j+1} S_{i,j+1} U_{i,j+1}
\tag{4.49}
$$

The fluxes in x and y-direction are computed and updated in the Eq. 4.36 to get the final solution.

Viscous and Turbulent Source Terms

The viscous terms which dominate the boundary layer dynamics are elliptic and hence are easier to solve as compared to the convective fluxes. The viscous fluxes are solved using the second-order central difference method [63], [64]. The source terms in $k-\varepsilon$ turbulence model are solved using the second-order central difference scheme and updated to the solution just as the viscous diffusion terms.

4.5 Boundary conditions

Instead of applying the boundary conditions directly on finite volume cells, a ghost cell methodology is used wherein a dummy/ghost/imaginary cell is created on the outer side of all the edges, and the boundary conditions are applied to these ghost cells. The remaining inner cells are called computational cells as no computations are done at ghost cells. The boundary conditions are applied to ghost cells in such a way that the flux at the interface between the ghost cells and inner cells corresponds to actual physical boundary condition. The number of points in stream-wise direction is nx and that in wall-normal direction is

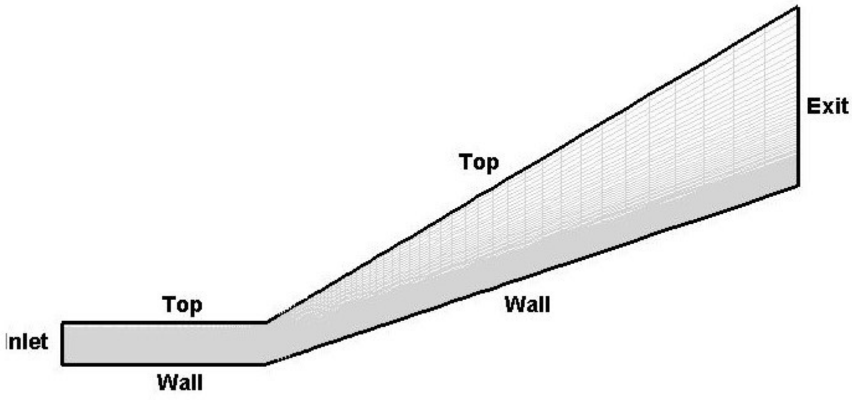

FIGURE 4.2: Boundary conditions applied to inlet, exit/outlet, top and wall at bottom of the computational domain.

ny. The grid lines in stream-wise direction (parallel to flow) is designated as j which varies from j = 1 at wall to j = ny at top. The grid lines along the wall-normal direction (perpendicular to flow) is designated as i which varies from i = 1 at inlet to i = nx exit. The free-stream conditions at the inlet is given at i = 1 with j varying from 1 to ny as given below

$$\begin{aligned} \rho(1,j) = \rho_\infty; \quad u(1,j) = U_\infty \\ v(1,j) = 0; \quad T(1,j) = T_\infty \end{aligned} \tag{4.50}$$

A supersonic extrapolation condition is applied to the outlet or exit of the domain. The flow-variables at exit at i = nx is computed using the conditions at location i = nx-1 as given below,

$$\begin{aligned} \rho(nx,j) = \rho(nx-1,j); \quad u(nx,j) = u(nx-1,j) \\ v(nx,j) = v(nx-1,j); \quad T(nx,j) = T(nx-1,j) \end{aligned} \tag{4.51}$$

At wall, where i varies from 1 to nx and j = 1 throughout, the physical boundary condition for viscous flows is applied. A no-slip condition is applied whereby the velocities at wall become zero. A zero pressure gradient is enforced simply by setting the ghost cell pressure equal to the nearest computational cell pressure. For isothermal wall conditions, a constant temperature is imposed on the wall (T_w = constant).

$$
\begin{aligned}
u(i,1) &= -u(i,2) \\
v(i,1) &= -v(i,2)
\end{aligned}
\tag{4.52}
$$

$$
\rho(i,1) = \rho(i,2)\frac{T(i,2)}{T(i,1)}; \tag{4.53}
$$

At the top boundary (see Fig. 4.2), free-stream conditions are assigned at j = my with i varying from 1 to mx as given below

$$
\begin{aligned}
\rho(i,my) = \rho_\infty; \quad u(i,my) = u_\infty \\
v(i,my) = 0; \quad T(i,my) = T_\infty
\end{aligned}
\tag{4.54}
$$

The initial condition for turbulent variables k and ε are computed using relations given by [57]

$$
k = \frac{3}{2}(u_{avg}I)^2 \tag{4.55}
$$

$$
\varepsilon = c_\mu \frac{\rho k^2}{\mu Re_t} \tag{4.56}
$$

where I = u'/u is the turbulence intensity, u_{avg} is average velocity at inlet and Re_t is viscosity ratio.

4.6 Summary

In this chapter, the governing equations and the numerical methodology used for the simulations is discussed in detail. The Reynolds averaging of the basic governing equations introduces an uknown Reynolds stress term. The Reynolds stress is modeled using Boussinesq's appromiation for closure. The equations for the k-ε turbulence model is discussed. The finite volume formulation of the equations is discussed, where the convective terms are solved using Steger-Warming method and the viscous terms are solved using the central difference method. Finally, the boundary conditions used for the 2D simulations is discussed.

Chapter 5

Amplification of turbulence across eddy-viscous shock waves

5.1 Introduction

In aerospace applications involving supersonic flow, the shock wave affects the turbulence in the supersonic boundary layer which in turn affects the surface properties of the vehicle. Consider a supersonic flow over a compression corner geometry, as shown in Fig. 5.1, the turbulence in incoming flow interacts with the oblique shock wave and affects the distribution of various properties across the surface of geometry. The complexity of this problem makes the analysis difficult. However, the problem of the turbulence interacting with normal shock wave is a similar problem, rich in physics and does not involve complexities due to boundary layer, shear-layer or flow separation at wall. By considering the normal components of flow over oblique shock, a normal shock is obtained as seen in

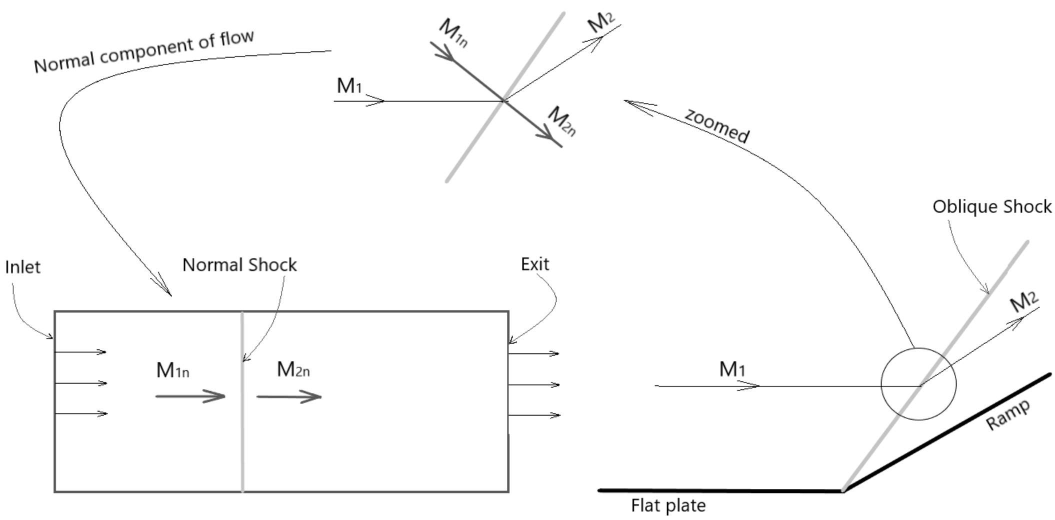

FIGURE 5.1: Flow over a normal shock obtained by taking the normal components of flow over a oblique shock.

left figure of Fig. 5.1. A standing normal shock is located inside the domain. The flow before the normal shock (at inlet) is supersonic and at the downstream of shock (at exit) it is subsonic. The turbulence in the incoming flow interacts with the normal shock and gets amplified across it. This problem of turbulence interacting with normal shock wave is frequently studied in literature for model improvement which leads to better predictions.

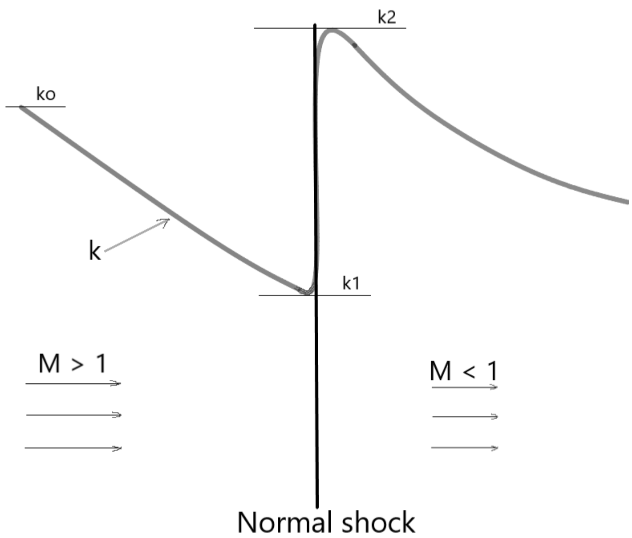

FIGURE 5.2: Schematic of evolution of turbulent kinetic energy k across a normal shock.

A homogeneous isotropic decaying turbulence interacting with the normal shock is considered as the model problem in the present analysis, as shown in Fig. 5.2. The decaying turbulent kinetic energy interacts with the normal shock, and gets amplified across the shock. The mean flow is one dimensional along the x-axis. The properties just upstream of the shock are denoted by subscript 1 and that immediately downstream of the shock are denoted by subscript 2. The conditions at the inlet of the domain is denoted by subscript 0, as shown in Fig. 5.2. Validation of results is done with DNS simulation data of Larsson et al. [12]. Effect of diffusion terms is also studied at turbulent boundary layer conditions in supersonic flow over a plate.

The methodology is discussed in section 5.2. Section 5.3 shows the results obtained by the solving non-conservative form of the equations. The results obtained by solving the conservative form of k-ε turbulence model are discussed in section 5.4. The conservative formulation is extended to flows with finite Reynolds number by including the diffusion terms and its effect is studied in section 5.5. The analysis of diffusion terms and the results, obtained using the realistic values of turbulent boundary layer data, are discussed in section 5.6.

5.2 Methodology

The k-ε turbulence model equations, when applied to 1D flow involving turbulence interacting with normal shock, reduces to

$$\frac{\partial \rho k}{\partial t} + \frac{\partial}{\partial x}(\rho u k) = -\frac{2}{3} C_0 \rho k \frac{\partial u}{\partial x} - \rho \varepsilon + \frac{\partial}{\partial x}\left[\frac{4}{3}\left(\mu + \frac{\mu_t}{\sigma_k}\right)\frac{\partial k}{\partial x}\right] \tag{5.1}$$

$$\frac{\partial \rho \varepsilon}{\partial t} + \frac{\partial}{\partial x}(\rho u \varepsilon) = -\frac{2}{3} C_1 \rho \varepsilon \frac{\partial u}{\partial x} C_{\varepsilon 1} - \frac{\rho \varepsilon^2}{k} C_{\varepsilon 2} + \frac{\partial}{\partial x}\left[\frac{4}{3}\left(\mu + \frac{\mu_t}{\sigma_\varepsilon}\right)\frac{\partial \varepsilon}{\partial x}\right] \tag{5.2}$$

The first term on RHS is the production term, second term is the dissipation term and the third term is the diffusion term, for both the equations. The second term in LHS is the convective term whereas the first one is the temporal term. The convective terms were solved using the Lax-Friedrichs numerical method, which is a FTCS (Forward in Time, Centered in Space) scheme. The Lax-Friedrichs method used to compute the convective flux is given by [65],

$$U_i^{n+1} = U_i^n + \frac{\Delta t}{2\Delta x}(f_{i+1/2}^n - f_{i-1/2}^n) \tag{5.3}$$

$$f_{i+1/2}^n = \frac{1}{2}((U_i^n) + U_{i+1}^n) + \alpha\lambda\,[U_{i+1}^n - U_i^n] \tag{5.4}$$

where α is the parameter that controls the value of numerical viscosity and λ is the wave speed. The schematic in Fig. 5.3 shows the cell centers (denoted by circles) located at *i-1, i, and i+1* whereas the cell faces (denoted by vertical dash line) are designated as i-$\frac{1}{2}$ and i+$\frac{1}{2}$ for the grid used in present simulations. The fluxes are computed along the cell faces using the Eq. 5.4 whereas the final solution is updated at the cell centers using the flux values of the respective cell faces, as given in Eq. 5.3. This method is first order accurate. The viscous diffusion terms and the turbulent source terms were solved using the second order second central difference method.

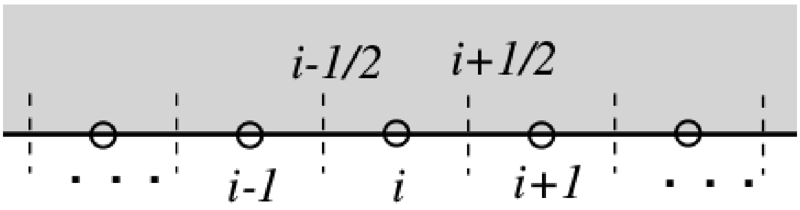

FIGURE 5.3: Schematic of cell-centers and cell-faces at the 1D grid used in RANS simulations.

An analytical solution is developed for the validation of the amplification of turbulent variables k and ε across the normal shock. Since the amplification in k and ε across the shock is dependent only on the production term, the dissipation and diffusion terms in the Eq. 5.1 and 5.2 can be neglected. Assuming it to be a steady state problem, the temporal terms on LHS can be neglected, and integrated in space across the shock (taking 1 as upstream and 2 as downstream of normal shock) to get the relation as given below [66]:

$$\frac{k_2}{k_1} = \left(\frac{\rho_2}{\rho_1}\right)^{\frac{2}{3}C_0} \quad and \quad \frac{\varepsilon_2}{\varepsilon_1} = \left(\frac{\rho_2}{\rho_1}\right)^{\frac{2}{3}C_1} \tag{5.5}$$

From the Eq. 5.5, amplifications in turbulent quantities across the shock can be found for a range of mach numbers and is used for the validation of results.

In the present analysis, the computational domain is in x-direction only and domain range is [-8, 42] with normal-shock being located at X = 0 location. For the simulations performed, the Mach number at the inlet ranges from 1.5 to 4.7 for all the simulations. In order to study the effect of grid refinement, the computational domain is discretized into 200, 400, 800 and 1200 points. The grid convergence is discussed along with results in subsequent sections. The free-stream conditions are applied at the inlet of the domain whereas at the exit of domain, an extrapolation boundary conditions are applied. The initial condition used for turbulent variables k and ε are calculated using the relations given in section 3.5.

TABLE 5.1: Details of DNS data corresponding to various Mach number used in validation [12].

M	M_t	Re_λ	Re_L	DNS source
1.5	0.22	40	5.56×10^2	Larsson & Lele [12]
2.0	0.22	40	7.48×10^2	
2.5	0.22	40	9.35×10^2	Larsson & Lele [12]
3.0	0.22	40	1.12×10^3	Larsson & Lele [12]
3.5	0.22	40	1.31×10^3	
4.25	0.22	40	1.59×10^3	Larsson & Lele[12]
4.7	0.22	40	1.76×10^3	

5.3 Non-conservative formulation

The simulations were performed over a domain in x-direcion by solving the equations as discussed in section 5.2. The different flow conditions for simulations done is listed in Table 5.1. The conditions at immediate upstream of shock (denoted by subscript 1) are available from DNS data and using the decay relations the conditions at the inlet (denoted by subscript 0) of computational domain is computed for turbulent variables. Table 5.1 shows the values of various turbulence quantities upstream of the shock for the range of Mach number used in the simulations.

Fig. 5.4 shows the evolution of turbulent kinetic energy (TKE) and turbulent dissipation rate for two test cases with varying shock strengths. In all the cases the shock is located at X = 0 position. Both k and ε gets amplified across the shock and this amplification is due to the production term in k-ε turbulence model. After the shock, both k and

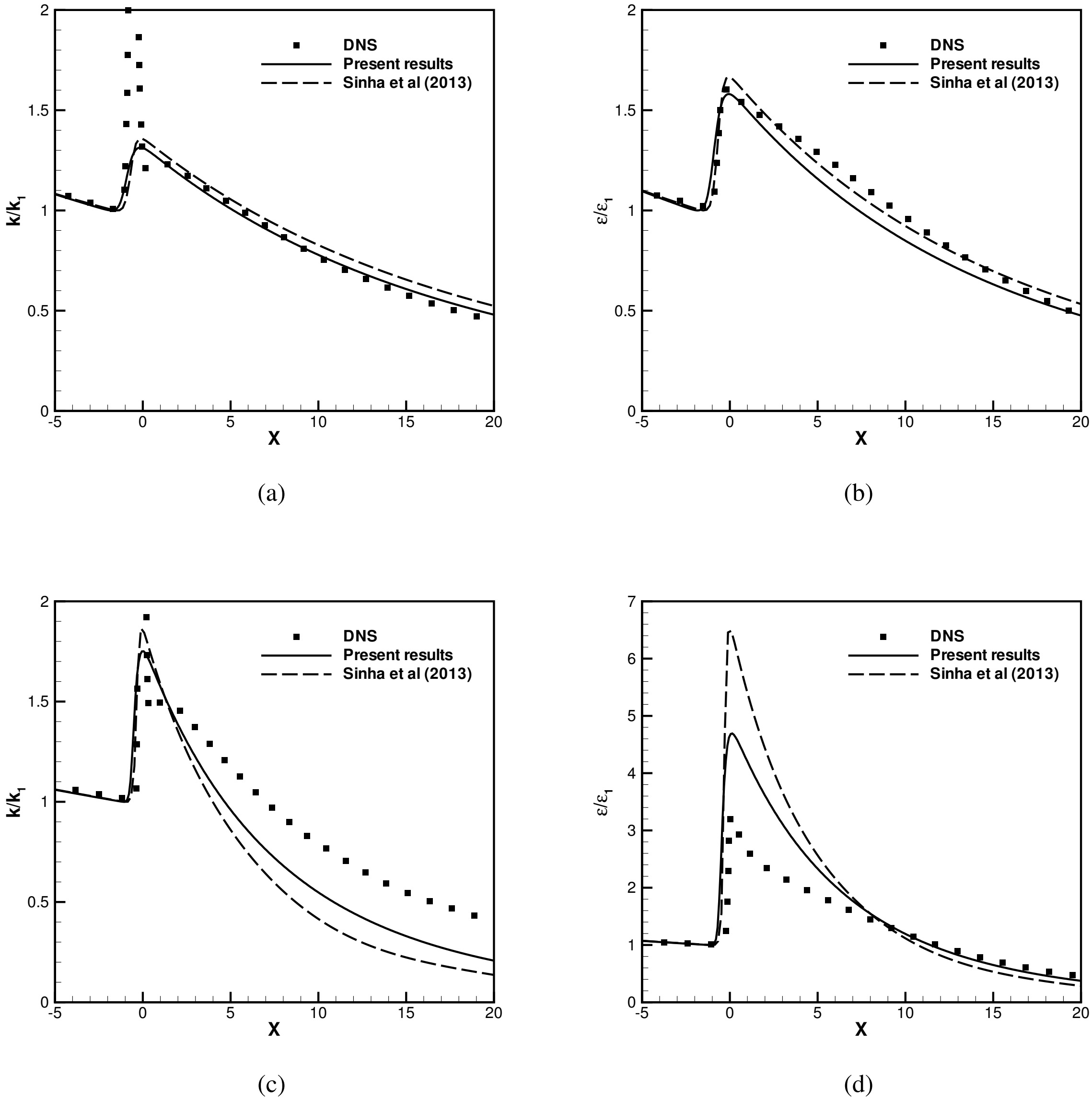

FIGURE 5.4: Evolution of turbulent variables k and ε across a normal shock (located at X = 0) for M = 1.5 (a, b) and M = 2.5 (c, d).

ε start decaying due to the dissipation term. It is seen that for low Mach number M = 1.5, the predictions are in good agreement with the DNS data. But for higher Mach numbers, the decay in k after shock is very sharp, contrary to DNS which shows a smooth decay. The results from Sinha et al [66] were obtained using Steger-Warming method with 200 grid points as baseline in their simulations whereas the present results were obtained using the Lax-Friedrich method using 400 grid points as the based in the simulations. The present results show a lower amplfication of turbulent variables as compared to the results of Sinha et al. (2013). This is because the Steger-Warming method is less dissipative as compared to the Lax-Friedrich method.

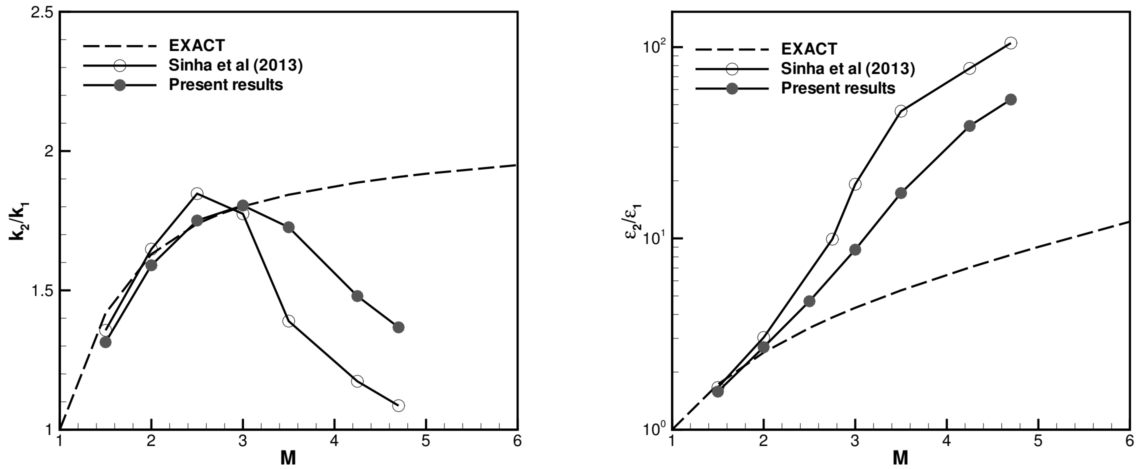

(a)

(b)

FIGURE 5.5: Amplifications in turbulent variables k and ε for a range of Mach numbers.

Fig. 5.5 shows the amplification (amplification of k and ε designated as k_2/k_1 and $\varepsilon_2/\varepsilon_1$ respectively) of turbulent variables against Mach number. Theoretically, as the Mach number is increased, the shock becomes stronger and hence the jump in k and ε should increase as indicated by analytical solution (Eq. 5.5) shown as dotted line. However, numerical predictions show that rather than increasing it decreases after a certain Mach number which correspond to strong-shock case (M $\geq$ 3). Whereas for ε it is seen that the jumps are highly over-predicted for increasing Mach numbers. The amplifictation of turbulent variables obtained from the results of Sinha et al. (2013) are higher than the presents results for most of the range.

Fig. 5.6 shows the effect of grid refinement on profile of k and ε for for M = 2.5 case. All the results shown so far used 400 (designated as 400) grid points in the simulations. In order to do the grid refinement study, further simulations were done with 200, 800

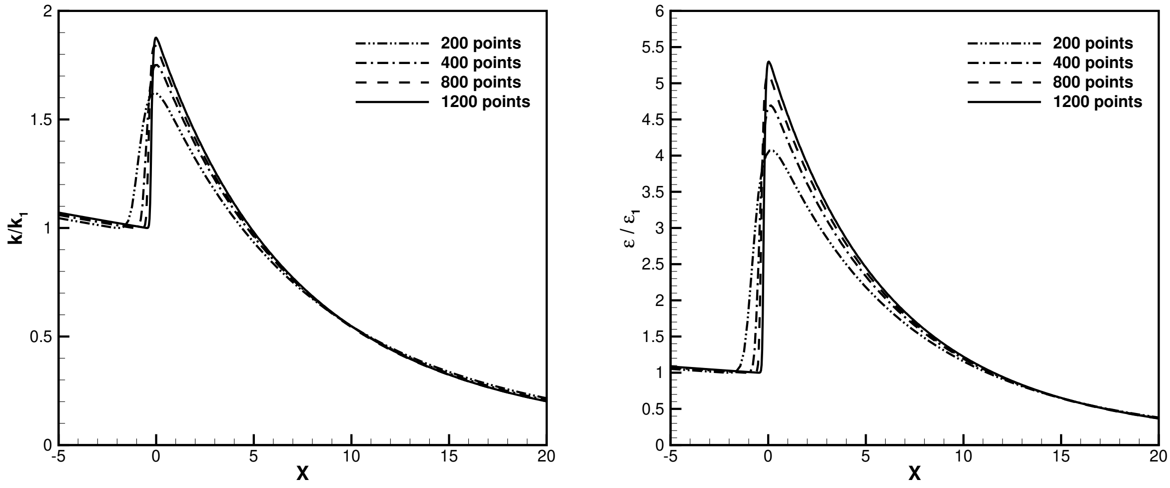

(a) (b)

FIGURE 5.6: Effect of grid refinement on evolution in turbulent variables k and ε for M = 2.5.

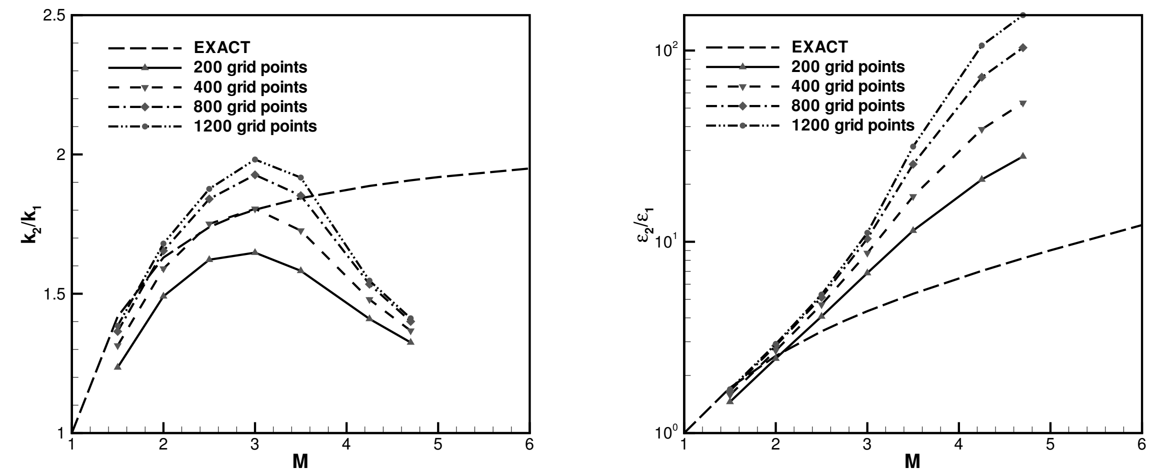

(a) (b)

FIGURE 5.7: Effect of grid refinement on amplification of turbulent variables k and ε across a normal shock for a range of Mach numbers.

and 1600 grid points designated as 200, 800 and 1600 respectively in the plots. It is seen from the plots that the peak values increase by a small margin at higher grids and downstream of the shock, the predicted decay are almost same for all the grids. Effect of grid refinement on amplification in turbulent variables is shown in Fig. 5.7 where the jump in k and ε over the shock for different Mach numbers, as predicted by different grid points, are compared with the analytical solution. The amplification ratio increases for weak and moderate shocks ($M \leq 3$) but for higher shock it starts to decrease. For high Mach numbers M = 4.7, the predictions for amplifications in k are coming close to each other whereas the predictions for ε amplifications are increasing with successive grid refinement. Simulations show this is due to the non-conservative error in the k and ε equations at the shock discontinuity for higher Mach numbers.

5.4 Conservative formulation

A conservative form of the turbulence model can be developed by analyzing the model equations at a shock-wave. Sinha and Balasridhar [66] studied the transport equations for the shock-unsteadiness k-ε model and arrived at a solution for k and ε at a normal shock in the limit of infinite Reynolds number. Following the methodology of Sinha and Balasridhar [66], the transformation of variables is carried out and conservative form of the equation is developed. Since $k \propto \rho^{\frac{2}{3}C_0}$ and $\varepsilon \propto \rho^{\frac{2}{3}C_1}$, two new variables are defined as following, which are conserved across a shock wave.

$$\begin{aligned} f &= k\rho^{-\frac{2}{3}C_0} \\ g &= \varepsilon\rho^{-\frac{2}{3}C_1} \end{aligned}$$

Using the above relation, the variables k and ε are replaced with variables f and g, and the new equation obtained [66], which is conservative, is as following.

$$\begin{aligned} \frac{\partial \rho f}{\partial t} + \frac{\partial}{\partial x}(\rho u f) = & -\rho g \rho^{\frac{2}{3}(C_1 - C_0)} \\ & + \rho^{-\frac{2}{3}C_0} \frac{\partial}{\partial x}\left[\frac{4}{3}\left(\mu + \frac{\mu_t}{\sigma_k}\right)\frac{\partial}{\partial x}(f\rho^{\frac{2}{3}C_0})\right] \end{aligned} \tag{5.6}$$

$$\begin{aligned} \frac{\partial \rho g}{\partial t} + \frac{\partial}{\partial x}(\rho u g) = & -C_2 \frac{\rho g^2}{f} \rho^{\frac{2}{3}(C_1 - C_0)} \\ & + \rho^{-\frac{2}{3}C_1} \frac{\partial}{\partial x}\left[\frac{4}{3}\left(\mu + \frac{\mu_t}{\sigma_\varepsilon}\right)\frac{\partial}{\partial x}(g\rho^{\frac{2}{3}C_1})\right] \end{aligned} \tag{5.7}$$

Here the second term on LHS contains both the convective and production term. The non-conservative production term is eliminated, but its physical effect is reproduced when f and g are recovered back to conventional turbulence variables k and ε. The first term on RHS is the dissipation term and the second one is the viscous term. The results presented in these section are obtained by solving the above equations of conservative form. The domain length, flow conditions and methodology remains same.

Fig. 5.8 shows the evolution of turbulent variables k and ε for two test cases with varying shock strengths. The results from Sinha et al [66] used 200 grid points as baseline in their simulations and the DNS data is from Larsson et al [12]. In all the cases the shock is located at X = 0 position. In the previous section it was seen that at high Mach numbers the prediction of the turbulent variables were not in good agreement with the DNS data. With the conservative formulation, the predictions in amplification as well in decay of the

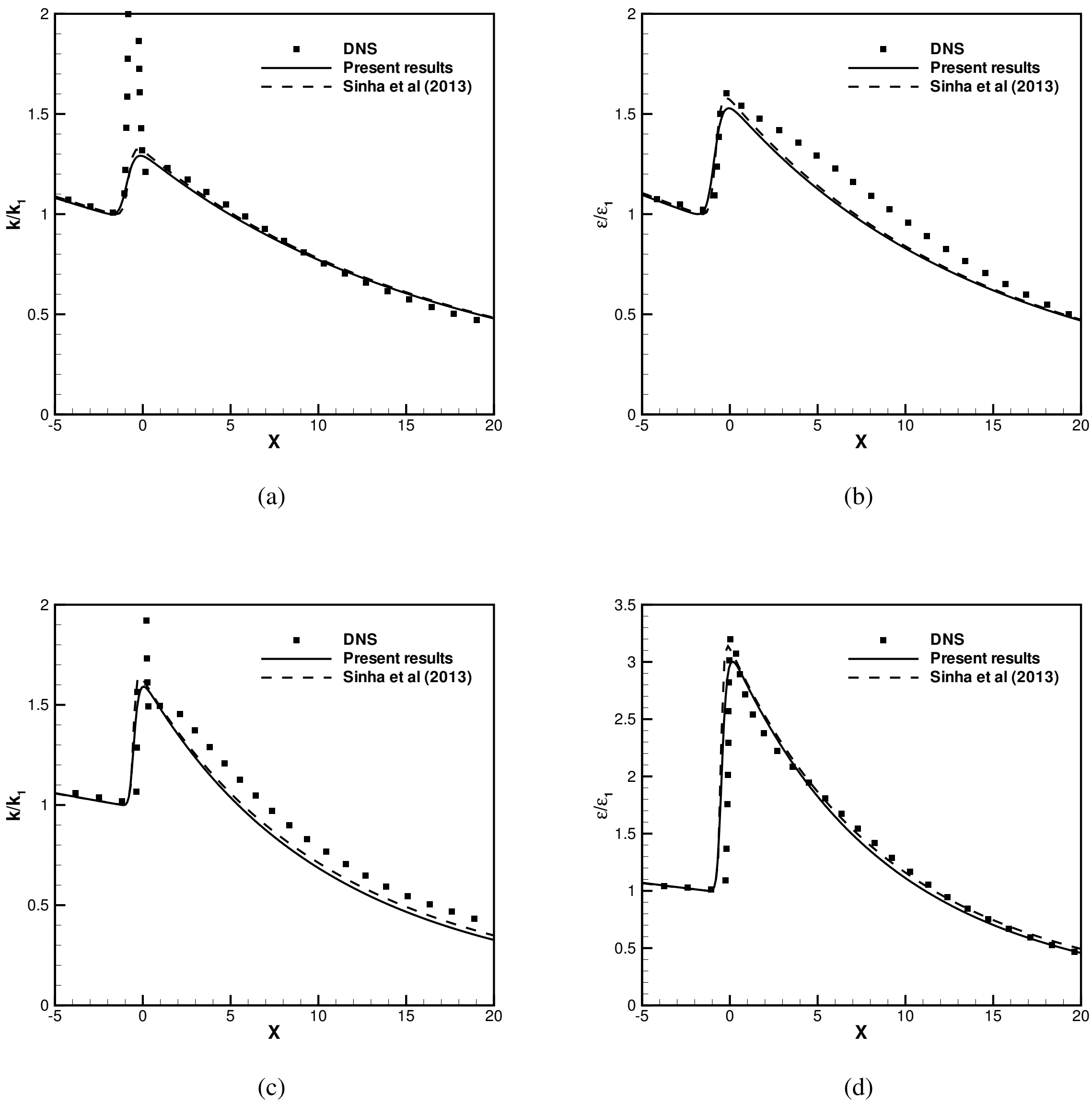

FIGURE 5.8: Evolution of k and ε across a normal shock for M = 1.5 (a, b) and M = 2.0 (c, d).

turbulent quantities are in good agreement with the DNS data. The conservative form of the equations does not contain the non-conservative production terms which are responsible for the numerical errors. By using the conservative form of the equation, numerical errors were reduced and dramatic improvement is seen in the solution.

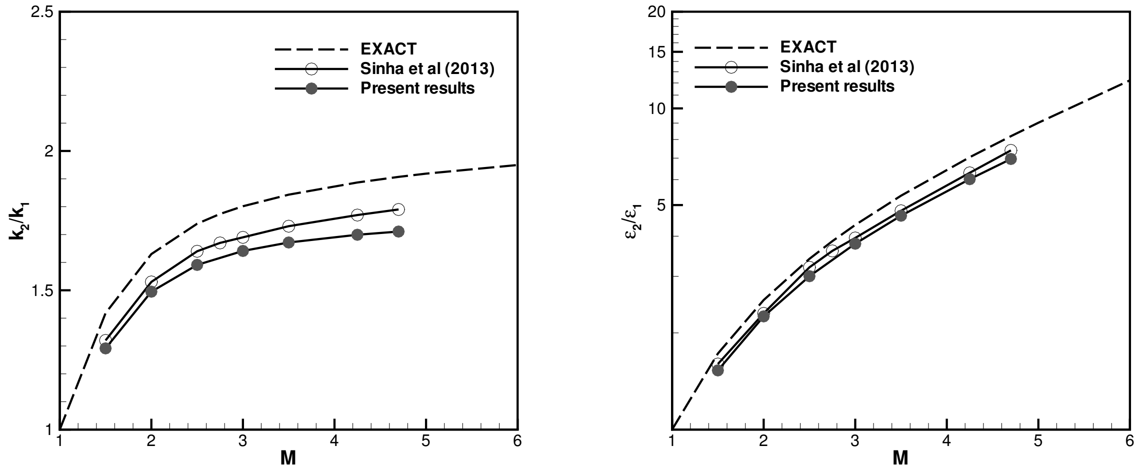

(a) (b)

FIGURE 5.9: Amplifications in turbulent quantities k and ε for a range of Mach numbers.

Fig. 5.9 shows the amplification of k and ε for a range of Mach number. With the non-conservative form of equation, as the Mach number is increased the amplifications in k and ε start to deviate at higher Mach numbers due to the numerical errors. With the conservative form of the equations these errors are removed and the amplifications in the turbulent quantities increase with the increasing Mach number following the analytical solution. Fig. 5.10 shows the effect of grid refinement on evolution of k and ε for M = 2.5 case. It is seen from the plots that the peak values increase by a small margin at higher grids and downstream of the shock, the predicted decay are almost same for all the grids. Fig. 5.11 shows that as the grid is refined, the predicted amplifications increase and move closer to the analytical solution. The conservative form obtained by the variable transformation minimized the numerical error at the shock wave without altering the physics of the problem. A dramatic improvement is observed in solution accuracy, especially for strong shock waves. The solution is found to be physically consistent and approaches the analytical result on successive grid refinement. The numerical predictions using the conservative k-ε turbulence model also matches well with DNS data over a range of Mach numbers.

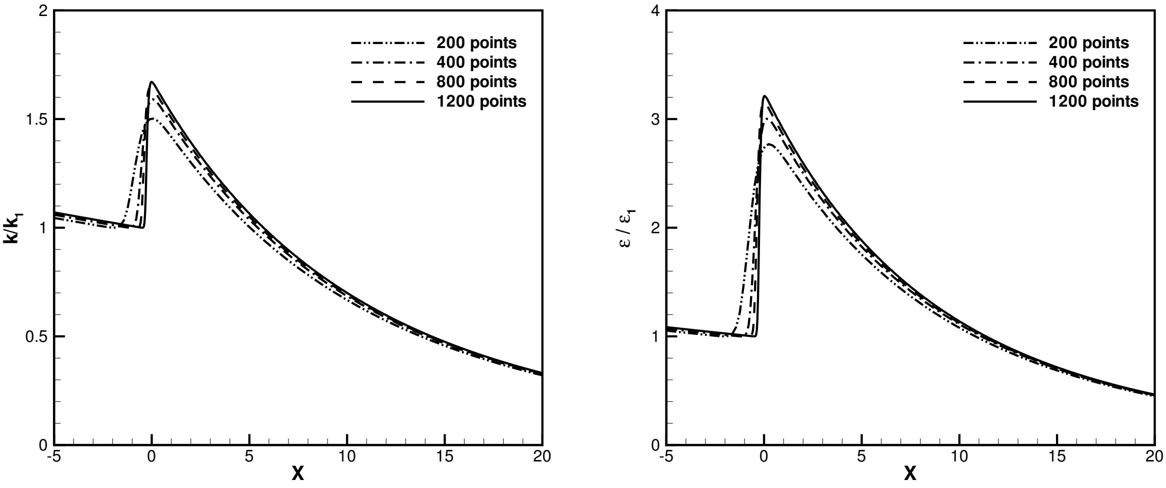

(a) (b)

FIGURE 5.10: Effect of grid refinement on evolution of k and ε across a normal shock.

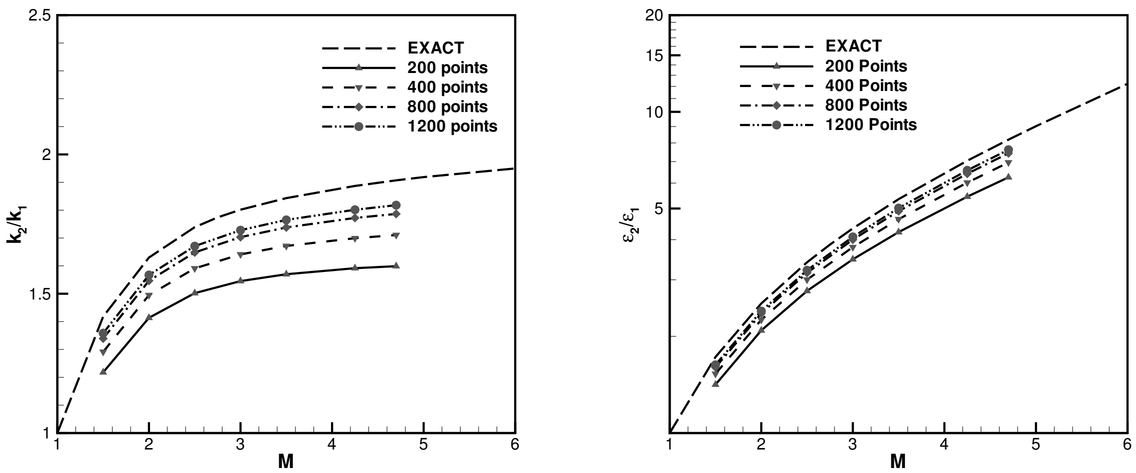

(a) (b)

FIGURE 5.11: Effect of grid refinement on amplifications in k and ε for a range of Mach numbers.

5.5 Effect of diffusion terms

Results in the previous sections were based on the Euler equations and the k-ε turbulence model without the viscous/diffusion terms. The effect of turbulent dissipation is retained, but the molecular and turbulent diffusion terms were not considered in the governing equations. Turbulent flows are highly dissipative, and turbulent or eddy viscosity is often much larger than the molecular viscosity of the fluid. The effect of turbulent viscosity therefore must be included if the conservative k-ε model is to be applied to realistic flows involving shock-boundary layer interactions. The diffusive effect of the turbulent viscosity is expected to smooth the shock gradients, resulting in a thicker shock wave. The production of turbulence is directly proportional to mean flow gradients, and therefore the amplification of k and ε are expected to be lower in an "eddy-viscous" shock wave. The shock-thickness of an eddy-viscous shock wave is determined by the eddy viscosity in a flow, instead of the numerical viscosity that is often applied to capture shock waves numerically.

Fig. 5.12 presents the evolution of TKE and turbulent dissipation rate, for Mach numbers 1.5 and 2.5, showing the effect of the diffusion term. The dotted line as indicated in the mentioned figure are for results obtained without the diffusion/viscous terms whereas solid lines are for results obtained by considering the diffusion terms. Here the peak of the k and ε is reduced a small amount, thereby showing the diffusive nature of the equations. The diffusion term is generally inactive before and after the shock. In the vicinity of shock, it takes some finite value which is responsible for smoothing of the sharp jumps in various quantities (ρ, u , p, T etc.) across the shock. This can be considered as thickening of the shock or as the diffusive effect on the shock. Similarly, in the k and ε equations, the diffusion term takes finite value in the region of shock and leads to the damping of the peak values of k and ε in the shock region. The effect of diffusion is due to the double derivative terms: $\partial^2 u/\partial x^2$ in the momentum and energy equation, $\partial^2 k/\partial x^2$ in k equation and $\partial^2 \varepsilon/\partial x^2$ in the ε equation. The differences are observed mainly in the region of shock. Away from the shock, the difference between results obtained with and without the diffusion term are negligible. Fig. 5.13 shows the ratio of turbulent quantities (amplification of k and ε designated as k_2/k_1 and $\varepsilon_2/\varepsilon_1$ respectively) against Mach number for simulations done with and without the diffusion terms. The results from Sinha et al. (2013) were for simulations done without the turbulent diffusion terms. The present results were obtained using the simulations done with and without the turbulent diffusion terms in the governing equations. As seen, the jumps for the viscous case (due to addition of diffusion terms) are always lower than the inviscid jumps. The addition of diffusion terms leads to smearing of shock and decrease in the amplification of turbulent quantities.

The effect of grid refinement on computed solutions using successively refined grids with 200, 400, 800 and 1200 equispaced points (cell sizes of 0.186, 0.093, 0.047 and 0.031 respectively) are shown in Fig. 5.14. As expected, a finer mesh gives a finer shock and higher jumps in k and ε across the shock wave; there is very little change in the solution

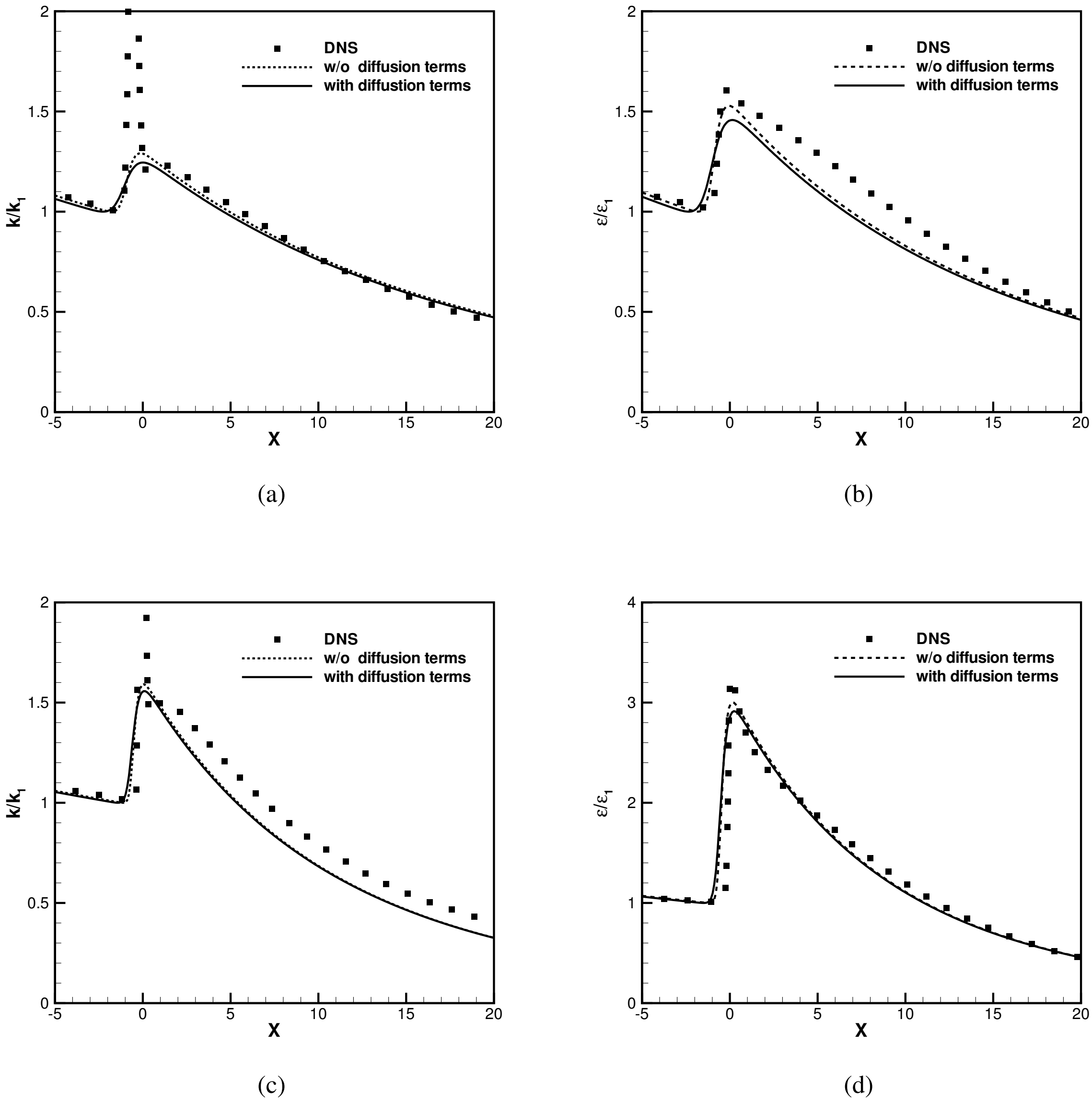

FIGURE 5.12: Effect of diffusion terms on k and ε profile across a normal shock for M = 1.5 (a, b) and M = 2.5 (c, d)

on either side of the shock. The results are also fairly close to the DNS data, except for the high TKE values obtained in the unsteady shock region, which represent shock oscillations [12]. Fig. 5.15 shows the jump in k and ε over the shock for different Mach numbers as predicted by different grid points and is compared with the exact solutions. As the grid is refined the amplifications in k and ε move closer to the exact solution.

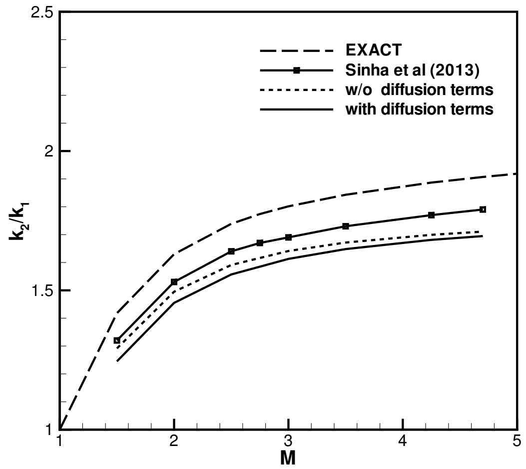

(a)

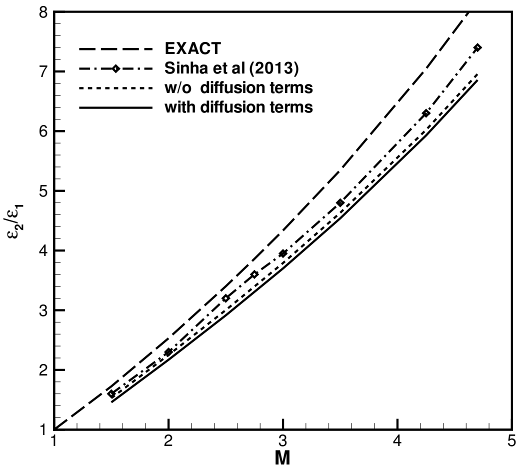

(b)

FIGURE 5.13: Effect of diffusion terms on k and ε amplification across a normal shock for different Mach numbers.

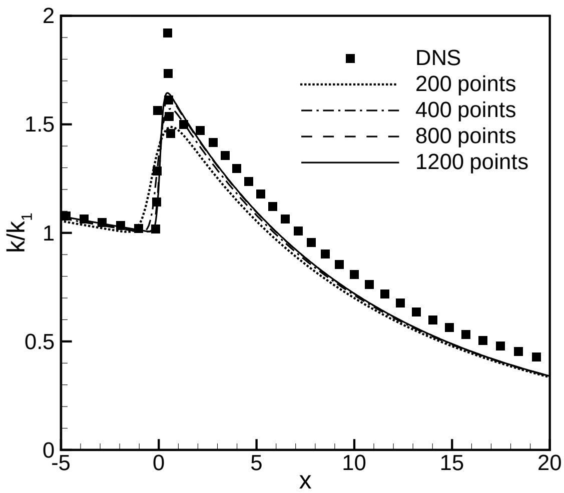

(a)

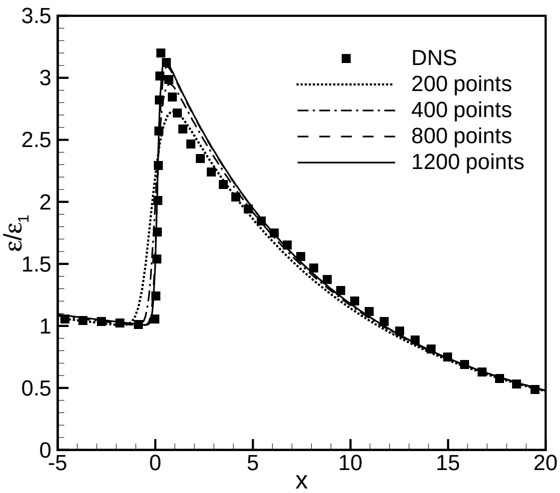

(b)

FIGURE 5.14: Effect of grid refinement on k and ε profile across a normal shock for M = 2.5.

5.6 Analysis of diffusion terms

In the previous section 5.5, the effect of diffusion term was studied using the flow conditions corresponding to DNS data [12], where the Reynolds number was very low. For any realistic flows in high speed applications, the Reynolds number is expected to be large. In

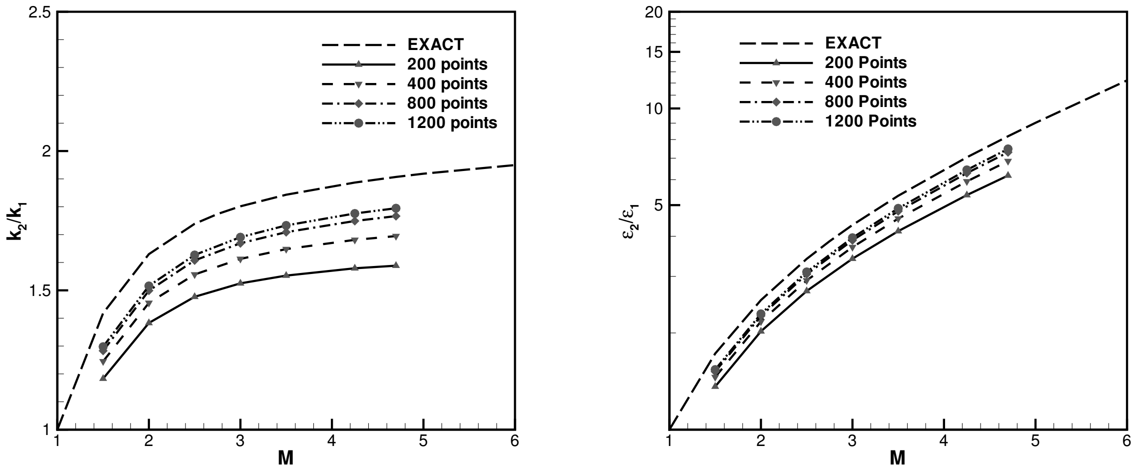

(a) (b)

FIGURE 5.15: Effect of grid refinement on k and ε amplifications across a normal shock at different Mach numbers for simulations done with the turbulent diffusion terms.

this section, the effect of turbulent diffusion terms on amplification in turbulent variables across a normal shock is studied using the boundary layer data of supersonic turbulent flow over a flat plate, where the Reynolds number is a representative of flight conditions.

The diffusion term in k equation is given as,

$$\frac{1}{Re}\frac{\partial}{\partial x}\left[\frac{4}{3}\left(\mu+\frac{\mu_t}{\sigma_k}\right)\frac{\partial k}{\partial x}\right] \tag{5.8}$$

Since the turbulence Reynolds number Re_t is the ratio of eddy-viscosity and molecular viscosity, the diffusion term can be written in terms of turbulence Reynolds number as given below,

$$\frac{1}{Re}\frac{\partial}{\partial x}\left[\frac{4}{3}\left(1+\frac{Re_t}{\sigma_k}\right)\mu\frac{\partial k}{\partial x}\right] \tag{5.9}$$

Based on the analysis of diffusion term (see appendix-E), the diffusion term is found to scale linearly with turbulence Reynolds number Re_t and inversely with Reynolds number Re and shock-thickness Δx.

For this study, a representative turbulent boundary layer on a flat plate is considered. The free-stream Mach number is taken as 2.84 corresponding to Settles 24° compression ramp experiment [48]. RANS solution is computed using a low Reynolds number k-ε turbulence model, and the numerical method is identical to that presented in [17]. Table 5.2 shows the peak values of turbulence Reynolds number Re_t inside the boundary

TABLE 5.2: Flow parameters from RANS solution of flat-plate boundary layer at different locations (in m) downstream of the plate tip.

M	M_t	Re	Re_t	Re_t/Re	location (x, m)
2.338	0.143	5.39E+04	1.89E+02	3.50E-03	0.15
2.384	0.129	1.64E+05	6.26E+02	3.81E-03	0.58
2.412	0.123	2.59E+05	1.03E+03	2.83E-03	1.03
2.421	0.120	3.52E+05	1.43E+03	4.06E-03	1.51
2.434	0.117	4.42E+05	1.82E+03	4.12E-03	2.02
2.437	0.116	5.35E+05	2.16E+03	4.04E-03	2.55

layer at different x-locations along the flat plate (see section 2.5 where variation of Re_t in the boundary layer is discussed in detail). The other parameters listed in Table 5.2 correspond to the location where the turbulence Reynolds numbers takes the peak value inside the boundary layer data. In the absence of peak-energy wave number for these cases, the boundary layer thickness is taken as the characteristic length scale, and the corresponding Reynolds numbers are included in the Table 5.2. These are used to set up equivalent canonical STI cases to isolate the effect of turbulent diffusion at realistic flow conditions. The different values of Re_t/Re, used in the results, are obtained by taking all the combinations of Re_t and Re values given in Table 5.2.

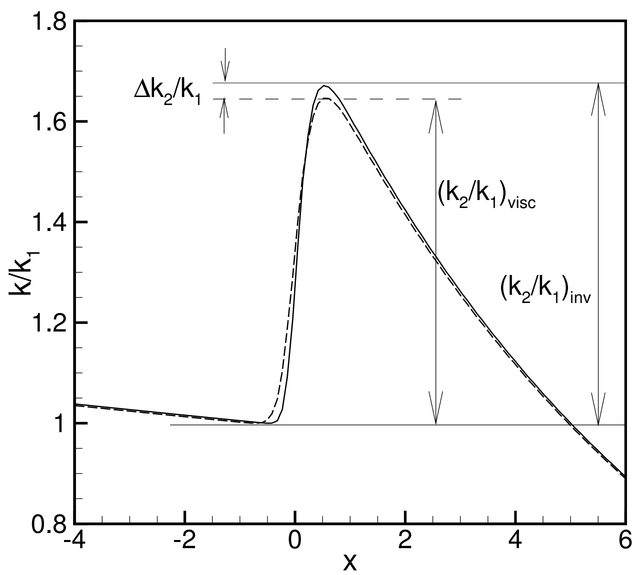

FIGURE 5.16: Difference in amplification in turbulent kinetic energy $\Delta k_2/k_1$ across shock showing the effect viscous/turbulent diffusion terms

Fig. 5.16 shows the evolution of normalized turbulent kinetic energy k for the simulations done with and without the turbulent diffusion terms using the flow-conditions of

DNS data corresponding to M = 2.5 flow. The difference in the amplification is thus given as $\Delta k_2/k_1 = (k_2/k_1)_{inv}$ - $(k_2/k_1)_{visc}$ as shown in Fig. 5.16. Using this parameter, the effect of turbulent diffusion terms will be quantified. The simulations are done using the supersonic boundary layer data (shown in Table 5.2) to study the effect of diffusion terms. Fig. 5.17 shows the effect of viscous/turbulent diffusion term for a range of Re_t/Re val-

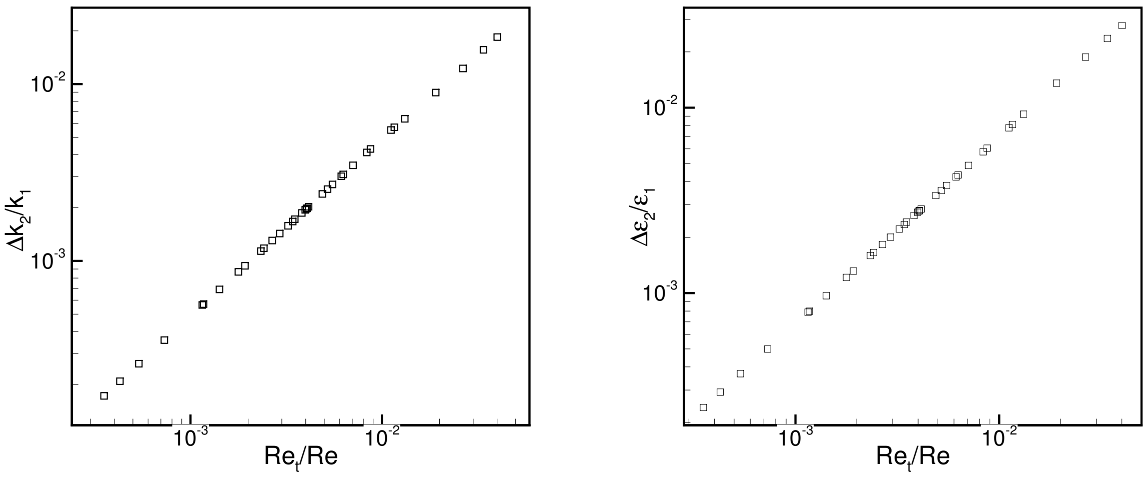

(a) (b)

FIGURE 5.17: Difference between inviscid and viscous amplifications of the turbulent variables k and ε for a range of Re_t/Re

ues. From the scaling of the diffusion, it is seen that the effect of diffusion term is directly proportional to turbulence Reynolds number Re_t and inversely proportional to Reynolds number. It is seen that as the ratio Re_t/Re increases, the difference in amplifications (between inviscid and viscous solution) increases. The effect of grid refinement on the peak k and ε are plotted as a function of Re_t/Re in Fig. 5.18. The data shows an identical trend with the finer grid results placed higher for all Reynolds numbers. The data shows a converging trend with grid refinement, especially for the turbulent dissipation rate. Thus a well-behaved solution is obtained in the limit of infinitely fine computational mesh, and the effect of diffusion terms in the k-ε equations found to be small.

5.7 Summary

A canonical case of isotropic turbulence passing through a normal shock is simulated using the k - ε turbulence model in order to understand the evolution of turbulent quantities k and ε across the normal shock and its decay downstream the shock. It is found that the non-conservative form of shock-unsteadiness k-ε turbulence model gives good prediction

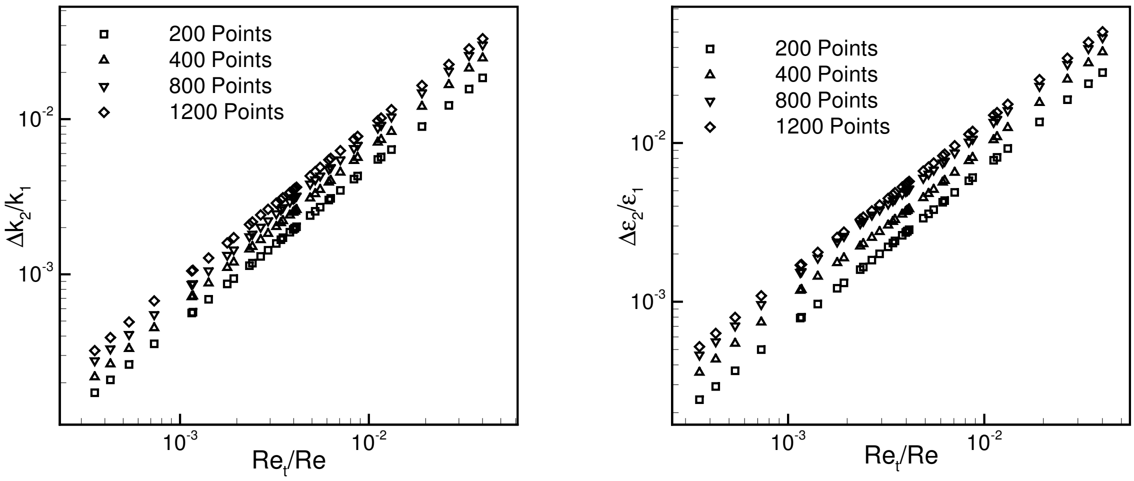

(a) (b)

FIGURE 5.18: Difference between inviscid and viscous amplifications of the turbulent variables k and ε for a range of Re_t/Re using different grid points.

for low Mach numbers but becomes highly inaccurate at higher Mach numbers. This is due to the non-conservative nature of the production term in the turbulence equations and is responsible for the error which becomes even higher at high Mach numbers and also when the grid is refined. Sinha et al. [66] proposed a new form of k-ε model where the equations are in conservative form. With this formulation the numerical errors are reduced to minimum and the results match well with the DNS as well as theoretical data. The analysis of the effect of viscous/turbulent diffusion term on eddy-viscous shocks is found to scale linearly the turbulent Reynolds number and inversely with the characteristic Reynolds number of the flow. Numerical simulations presented for a range of parameters substantiate the error estimate, and show that the effect of the diffusion terms is minimal for realistic values of Reynolds number. The difference remains bounded and small on successive grid refinement, and the model equations accurately reproduce DNS data of shock-turbulence interaction. The current k-ε model is thus shown to be numerically robust at shock waves with eddy-viscous effects.

Chapter 6

Physics of flow separation due to shock waves

6.1 Introduction

In this chapter, the effect of canonical parameters on flow separation in a compression corner geometry is studied. The shock-unsteadiness turbulence model, validated for realistic Reynolds numbers in the previous chapter, is used in the simulation. The compression corner consists of a flat plate parallel to the flow and a ramp inclined at angle with the incoming flow. The four canonical parameters studied are ramp angle, wall-temperature, Mach number and Reynolds number Re_δ. These parameters are varied such that its shows the effect of only one given parameter. For example, to study the effect of Mach number, only the Mach number is varied keeping all other parameters constant. The section 6.2 discusses the validation, grid convergence, and computational domain used in simulations performed. The effect of ramp angle on separation length is discussed in section 6.3. Section-6.4 shows the results obtained for different wall-to-recovery-temperature ratios and the analysis of the results. The result obtained with Mach number is discussed in section 6.5 along with the analysis and scaling of the separation length. Finally, the results obtained for different Reynolds number Re_δ are presented in section 6.6.

6.2 Methodology

Table 6.1 shows the flow conditions upstream of the corner for turbulent flow over the compression corner geometry. The values in second column correspond to on-design values (values at station-2 of scramjet geometry at on-design condition; see section 1.3 for details), and to study the effect of a given parameter, the values are varied as given in the last column of Table 6.1. The region near the corner is modeled as compression corner geometry, as shown in Fig. 6.1 (top). Simulations are done for a compression corner

TABLE 6.1: Range of flow parameters considered for compression corner simulations to study the effect of given parameter.

Parameters	Reference parameter	Range of parameters varied
θ	18.56	5, 10, 15, 20, 25
M	4.097	3.0, 3.5, 4.5, 5.0
Re_{δ}	1.1E+5	9.5E+4, 1.0E+5, 1.2E+5
T_w/T_r	0.24	0.12, 0.18, 0.29, 0.35

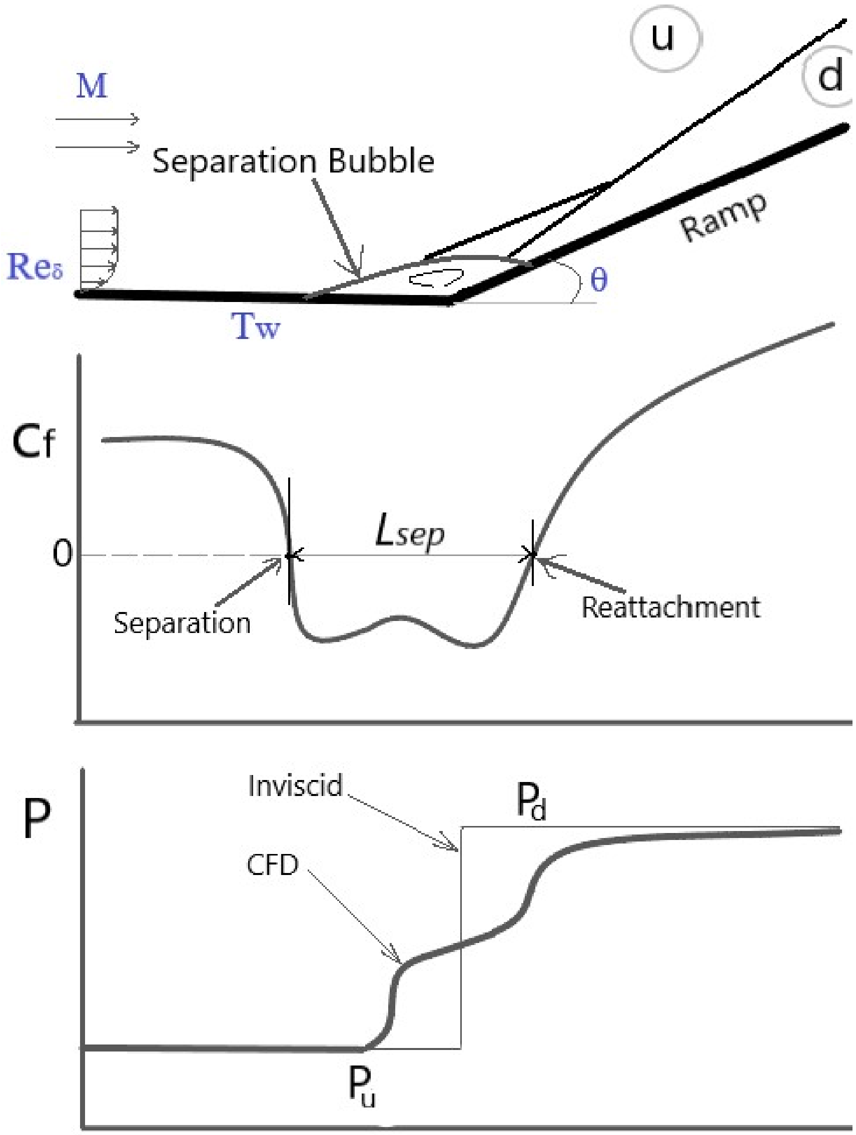

FIGURE 6.1: Skin-friction and wall-pressure distribution over the compression corner geometry.

geometry to study the effect of canonical parameter on separation length formed at the corner. The flat plate is 2.00 m long and the conditions at upstream of the corner are M =

4.097, P_u = 6.592 kPa, T_u = 426.55 K, and ρ_u = 0.05385 kg/m^3. To do the simulations, first, the flat plate is simulated using the above mentioned conditions, and the boundary layer profiles are extracted at the required location. The extracted boundary layer profile is given as an inlet to the computational domain to study the effect of the canonical parameters. To study the effect of canonical parameters, the range of given parameters considered are given the last column of Table 6.1. All the results presented in this chapter are based on the Table 6.1. The effect of separation bubble is seen in the wall-pressure (P) and skin-friction (C_f) distribution over the compression corner geometry. Fig. 6.1 shows the schematic of the skin-friction (middle) and wall-pressure (bottom) distribution over the compression corner geometry. The point where the skin-friction takes zero values indicates the separation and reattachment points and the distance between the two is taken as the separation length. Due to the shock formation, the upstream pressure P_u gets amplified to downstream pressure P_d. The CFD computed wall-pressure distribution deviates from the inviscid solution due to the formation of the separation bubble.

6.2.1 Computational domain

Fig. 6.2 shows the schematic of supersonic flow over a compression corner geometry and the computational domain used for the simulations. The computational domain consists of flat plate of 0.2m followed by the ramp of varying length (0.4, 0.5, 0.6 and 0.7m) inclined at an angle θ. The height of the domain at beginning is 0.04 m since the boundary layer thickness is less than 4 cm for all the cases considered and the height at the exit varies depending on the ramp angle and the shock angle. The corner is located $X = 0.2$ location. However, in presenting the results, the corner is shifter to $X = 0$ location so that the shock is at $X = 0$ location.

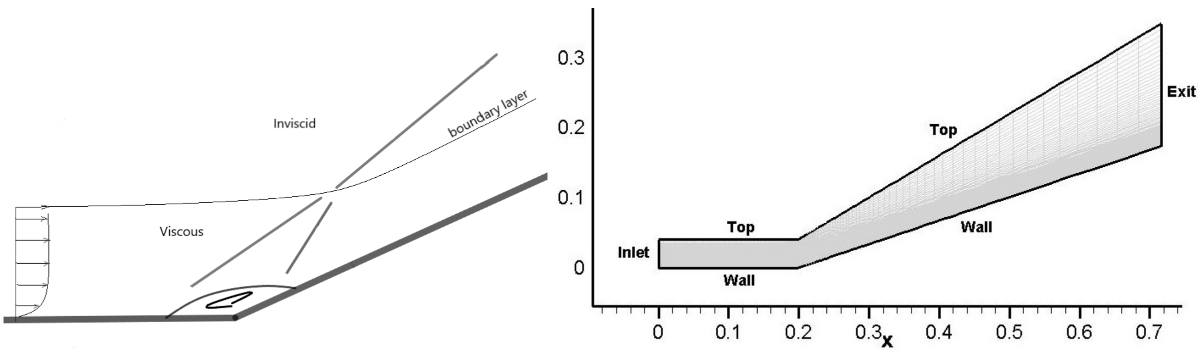

(a) (b)

FIGURE 6.2: Schematic of (a) supersonic flow over compression corner geometry and (b) computational domain with the grid.

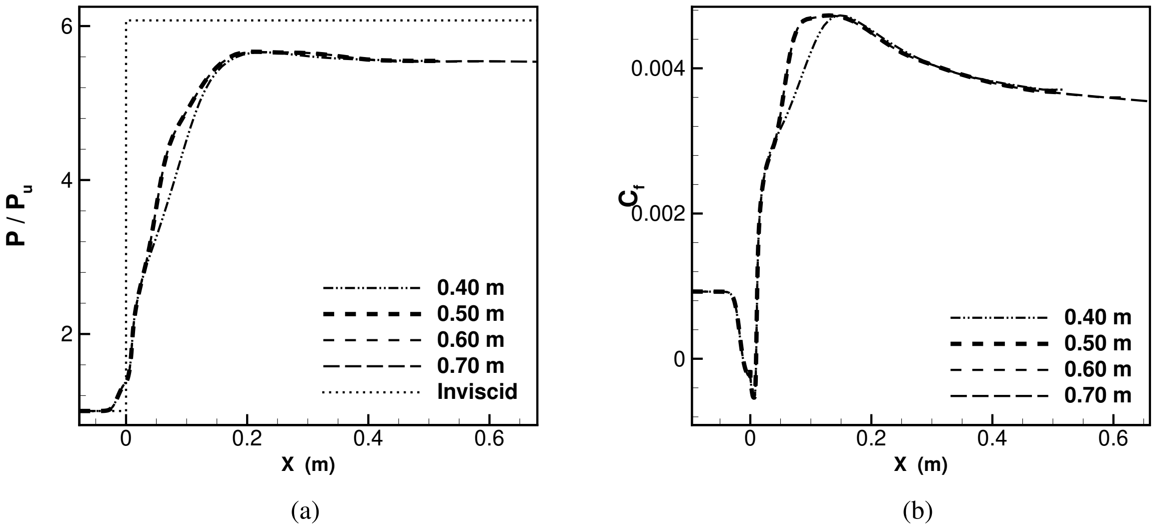

FIGURE 6.3: (a) Wall pressure and (b) skin-friction distribution for different ramp lengths. Corner shifted to $X = 0$ location.

The optimum value of the ramp length is found to be 0.5 m based on the results plotted in Fig. 6.3. The ramp length is varied from 0.4 to 0.7 in steps of 0.1 m. The separation bubble is found to be within the flat plate length of 0.2 m of the computational domain for all cases. Increasing the ramp length to values above 0.50 m does not much affect the results as seen from the wall-pressure and skin-friction distribution plots in Fig. 6.3.

6.2.2 Grid-convergence

For the grid convergence study, the number of points in stream-wise or wall-normal direction were halved/doubled, and the value of first cell thickness in stream-wise or wall-normal direction was doubled/halved, respectively, for M = 6 flow condition. In Fig. 6.4a and 6.4b, the number of grid points and the first cell thickness is varied in stream-wise direction, while that in Fig.6.4c and 6.4d same is varied in wall-normal direction. Only for the coarse grid cases, a slight difference is observed at the peak values of skin-friction while for all other cases, the difference is negligible. Based on the grid convergence study shown in Fig. 6.4, the number of grid points in stream-wise direction is taken to be 170 points with first cell thickness at the corner as 5e-5 m whereas that in wall-normal direction, the numberof grid points is 200 with the first cell thickness near wall as 5e-7 m. An exponential grid stretching is used where the grid is clustered near the wall and at the corner. The stretching factor β is computed using the relation $\beta = e^{\alpha}$. The value of α is

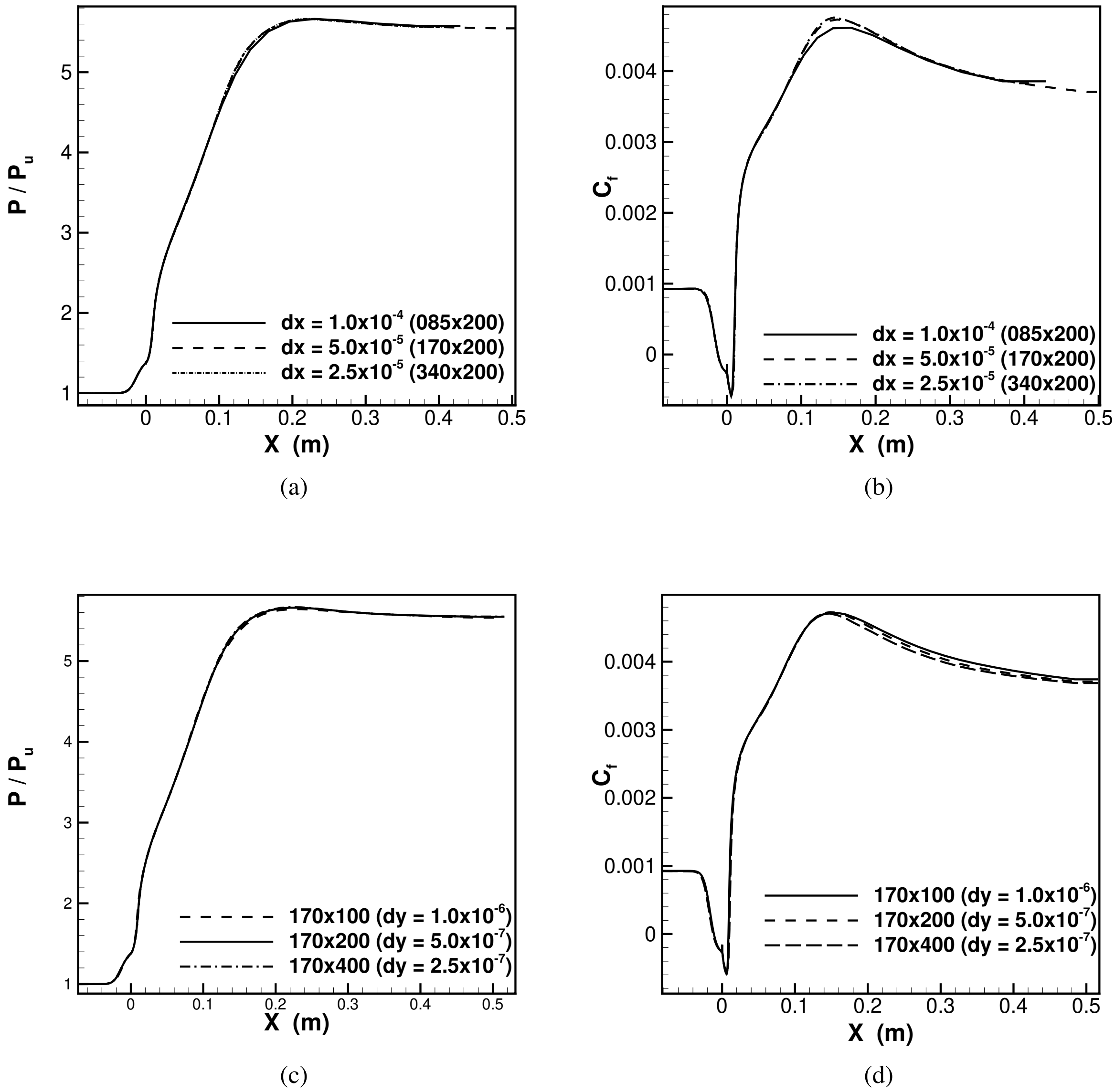

FIGURE 6.4: Wall-pressure and skin-friction distribution for different grids in stream-wise (a,b) direction and in wall-normal (c,d) direction.

computed based on the domain length, number of grid points and first grid thickness. The stretching factor was less than 1.07 for all the grids used in the simulations.

6.2.3 Validation

Validation is done using the (i) experimental data of Settles et al. [33] and (ii) scaling law of Souverein et al. [56]. Settles et al. [33] did experiment for supersonic flow over a compression ramp of different ramp angles. The free-stream conditions given in the experiments were $M_\infty = 2.83$, $P_\infty = 23.9$ kPa, $T_\infty = 103$°K and $\rho_\infty = 0.8096\ kg/m^3$. The ramp angles ranged from θ = 16, 20, 24°, and the incoming turbulent boundary layer thickness was about δ_0 = 2.3 cm for all the cases. The free-stream Reynolds number was Re = 7.3 x $10^7/m$.

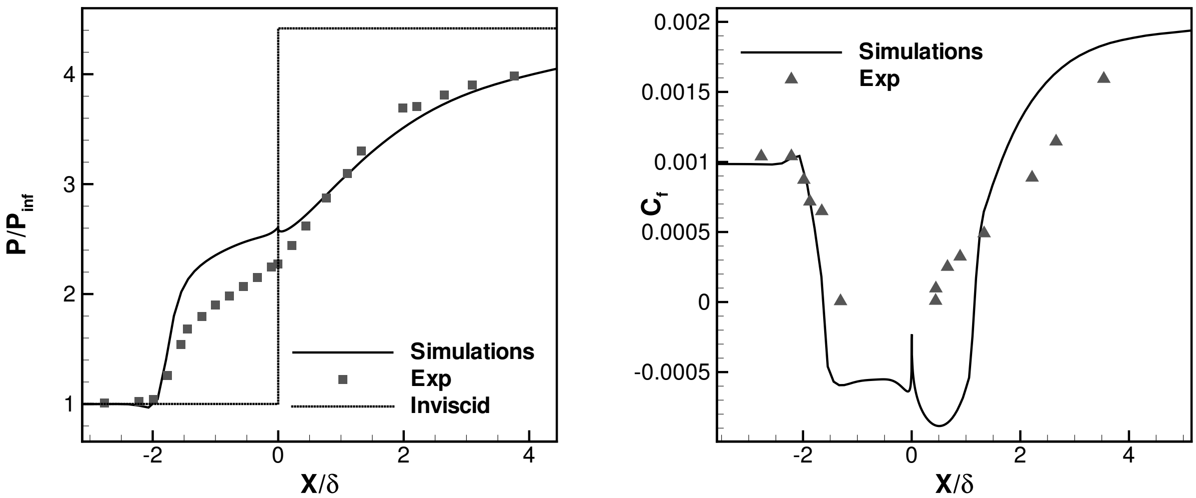

(a) (b)

FIGURE 6.5: Comparison of (a) computed wall-pressure and (b) skin-friction distribution with the experimental data of Settles et al. [48] for θ = 24 degree case.

Fig. 6.5 gives the comparison of computed results with experimental data of Settles et al. [24] for 24 ° ramp angle case, where strong interaction is seen, and separation length is largest as compared to all other cases. The stream-wise direction is normalized by incoming boundary layer thickness δ. The normalized pressure distribution is compared with experimental data as well as inviscid solution obtained using Rankine-Hugoniot relations. The first pressure rise (upstream influence) occurs at x/δ = -2 followed by a plateau for a small distance. The second pressure rise occurs at around x/δ = +1.10 and then it reaches close to inviscid values gradually. The plateau region (between the two pressure rises) indicates the region of flow separation. The skin-friction takes zero value at around x/δ = -1.5 and indicates the start of flow separation. At around x/δ = + 1.20, the skin-friction reaches back to zero value and at this point the separated flow reattaches indicating the end of flow separation. The distance between the separation and reattachment point is the separation length.

Fig. 6.6 shows the comparison of present results with results of Sinha et al. [17] for 16, 20 and 24° case of Settles et al. [33]. The upstream influence (first pressure rise due to separation shock) is observed at $x/\delta \simeq$ -2 location for the 24-degree case and it moves further downstream with a decrease in ramp angle as seen in Fig. 6.6a. The upstream

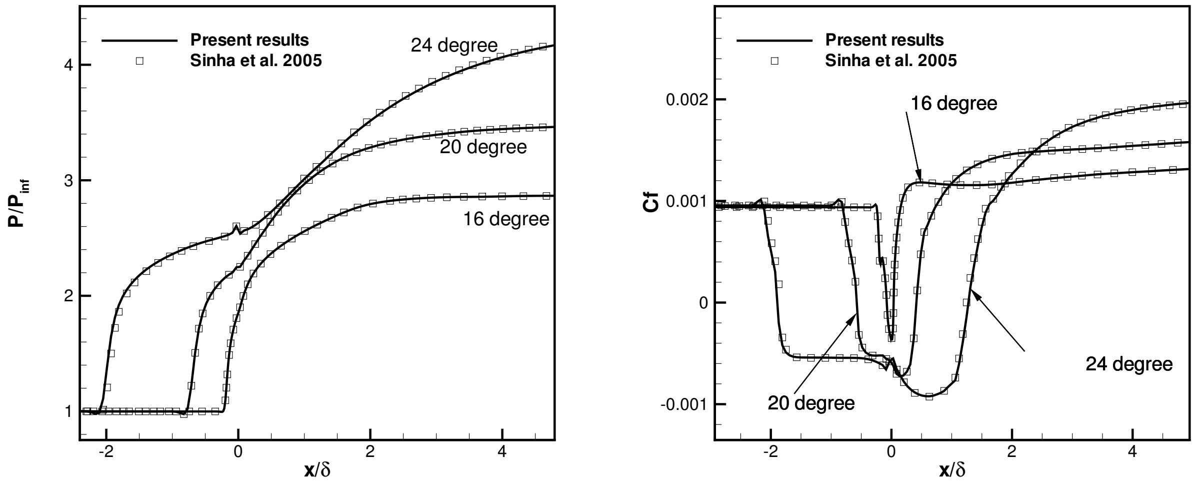

(a) (b)

FIGURE 6.6: Comparison of computed (a) wall-pressure and (b) skin-friction distribution with the computational results of Sinha et al. [17]

influence is followed by plateau (constant pressure in the re-circulation region) and then a second pressure rise, due to reattachment shock, is observed at downstream of the corner. The pressure jump increases with an increase in ramp angle due to the increase in shock-strength. Fig. 6.6b shows the comparison of computed skin-friction distribution for same ramp angle cases. The location ($x/\delta \simeq$ -2 for 24-degree case) where the value of skin-friction starts to fall indicates the upstream influence. The flow gets separated near $x/\delta \simeq$ -1.5 location for 24-degree case, where the skin-friction takes zero value, and this location is denoted as the separation point (S). The flow gets re-attached, at $x/\delta \simeq$ +1.25 for 24-degree case, where the skin-friction reaches back to zero from negative values, and this location is denoted as re-attachment point (R). It is seen that as the ramp angle decreases, the separation length decreases due to a decrease in shock-strength.

6.3 Effect of ramp angle

The effect of ramp angle on flow separation has been widely studied in the past both using experiments and computations. Consequently, this parameter acts as a starting point for most of separation length studies as even the scaling laws were formulated based on this parameter. In this section, the effect of ramp angle on flow separation for different ramp angles is studied, followed by a brief comparison with results observed in literature and analysis of present results. Simulations were done to study the effect of ramp angle on separation length by varying the ramp angle θ as 5, 10, 15, 18.56, 20 and 25° where the angle θ_2 = 18.56° corresponds to an on-design condition as given in Table 6.1. First, the flat plate simulated using the conditions given at the upstream of the corner, and boundary layer profile was extracted at the required location. This extracted boundary layer profile was used as an inlet for compression corner simulations with different ramp angles. The conditions at upstream of the corner are M = 4.097, P = 6.592 kPa, T = 426.55 K, and ρ = 0.05385 kg/m^3. The adiabatic wall temperature were used for all the simulations.

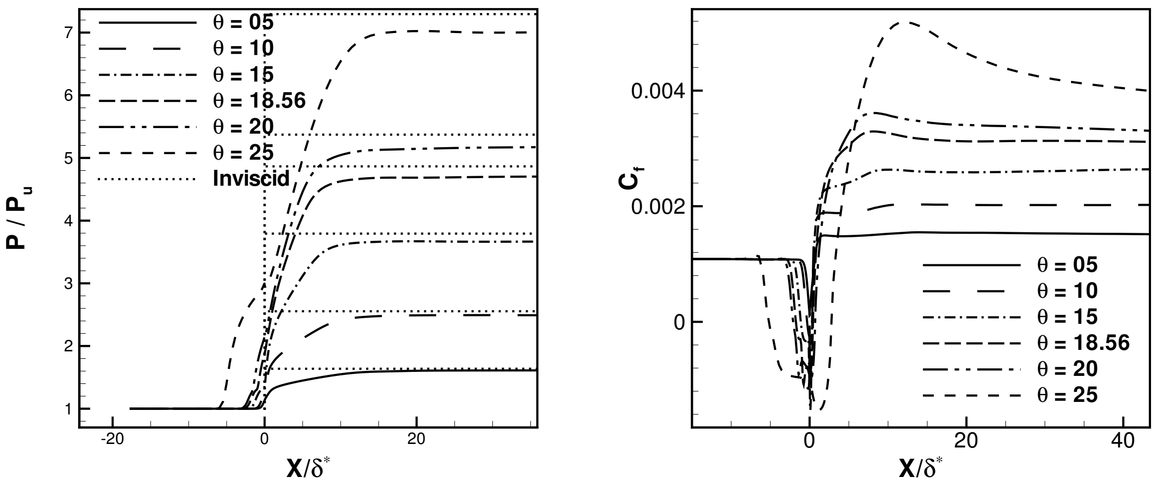

(a) (b)

FIGURE 6.7: Variation in (a) wall-pressure distribution, and (b) skin-friction distribution for different ramp angles.

From Fig. 6.7a shows the normalized pressure distribution over the surface compression corner geometry for different ramp angle θ. The pressure distribution (indicated as P) is normalized by the pressure upstream of the interaction (indicated as P_u). The stream-wise direction (x) is normalized the displacement boundary layer thickness of the boundary layer profile extracted from the flat plate simulations. The displacement boundary layer thickness of the extracted boundary layer profile was $\delta^\star$ = 0.01081 m for all the cases since only the ramp angle is varied. It is seen that as the ramp angle increases, pressure jump across the shock increases, which is consistent with the inviscid solution (shown as a dotted line) obtained from gas dynamics. For smaller ramp angles, the pressure jump obtained from the simulations nearly matches with the inviscid values. However, the simulations always under-predict the pressure jump by a small margin and this difference increases as the ramp angle increases. Further, as the ramp angle increases, the upstream influence (distance at which pressure starts to rise before the interaction) increases, which indicates increase in separation length. Fig. 6.7b shows the distribution of skin-friction for different ramp angles. As the ramp angle increases the size of the separation bubble increases. The point where the x-location takes zero skin-friction value is the separation point and indicates start of flow separation. The x-location where it comes back to zero value from negative values indicate the re-attachment point. The region between these two points (separation and re-attachment points) has reversed flow and separation length is taken as the distance between these two points.

The above observations are in consistency with experiments [48],[29], [31] as well as RANS [44][10] and DNS [67] computations. As the ramp angle increases, the difference between the computed pressure and inviscid pressure downstream of shock increases, computational predictions being lower than the inviscid values. The same pattern is observed in experiments of Elfstrom [29]. One probable reason for this might be - increase the velocity fluctuations near the wall as the ramp angle increases. Fig. 6.8 shows the variation of normalized separation length with the normalized shock strength for different ramp angles using Souverein et al. [56] scaling law and its best curve fit equation. The filled symbols are results obtained using present results, whereas the open symbols are simulations done with experimental conditions of Settles et al. [48]. The scaling law proposed by Souverin et al. [56] gives a good estimate of separation as most of the data is found to be scattered over the curve $y = ax^b$ where a = 1.3 and b = 3 are the constant in the best curve fit equation.

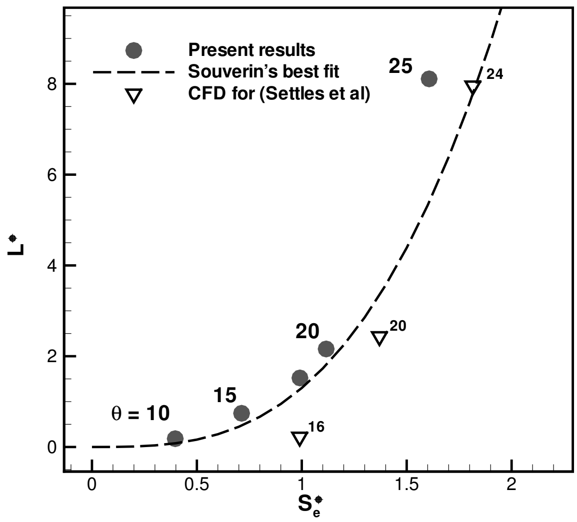

FIGURE 6.8: Normalized separation length obtained for ramp angles plotted against the normalized shock-strength using the scaling law proposed by Souverein et al [56], and its best curve fit equation.

TABLE 6.2: Pressure jump across the shock for different ramp angles.

M	θ	P_d/P_u
4.09	5.00	1.63
4.09	10.00	2.55
4.09	15.00	3.79
4.09	20.00	5.37
4.09	25.00	7.29

As, the ramp angle θ increases, the pressure jump P_d/P_u across the shock (P_d is pressure after shock and P_u is pressure before shock at upstream of corner) increases, and the separation length also increases. The reason being an increase in ramp angle leads to an increase in shock strength (higher shock angle) which increases the pressure jump across the shock, as seen in Table 6.2. Thus, the pressure jump across the shock is found to be an important scaling parameter for separation length studies, and this factor has been used in all the scaling or empirical relations available in the literature. However, this parameter has a limitation that it is not applicable when shock strength increases due to an increase in Mach number, keeping the ramp angle constant. This will be discussed in detail in the section 6.5 on Effect of Mach number.

6.4 Effect of wall temperature

Simulations are done to study the effect of wall temperature by varying the wall-temperature in the range of 200, 300, 400, 500 and 600 K which gives the ratio T_w/T_r as 0.12, 0.18, 0.24, 0.29 and 0.35, respectively. The methodology followed for simulations and the conditions at upstream of the corner are M = 4.097, P = 6.592 kPa, T = 426.55 K, and ρ = 0.05385 kg/m^3.

Fig. 6.9a gives a comparison of the pressure rise for different wall temperatures. The ratio T_w/T_r is obtained by varying the wall-temperature. The wall-pressure distribution (indicated as P) is normalized by the wall pressure upstream of the corner (indicated as P_u). The stream-wise direction (x) is normalized the displacement boundary layer thickness of the boundary layer profile extracted from the flat plate simulations. The displacement boundary layer thickness of extracted boundary layer profiles were 0.009318, 0.009320, 0.009364, 0.009441 and 0.09537 m for simulations done with wall-temperatures 200, 300, 400, 500 and 600 K, respectively. For the lowest T_w/T_r ratio, the pressure rises just upstream of the corner, which indicates the start of flow separation, and this pressure rise is sharp and distributed over a small region. As the T_w/T_r ratio increases, the pressure rise happens much upstream of the corner leading to increase in size of the separation bubble. The pressure rise at high T_w/T_r ratios is gradual, distributed over a

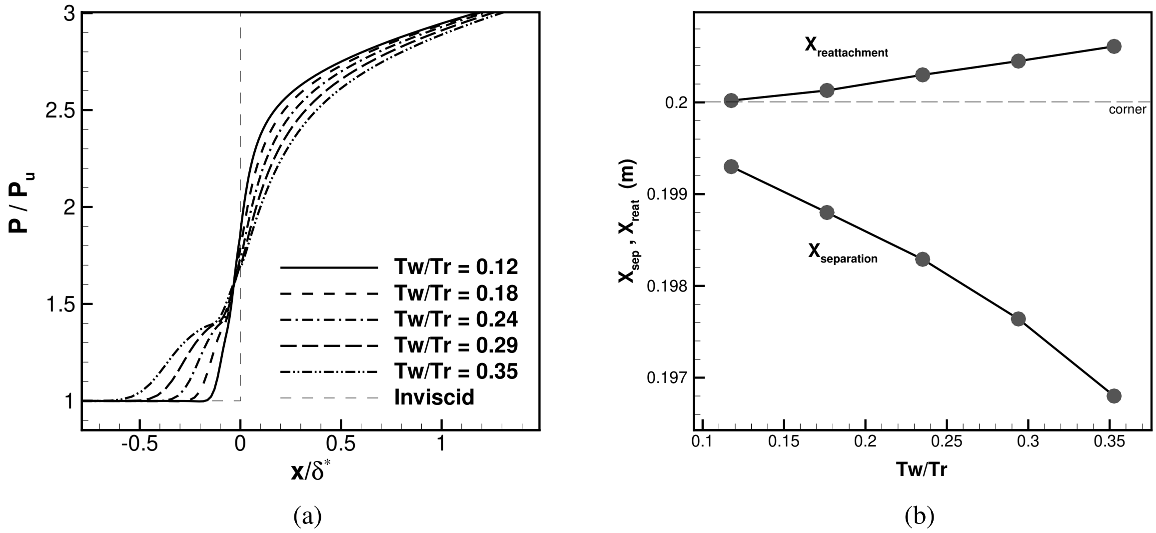

FIGURE 6.9: (a) Variation in wall-pressure distribution, and (b) movement of the separation and re-attachment points for different wall-to-recovery-temperature ratios.

region and not as sharp as in lower T_w/T_r cases. The dashed line indicates the inviscid solution, and is same for all the cases as the shock-strength is unaffected by changes in wall-temperature. As the wall-temperature increases, both separation and re-attachment points move away from the corner (as shown in Fig. 6.9b), and thus the separation length is found to increase.

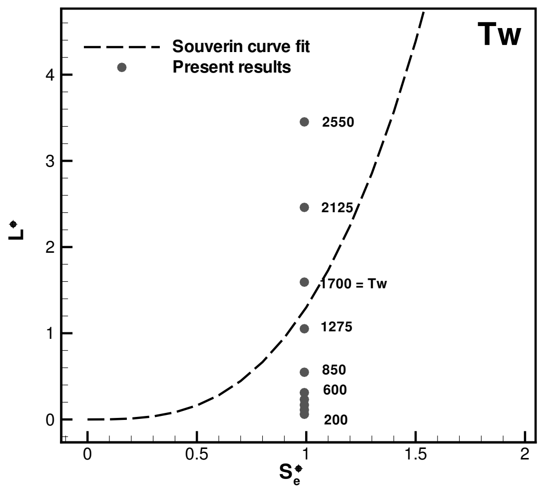

FIGURE 6.10: Normalized separation length obtained for different wall-temperatures plotted against the normalized shock-strength using the scaling law propsed by Souverein et al [56], and its best curve fit equation.

The observed trend in separation length changes with wall-to-recovery temperature ratios is in agreement with those available in the literature ([19],[44], [38], [35], [10]). Marini et al. [10] showed that the separation length shows a nearly linear growth with an increase in ratio T_w/T_r. Further, it was added that the ratio T_w/T_r is not a similitude parameter, i.e., for the same value of T_w/T_r realized with different couples of $(T_w, T\ )$ produces different separation lengths. Fig. 6.10 shows the variation of the normalized separation length with shock-strength for different wall temperatures ranging from 200 K to 2550 K. Since the scaling law proposed by Souverein et al. [56] does not take into account the effect of changes in wall-temperature, the normalized shock-strength is constant for all the cases whereas the normalized separation length increases with an increase in wall temperature. However, the adiabatic wall-temperature ($T_w = 1700$ K, where $\frac{T_w}{T_r} = 1$) is close to the best curve fit line proposed by Souverein et al. [56] as the scaling law proposed by Souverein et al [56] was developed using the adiabatic data available in the literature. Hence, for non-adiabatic cases, the prediction is bound to be offset (above for hot wall and below for cold walls) from the curve. For the cold wall-temperatures ($T_w < 1700$ K), the separation length predicted is always on the lower side of this curve whereas for the hot-wall cases ($T_w > 1700$ K), the separation length predicted is on the upper side of this curve.

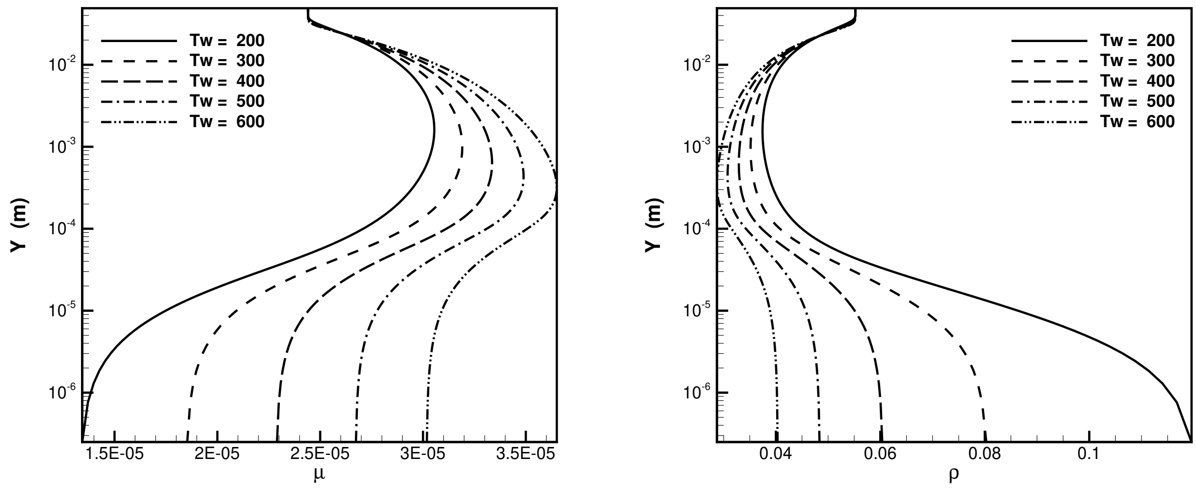

(a) (b)

FIGURE 6.11: Variation of (a) near-wall viscosity (Pa.s) and (b) near-wall density (kg/m^3) in wall-normal direction for different wall temperatures.

The reason for the observed trend is due to the changes in near-wall properties with wall temperature changes, and these, in turn, lead to expansion/contraction of viscous sub-layer, sub-sonic layer or the boundary layer. As the wall-temperature increases, the near-wall viscosity increases ([19] and [41]) as shown in Fig. 6.11b. Increase in viscosity leads to decrease in Reynolds number and subsequent increase in boundary layer thickness δ With respect to density, it is found that as the wall-temperature increases the near-wall density decreases ([19], [41] and [44]), as shown in Fig. 6.11a , which leads to increase in boundary layer thickness on similar analogy. Fig. 6.12 shows the movement of the sonic

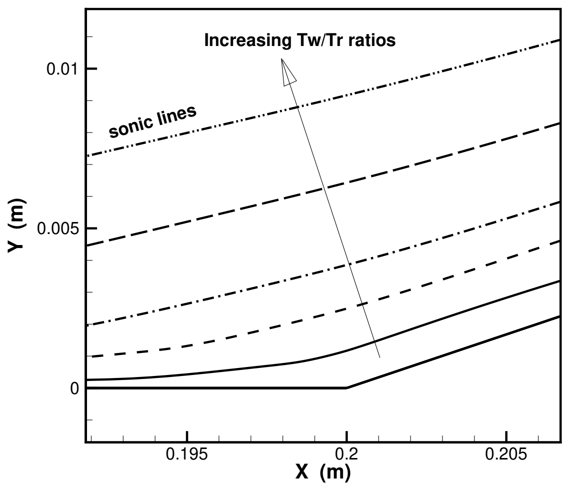

FIGURE 6.12: Shifting of the sonic line away from the wall for different wall temperatures.

line (area below the sonic line can be considered as subsonic channel thickness) with an increase in wall-temperature. It is seen that as the wall-temperature increases, the sonic line moves away from the wall or the subsonic channel thickness increases leading to an increase in separation bubble length. Compared to viscous sub-layer and the boundary layer, the changes in sub-sonic layer (sonic line or sub-sonic channel thickness) is found to be the reason for the changes in separation length. If the sonic line moves away from the wall (increase in the subsonic layer thickness), the size of the separation bubble is found to increase and vice-versa. Hence, separation length is analyzed with this boundary layer parameter in all the results presented further. Of all the near-wall properties, density is found to be an important parameter. If the near-wall density increases, the separation length decrease, and vice-versa. Based on this, the changes in near-wall density and movement of the sonic line with respect to the wall is used for the boundary layer analysis of the subsequent results.

The wall-to-recovery-temperature ratio is found to be an important scaling parameter

TABLE 6.3: Changes in wall-to-recovery temperature ratio for different wall temperatures.

T_w	M	θ	P_d/P_u	T_w/T_r
200	4.09	18.56	4.88	0.12
300	4.09	18.56	4.88	0.18
400	4.09	18.56	4.88	0.24
500	4.09	18.56	4.88	0.29
600	4.09	18.56	4.88	0.35

for separation length studies, as discussed in section 2.6. It not only takes into consideration the effect of wall-temperature T_w but also the effect of temperature T at the edge of boundary layer (i.e., in outer inviscid flow region) and the Mach number M. As seen in Table 6.3, as the wall-temperature is increased, the pressure ratio does not change since the shock-strength is not changing due to fixed Mach number and fixed ramp angle.

6.5 Effect of Mach number

The effect of increasing the Mach number on flow separation was studied, mainly experimentally, by many researchers in the past. However, there was very few numerical study for the above. Simulations are performed to study the effect of only Mach number keeping all other parameters constant and varying the Mach number M as 3.00, 3.50, 4.097, 4.50 and 5.00, where M = 4.097 corresponds to on-design conditions. The conditions used for simulations are P = 6.592 kPa, T = 426.55 K, ρ = 0.05385 kg/m^3, and T_w = 850 K.

Fig. 6.13a gives a comparison of the CFD computed pressure rise for different Mach numbers with the inviscid pressure jump (calculated using Rankine-Hugoniot relations) indicated by the dotted line. It is evident that the pressure jumps are always lower than the respective inviscid values. As the Mach number increases, the upstream influence (pressure rise) moves closer to the corner, which indicates decrease in size of separation bubble if flow is already separated. The stream-wise (x) direction is normalized by the displacement boundary layer thickness the boundary layer. The displacement boundary layer thickness of extracted boundary layer profiles were 0.008582, 0.009112, 0.009816, 0.01032, and 0.01260 m for Mach number of 3.00, 3.50, 4.09, 4.50, and 5.00, respectively. Fig. 6.13b shows the variation of normalized separation length for different Mach numbers. As concluded from the previous plots, the size of the separation bubble decreases as the Mach number increases.

The variation of separation length with the Mach number has been studied in the past ([44], [40],[42]), but the reasoning behind the observed phenomenon is not well-defined

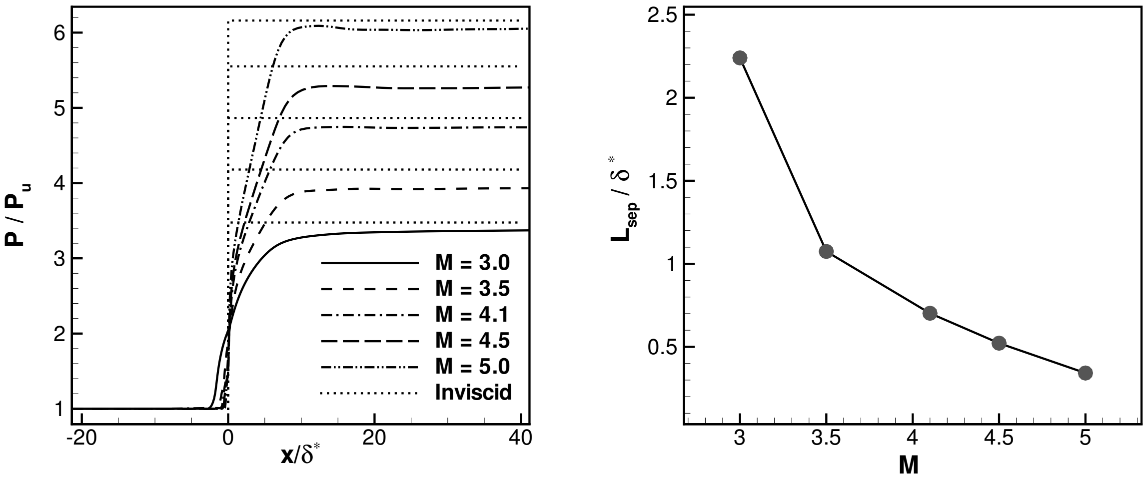

(a) (b)

FIGURE 6.13: Variation in (a) wall-pressure distribution, and (b) normalized separation length for different Mach numbers.

or least discussed compared to all other parameters. As the Mach number increases, the pressure jump across the shock increases which makes it a case of adverse pressure gradient and hence the separation length is expected to increase but the observed trend, as seen in results above, is opposite to it. John et al. [40] reasoned that for higher Mach number means higher kinetic energy of the flow for the same internal energy which leads to a decrease in separation length. Based on their computational study, Pasha et al. [44] commented - *More investigations required to understand this behavior* - [44] concerning the effect of Mach number on flow separation. Similar observations were reported by Elfstrom et al. [29], but it did not include any reasoning for the observed trend.

Fig. 6.14 shows the variation in separation length for different shock-strength obtained by varying Mach number. It is seen that as the Mach number increases, the shock-strength P_d/P_u increases, whereas the separation length ($L/\delta^\star$) decreases. However, using the Souverein's scaling law, as the Mach number increases, the normalized shock-strength ($S_e^\star$ in Souverein's scaling law) decreases, and the normalized separation length ($L^\star$) also decreases. The wall-temperature here is varied such that the ratio $T_w/T_r = 1$ for all the three cases. $T_w = 1109.75$ K for M = 3.0, $T_w = 1356.48$ K for M = 3.5 and $T_w = 1700.80$ K for M = 4.097 case which gives $T_w/T_r = 1$ for all the three cases. The Souverein's scaling law was developed using the data available in the literature that corresponded to adiabatic wall conditions, and hence, the above results match well with the scaling law.

Fig. 6.15b shows the changes in near-wall density with the changes in Mach number. It is seen that as the Mach number increases the density near-wall increases, which should

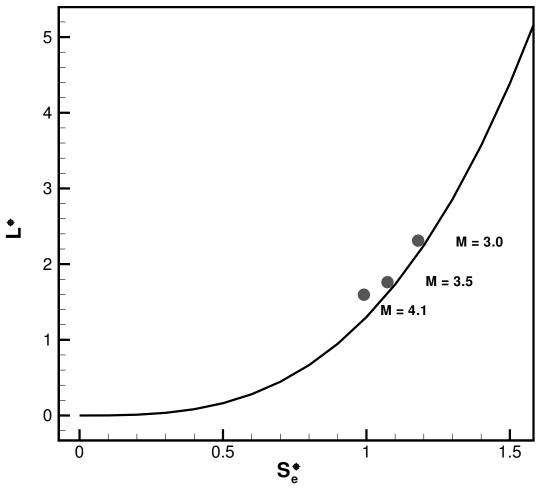

FIGURE 6.14: Normalized separation length obtained for different Mach numbers plotted against the normalized shock-strength using the scaling law proposed by Souverein et al [56], and its best curve fit equation.

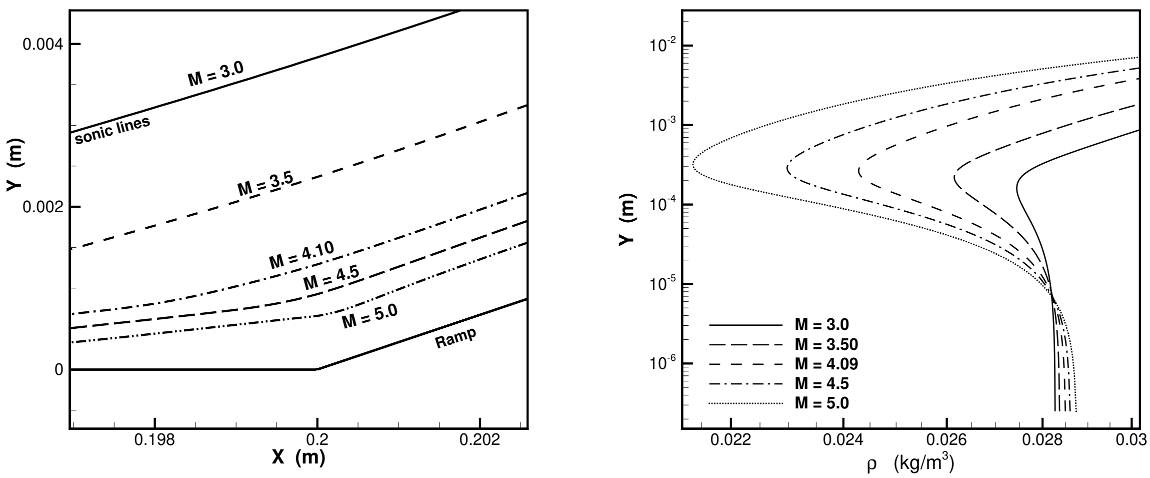

(a) (b)

FIGURE 6.15: (a) Shifting of sonic lines and (b) changes in near-wall density for different Mach numbers.

lead to a decrease in boundary layer thickness and consequently, decrease in separation length. From Fig. 6.15a it is seen that as the Mach number increases, the sonic line moves closer to the wall thereby shrinking the subsonic channel thickness and this leads to decrease in separation bubble size and consequently decrease in separation length.

Increase in pressure gradient should always lead to a decrease in flow velocity for flow to separate. In the present case, as the Mach number increases the pressure jump across

TABLE 6.4: Different ratios across the shock for different Mach numbers.

M	θ	$\frac{P_d}{P_u}$	$\frac{T_w}{T_r}$	$\left(\frac{P_d}{P_u}\frac{T_w}{T_r}\right)$
3.00	18.56	3.47	0.76	2.64
3.50	18.56	4.06	0.62	2.52
4.09	18.56	4.88	0.49	2.39
4.50	18.56	5.49	0.43	2.36
5.00	18.56	6.33	0.36	2.28

the shock increases, but the flow velocity near the wall is also increasing. Thus, an increase in Mach number has two effects: one, it leads to an adverse pressure gradient due to the increase in shock-strength and two, the kinetic energy of flow increases. Higher kinetic energy offers greater inertia to flow, leading to a decrease in separation length, as pointed by John et al. [40]. This shows, apart from the changing shock-strength, the flow kinetic energy is also an important parameter and should be considered in the analysis of flow separation. As the Mach number increases, the separation length decreases and wall-to-recovery-temperature ratio (see Table 6.4) is also found to decrease as T_r is function of Mach number as well. The ratio T_w/T_r takes into account the effect of upstream Mach number. However, it fails to take into account the effect of shock-strength, i.e., the changes in pressure jump P_d/P_u across the shock. As the Mach number increases, the shock-strength P_d/P_u increases, as shown in Table 6.4. The product of these two parameters $(P_d/P_u)*(T_w/T_r)$ takes into account the effect of both wall-to-recovery-temperature ratio and shock-strength. With respect to changes in Mach number, the separation length is found to scale with this parameter. This parameter $(P_d/P_u)*(T_w/T_r)$ is used to analyze the changes in separation length due to different flight conditions in chapter-7.

6.6 Effect of Reynolds number Re_δ

Compared to all other parameters, the effect of Reynolds number Re_δ (Reynolds number based on boundary layer thickness δ) on flow separation, in shock boundary layer interactions, is relatively least studied in the recent past. Simulations were done to study the effect of Reynolds number by increasing the Reynolds number Re_δ in the range of 6.00E+04, 7.29E+04, 8.88E+04, 1.02E+05 and 1.13E+05 keeping the wall temperature equal to 1300 K for all the cases. The Re_δ = 1.13E+05 corresponds to on-design condition (keeping all other parameters constant). The above range of Reynolds number is achieved by increasing the length of the flat plate in range of 1.00, 1.25. 1.50, 1.75 and 2.00 m, respectively.

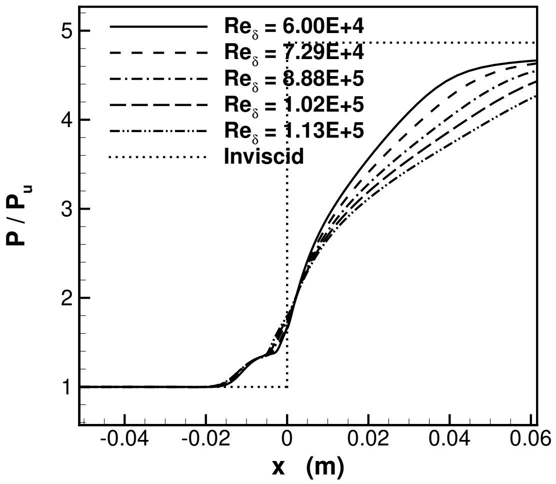

(a)

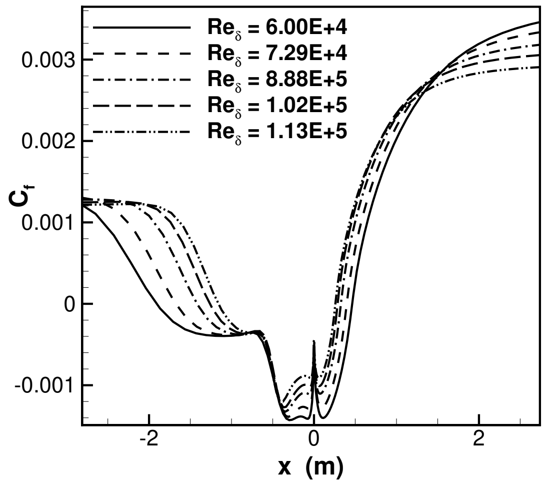

(b)

FIGURE 6.16: Variation in (a) wall-pressure and (b) skin-friction distribution for different Reynolds number Re_δ.

Fig. 6.16a shows the pressure distribution for different Reynolds numbers near the separation region. It is observed that the effect of Reynolds number Re_δ on the extent of interaction length is relatively small as pointed by Holden et al. [68]. Increase in Reynolds number Re_δ leads to a small rise in the upstream influence as seen. It is difficult to predict the effect on separation size from the pressure plot as the upstream influence is not distinguishable. From the skin-friction plot in Fig. 6.16b, it is observed that the separation points moves slightly upstream of the corner whereas the re-attachment point moves downstream of the corner by a relatively much smaller distance leading to increase in separation length, as observed by Pasha et al. [44].

Babinsky et al. [19] pointed out that - for a turbulent boundary layer, the influence of the Reynolds number on L/δ is less clear. Some researchers reported that the separation length increases with increase in Reynolds number Re_δ ([44], [68]) while some have reported the opposite trend ([33], [69] and [29]). Pasha et al. [44] showed that as the Reynolds number increases, the size of the separation bubble increases due to an increase in boundary layer thickness. Spaid et al. [28], from their experimental investigation, found that as the Reynolds number Re_δ increased, the incipient separation angle decreased (which means the separation length increased, discussed in section 3). Kuehn et al. [70], from their experimental investigation, found the same trend as above. On the other hand, Elfstrom et al. [29], Law et al. [30] and Roshko et al. [32], found that the incipient separation angle increases with an increase in the Reynolds number which means the size of the separation bubble decreases with an increase in Re_δ, and this is contradictory to the above findings. Settles et al. [33] did an experimental investigation and showed that the upstream influence *(or the size of the separation bubble)* decreases with increase in Reynolds number.

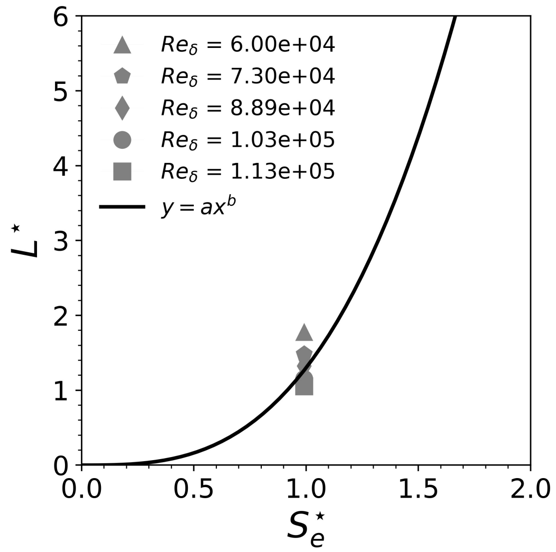

FIGURE 6.17: Normalized separation length obtained for different Re_δ plotted against the normalized shock-strength using the scaling law proposed by Souverein et al [56], and its best curve fit equation.

Fig. 6.17 shows the variation of the normalized separation length $L^\star$ with the shock-strength $S_e^\star$ for different Reynolds number Re_δ as per the scaling law proposed by Souverein et al [56]. For all the cases considered in this study, the Reynolds number based on momentum thickness Re_θ is less than 10^5, and hence the value of k is taken to be equal to 3 for all cases . Since k is constant, the normalized shock-strength $S_e^\star$ also remains constant, as seen in Fig. 6.17. The normalized separation length decreases with an increase in Reynolds number Re_δ.

As shown in Fig. 6.18a, the sonic line moves away from the wall by a very small distance as the Reynolds number Re_δ) increases. Due to the movement of the sonic line away from the wall, subsonic channel thickness increases and size of separation length increases (as seen in Fig. 6.18b). This observed trend is consistent with that reported by Pasha et al. [44], Holden et al. [68], Spaid et al [28], and Kuehn et al [70]. The separation length, normalized by the incoming displacement boundary layer thickness, is shown in Fig. 6.18d. The displacement boundary layer thickness of the extracted boundary layer profiles are 0.005688, 0.006836, 0.008219, 0.009439, and 0.01035 m for the flat plate simulations of length 1.00, 1.25, 1.50, 1.75 and 2.00 m, respectively. As observed from Fig. 6.18b and 6.18d, when the separation length is normalized by the incoming displacement boundary layer thickness $\delta^\star$, the trend becomes opposite. This

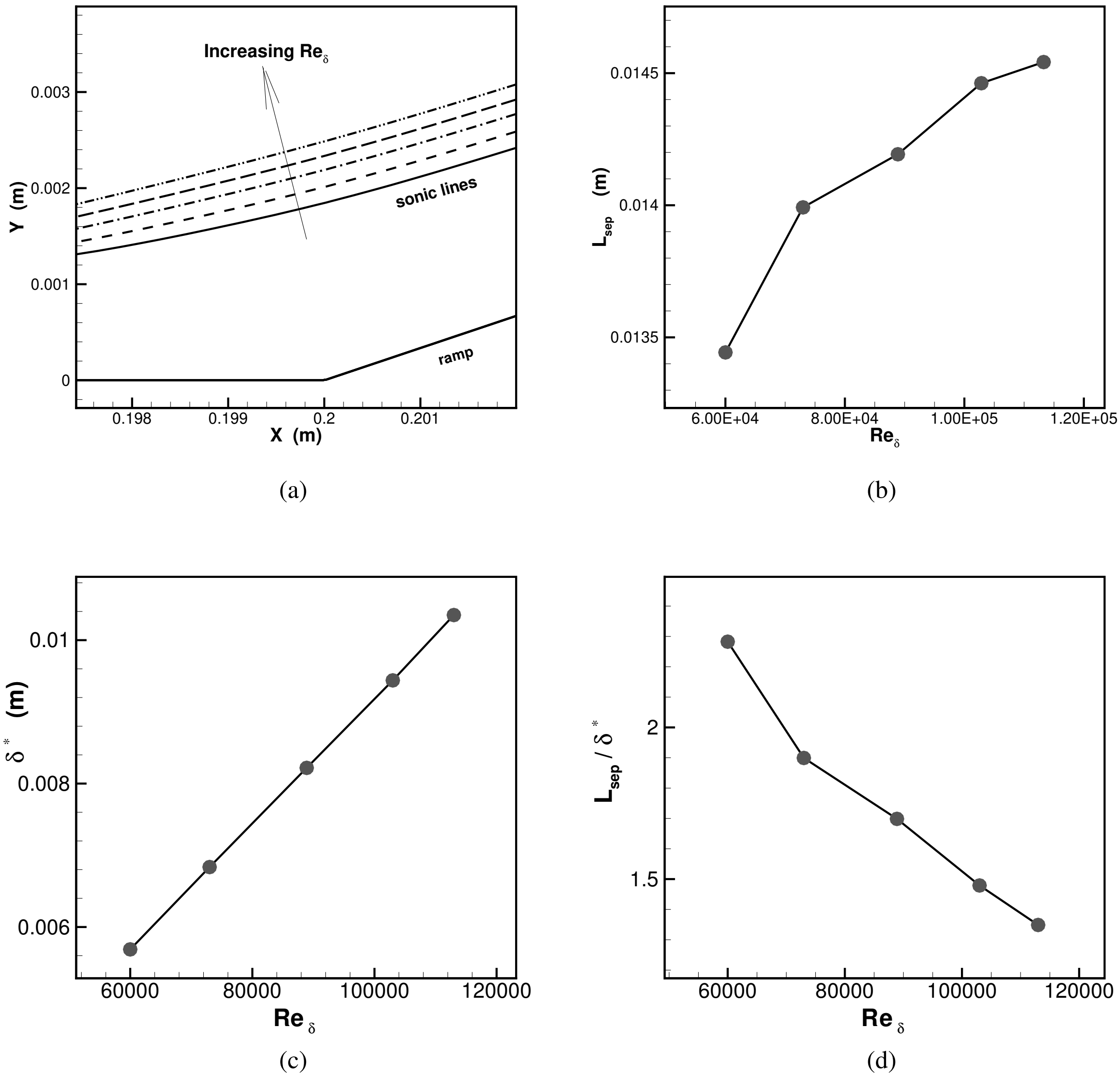

FIGURE 6.18: (a) Shifting of the sonic line, (b) the variation in separation length, (c) variation in the displacement boundary layer thickness $\delta^\star$ and (d) variation of the normalized separation length for different Reynolds number Re_δ.

trend reversal is because the variation in the $\delta^\star$ is much more significant as compared to that in the separation length L_{sep} (comparing Fig. 6.18b and Fig. 6.18c). While the changes in the separation length are of the order of 10^{-3}, the changes in displacement boundary layer thickness are of the order of 10^{-2}. Hence, the normalized separation length decreases as the Reynolds number Re_δ increases. The same trends were found when the normalization of separation length was done with incoming boundary layer thickness δ rather than the displacement boundary layer thickness $\delta^\star$. These observations are consistent with that reported by Settles et al. [33], [69] and Elfstrom et al. [29].

The separation length L_{sep} is found to increase with an increase in Reynolds number Re_{δ} and the boundary layer thickness (δ as well as $\delta^{\star}$) are directly proportional to Re_{δ} by definition. As the flat plate length is increased, all the three boundary layer parameters - δ, $\delta^{\star}$ and Re_{δ} - increases. Thus, the separation length L_{sep} is directly proportional to boundary layer thickness - δ as well as $\delta^{\star}$. The separation length L_{sep} is normalized with boundary layer values (δ or $\delta^{\star}$) as separation length is proportional to these parameters ($L_{sep} \propto \delta$ or $\delta^{\star}$). Thus, the normalization itself takes into account the effect of Reynolds number based on boundary layer values (δ or $\delta^{\star}$).

6.7 Summary

Fig. 6.19 shows the summary of various parameters that affect the separation bubble in high-speed turbulent flows. As the ramp angle θ increases, the shock-strength P_d/P_u increases, and the separation length increases, as shown in Table 6.5. The wall-to-recovery-temperature ratio T_w/T_r does not change with the ramp angle. With an increase in Mach number, the shock-strength P_d/P_u increases whereas the wall-to-recovery-temperature ratio T_w/T_r decreases, and the separation length also decreases. Thus, the Mach number affects both the shock-strength and the upstream flow, and hence, both scaling parameters should be taken into account. As the wall-temperature increases, shock-strength P_d/P_u does not change, and the wall-to-recovery-temperature ratio increases, as shown in Table 6.5. The changes in Reynolds number Re_{δ} or the incoming boundary layer thickness, neither affect the shock-strength nor the wall-to-recovery-temperature ratio. However, since the separation length L_{sep} is normalized with the incoming boundary layer property $\delta^{\star}$, this normalization itself takes into account the effect of incoming boundary layer thickness or Reynolds number Re_{δ}.

TABLE 6.5: Variation of normalized separation length with respect to various parameters.

Parameters	Separation length	Shock-strength	Wall-to-recovery-temperature ratio
$\theta\ \uparrow$	$L_{sep}/\delta^{\star}\ \uparrow$	$P_d/P_u\ \uparrow$	$T_w/T_r\ -$
$M\ \uparrow$	$L_{sep}/\delta^{\star}\ \downarrow$	$P_d/P_u\ \uparrow$	$T_w/T_r \downarrow$
$T_w\ \uparrow$	$L_{sep}/\delta^{\star}\ \uparrow$	$P_d/P_u\ -$	$T_w/T_r \uparrow$
$Re_{\delta}\ \uparrow$	$L_{sep}/\delta^{\star}\ \downarrow$	$P_d/P_u\ -$	$T_w/T_r\ -$

Using the conclusions/understanding drawn from the above study, one can justify/predict how the separation bubble behaves in actual flight conditions where changes in one parameter lead to simultaneous changes in multiple parameters. Concerning the scaling of

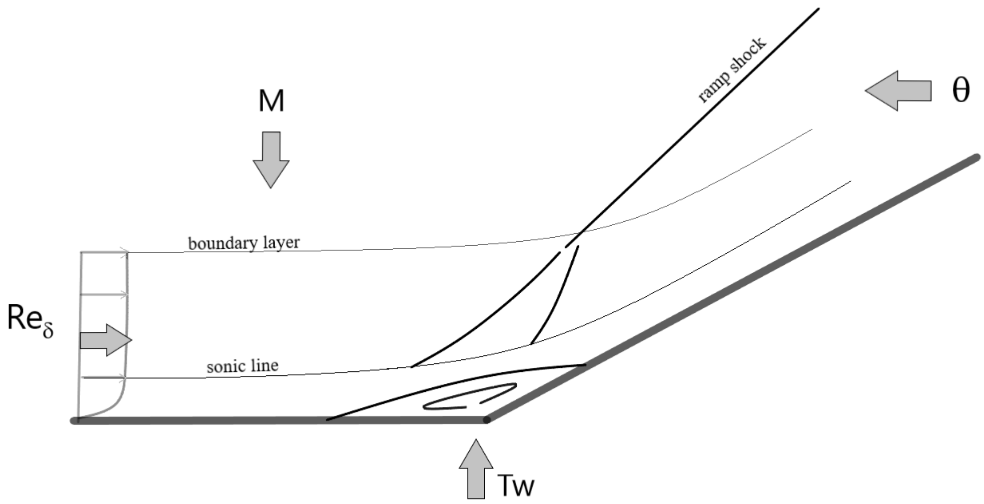

FIGURE 6.19: Canonical parameters affecting the separation length for supersonic flow over a compression ramp geometry.

separation length, it is found that both T_w/T_r and P_d/P_u are essential non-dimensional parameters for the study of scaling of separation length. The product of these two ratios (T_w/T_r) and (P_d/P_u) would be the relevant scaling parameter for the study of separation length changes with respect to different flight parameters.

Chapter 7

Effect of flow separation in hypersonic intakes

7.1 Introduction

In this chapter, the changes in the separation length with different flight parameters is studied and the effect of the separation bubble on the lift and drag of the intake is quantified in terms of percentage difference. The four flight parameters considered are:

1. Flight Mach number : M_1
2. First ramp length : L1
3. Angle of attack : α
4. Cruise Altitude : z

These four flight parameters are shown in Fig. 7.1. The observed trend in separation length with different flight parameters is justified based on the understanding drawn from the study of canonical parameters affecting flow separation. Further, the effect of flow separation on intake generated lift and drag is quantified and scaling of the separation length is carried out with a non-dimensional scaling parameter. The effect of varying the flight Mach number on separation length and its effect is discussed in section 7.2 along with the scaling parameter analysis. Similarly, the results for changes in separation length, analysis of the results and the scaling parameter with respect to other flight parameters - first ramp length, angle of attack, and cruise altitude - are discussed in sections 7.3, 7.4, and 7.5, respectively. The overall analysis of the scaling parameter is presented in section 7.6 with summary of the chapter at the end.

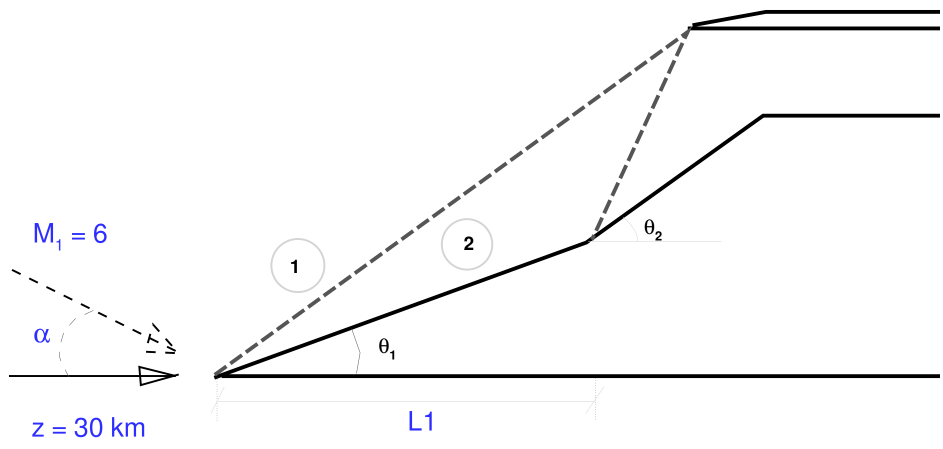

FIGURE 7.1: Schematic of scramjet intake and the flight parameters varied.

Methodology

To study the effect of a given flight parameter, the conditions at station-1 (see schematic of intake in Fig. 7.1) is varied, and this leads to changes in multiple parameters at station-2 of the scramjet intake. The conditions given at station-1 (see Table 7.1) are used to calculate the conditions at station-2 using the inviscid calculations and these are used as the inlet conditions for the simulations. For example, to study the effect of flight Mach number M_1, the Mach number M_2 and flow-properties (P_2, T_2, and ρ_2) at station-2 are computed for the corresponding values of M_1 and flow-properties (P_1, T_1, and ρ_1 at z = 30 km) at station-1. The first ramp is simulated using the flow conditions obtained at station-2 and the boundary layer profiles are extracted at the required locations. Same methodology is applied for the study of other flight parameters. **Note:** The values shown in second column of Table 7.1 correspond to on-design condition while that in last column correspond to off-design flight conditions. All the results presented in this chapter are based on the values given in Table 7.1.

TABLE 7.1: On and Off-design parameters for the study of flight parameters affecting flow separation.

Flight parameters	On-design	Off-design conditions
z (km)	30	26, 28, 32, 34
M_1	6	4, 5, 7, 8
α	0	-4, -2, 2, 4
$L1$ (m)	2.00	1.50, 1.75, 2.25

A weak boundary layer leading edge shock at the first ramp, and its effect on intake generated lift and drag is not considered in the present results. Fig. 7.2 shows the schematic of intake of scramjet rotated in clockwise direction by θ_1 degrees. Here the first ramp is made horizontal and the incoming flow is inclined at an angle θ_1 with the horizontal. In other words, Fig. 7.1 is rotated in clockwise direction by θ_1 degrees to obtain the schematic shown in Fig. 7.2. The first ramp is kept horizontal, and simulations of flat plate are done using the conditions at station-2 as the free-stream conditions. This leads to isolation of the effect of first ramp shock. However, still, a weak boundary layer leading edge shock is formed at the leading edge of first ramp due to the formation of the boundary layer, as shown in Fig. 7.2. Due to this, the CFD computed wall pressure at first ramp will be higher than that found using inviscid solution, as shown in Fig. 7.3a. The boundary layer profiles extracted from the first ramp does not include the effect of boundary layer shock (the boundary layer profiles used as an inlet for simulations does not include the discontinuity due to boundary layer shock).

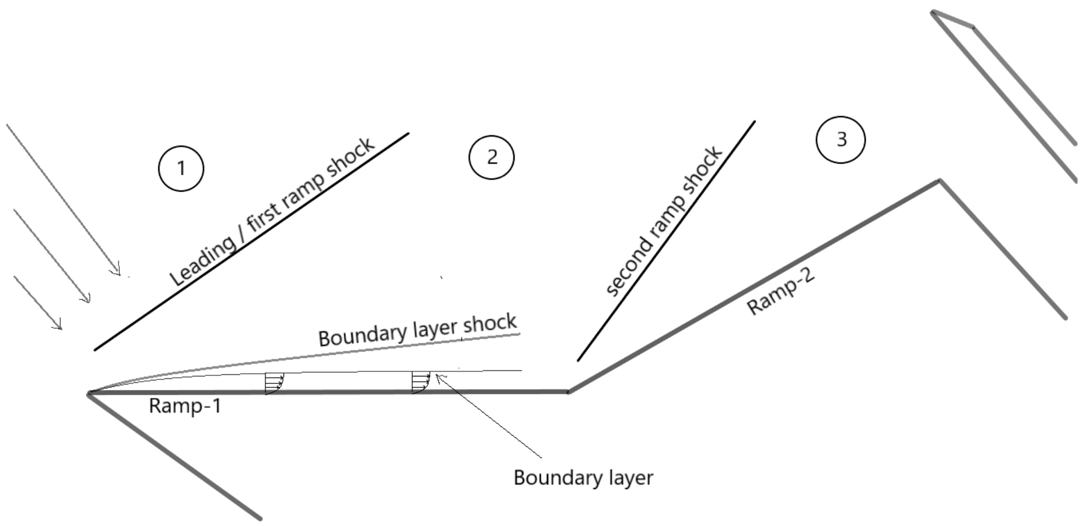

FIGURE 7.2: Intake of scramjet engine, rotated in clock wise direction such that first ramp is horizontal to incoming flow, showing the weak boundary layer (leading edge) shock formed at the first ramp.

The CFD computed wall-pressure over the first ramp is little higher than the inviscid values as shown in Fig. 7.3a, due to the formation of weak boundary layer leading edge shock over the first ramp. The modification in wall-pressure distribution due to the separation bubble and separation shock occurs only near the corner and downstream of the corner i.e. across the second ramp. Since, the objective of the current work is to study only the effect of the ramp shock-induced separation on intake generated lift and drag, the pressure jump due to the weak boundary layer shock at the leading edge is not to be considered (or its effect is to be removed/isolated) in the calculations of lift and drag. Accordingly, inviscid pressure at first ramp is taken to be equal to the CFD computed wall pressure at first ramp, as shown in Fig. 7.3b, which clearly shows only the effect of separation bubble over the first ramp. Over the second ramp, the effect of separation bubble

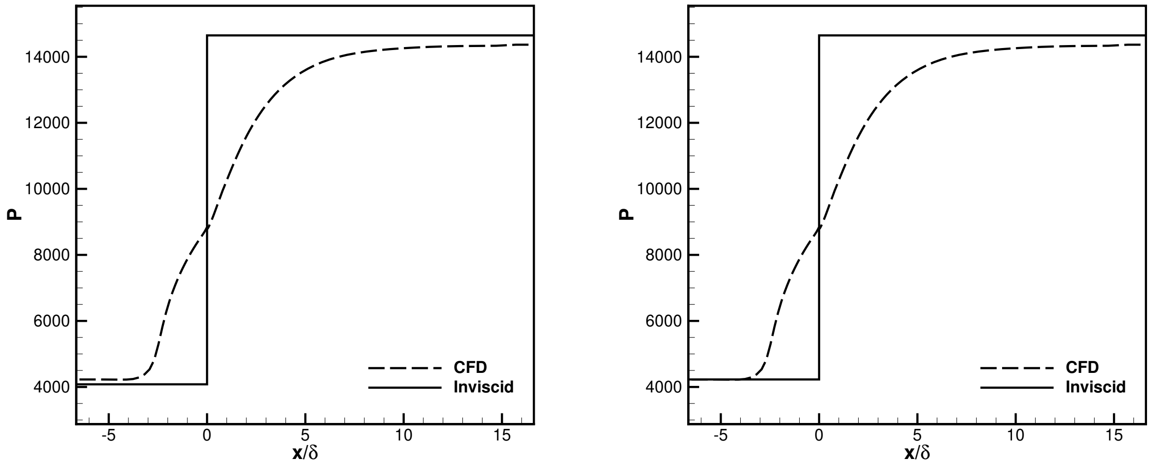

(a) (b)

FIGURE 7.3: Pressure distribution (inviscid vs CFD) plotted using two different approach: (a) shows the effect of boundary layer shock at first ramp as well as the second ramp shock induced separation and (b) shows only the effect of second ramp shock induced separation.

as well as separation shock is observed. The methodology shown in Fig. 7.3a is named as Approach-A whereas that shown in Fig. 7.3b is named as Approach-B. The approach-B isolates the effect of weak boundary layer shock at leading edge. All the results presented in this work are based on Approach-B. In computation of the effect of shock-induced separation on lift and drag forces (in terms of percentage difference) acting on the two ramps, the methodology shown in Fig. 7.3b (Approach-B) is adopted for all the flight parameters.

7.2 Effect of flight Mach number

For an intake shown in Fig. 7.1, if the flight Mach number is varied then, at station-2, along with the Mach number, pressure, temperature, and density will also vary. So if the flight Mach number M_1 is changed, the effect observed on the separation bubble is the combined effect of all changes in all these parameters (M_2, P_2, T_2, and ρ_2) and is not just the effect of Mach number. The flight Mach number is varied, as given in Table 7.2, and its effect on the separation length is studied in detail in this section.

Simulations are done to study the effect of flight Mach number using the conditions as given in Table 7.2 keeping the wall temperature equal to 1700 K. First, the first ramp was simulated using the conditions at station-2, and the boundary layer profiles were

TABLE 7.2: Effect of varying the flight Mach number M_1 on flow parameters at station-2.

M_1	M_2	P_2	ρ_2	T_2
4	2.98	4080.10	0.041	341.74
5	3.58	5225.66	0.047	380.91
6	4.09	6592.30	0.053	426.55
7	4.53	8178.60	0.059	478.93
8	4.90	9995.87	0.064	538.31

extracted at the required location. The displacement boundary layer thickness of the extracted boundary layer profile was 0.01127, 0.01093, 0.01081, 0.01077 and 0.01083 m for the flight Mach number of 4, 5, 6, 7 and 8, respectively. The extracted boundary layer profiles were given as inlet to the computational domain to study the effect of flight Mach number.

Fig. 7.4a gives the comparison of the pressure rise for different flight Mach numbers with respective inviscid pressure jump indicated by the dotted line. The computed pressure distribution over the wall matches closely with the inviscid data. The upstream influence is found to be maximum for the lowest flight Mach number and minimum for the highest flight Mach number. Further, the computed pressure rise across the shock is always lower than the inviscid data for all cases. For lower flight Mach numbers, there is a small difference in the computed and inviscid pressure rise. However, as the flight Mach number increases, this difference (in pressure jump) between the computed and inviscid results keeps on increasing. From the skin-friction distribution (Fig. 7.4b), it is observed that increasing flight Mach number pushes the separation and reattachment point closer towards the corner and thereby reducing the separation length. Fig. 7.4c shows the movement of the separation and reattachment points from the corner for different flight Mach numbers; the corner being at X = 0.2 location. The length of the separation bubble is taken as the distance between the separation and reattachment points, and the separation length decreases with the increase in flight Mach number, as seen in Fig. 7.4d.

The variation in separation length, with a given flight parameter, can be predicted/justified based on understanding drawn from the study of canonical parameters, discussed in the previous chapter. As the flight Mach number increases, along with Mach number, the pressure, temperature, and density at station-2 are also changing. Thus, it is a cumulative effect of Mach number and the three flow properties - pressure, temperature, and density. Both Mach number M and flow-properties (P, ρ and T) have the same effect on separation, i.e., increase in M, P, ρ or T leads to a decrease in separation length. Thus, the cumulative effect of the above parameters should lead to a decrease in separation length, and observed results are consistent with this.

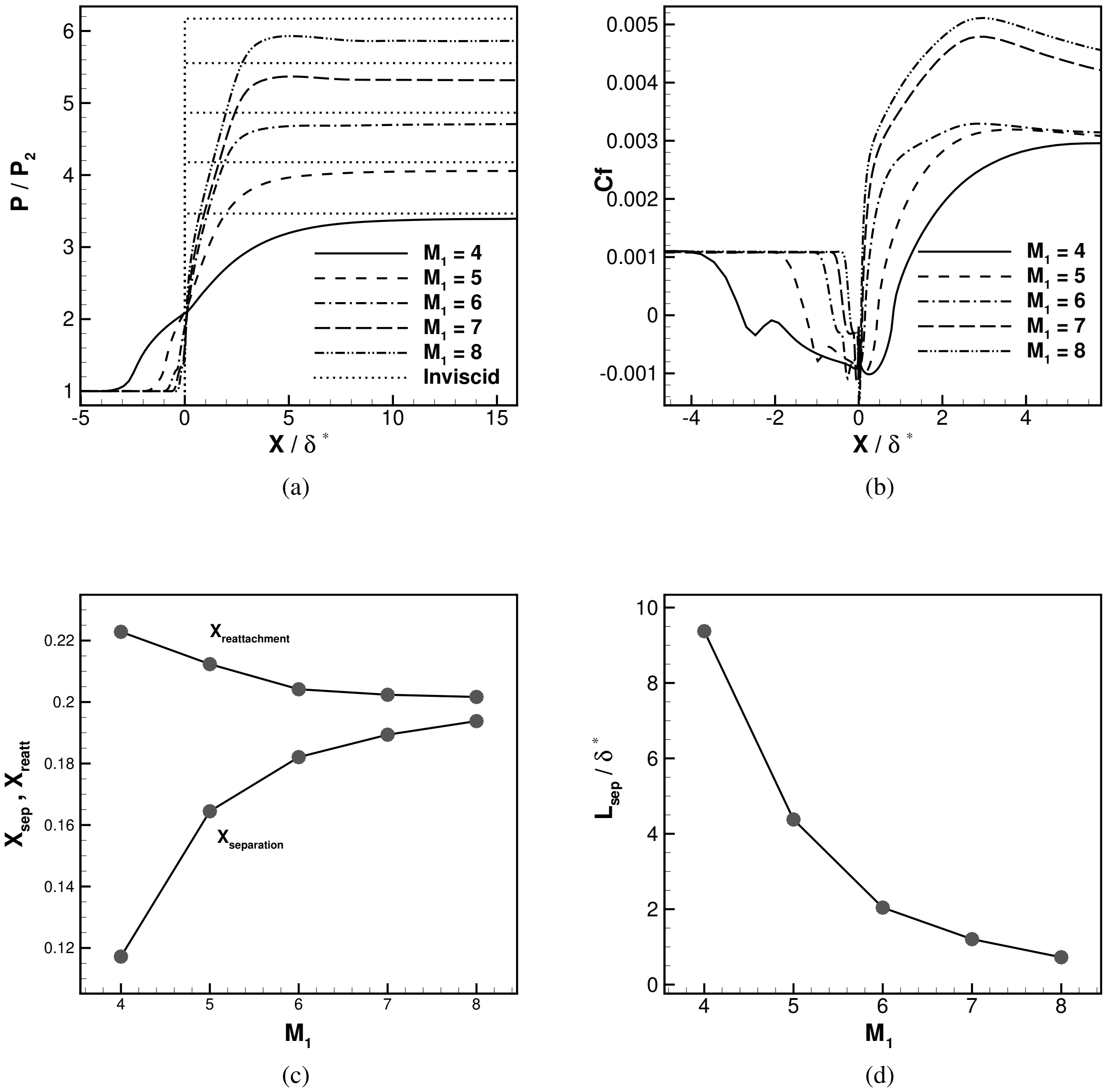

FIGURE 7.4: Variation in (a) wall-pressure distribution, (b) skin-friction distribution, (c) movement of separation and re-attachment points from corner, and (d) normalized separation length for different flight Mach numbers.

Based on the analysis of the results with the scaling parameter, in the previous chapter, it was found that the wall-to-recovery-temperature ratio T_w/T_r and the shock-strength P_3/P_2 are two important scaling parameters. See section 2.6 for details regarding the wall-to-recovery-temperature ratio. The variation in separation length with changes in flight Mach number is analyzed with these scaling parameters in this section.

Increase in flight Mach number leads to a decrease in separation length as well the ratio T_w/T_r as given in Table 7.3. This shows the ratio T_w/T_r is an important parameter as

TABLE 7.3: Changes in scaling parameter for different flight Mach numbers.

M_1	M_2	$\dfrac{T_w}{T_r}$	$\dfrac{P_3}{P_2}$	$\left(\dfrac{T_w}{T_r}\dfrac{P_3}{P_2}\right)$	$\dfrac{L_{sep}}{\delta^\star}$
4	2.98	1.92	3.46	6.66	9.37
5	3.58	1.36	4.17	5.67	4.37
6	4.09	1.00	4.88	4.88	2.04
7	4.53	0.76	5.55	4.23	1.20
8	4.90	0.60	6.16	3.69	0.72

not only it takes into consideration the effects of wall-temperature and free-stream temperature but also the effect of Mach number. However, as flight Mach number changes the shock-strength P_3/P_2 also changes, and hence, it should also be taken into consideration. With an increase in flight Mach number, the shock-strength increases (see Table 7.3) whereas the separation length decreases. Even though the changes in separation length does not scale with the shock-strength, it scales with the product of these two parameters, i.e., separation length is found to scale with the product of ratios (T_w/T_r) and (P_3/P_2), as seen in Table 7.3. Thus, the scaling parameter $\left(\dfrac{T_w}{T_r}\dfrac{P_3}{P_2}\right)$ takes into account the effect of shock-strength as well as the wall-temperature and flow-parameters (Mach number and Temperature).

As the flight Mach number increases, the size of the separation bubble decreases. Thus, at flight Mach number ($M_1 = 4, 5$) lower than the on-design condition, the separation bubble size would be large which leads to deterioration of the aerodynamic properties of the vehicle surface. On the other hand, at a Mach number (M_1 = 7, 8) higher than on-design condition, even though the size of separation bubble is very small, the pressure jump across the shock is lower as compared to an inviscid solution, and this affects the aerodynamic properties. Fig. 7.5 shows the percentage difference between the inviscid solution and CFD computed lift & drag, due to pressure forces, acting over the two ramps for different flight Mach numbers. Even though the absolute values of lift and drag over the two ramps are different, their percentage difference with inviscid solution remains the same. Hence, the percentage difference for both lift and drag is shown in the same plot, i.e., the percentage difference given in this plot is applicable for both lift and drag over the given ramp. Same methodology is applied in discussion of lift and drag deviation with other flight parameters.

Since the separation length decreases with the increase in flight Mach number, the percentage difference is also expected to decrease for both the ramps. For the first ramp, the percentage difference decreases with the increase in flight Mach number whereas for the second ramp it decreases till M_1 = 6 and then starts to increase (Negative percentage

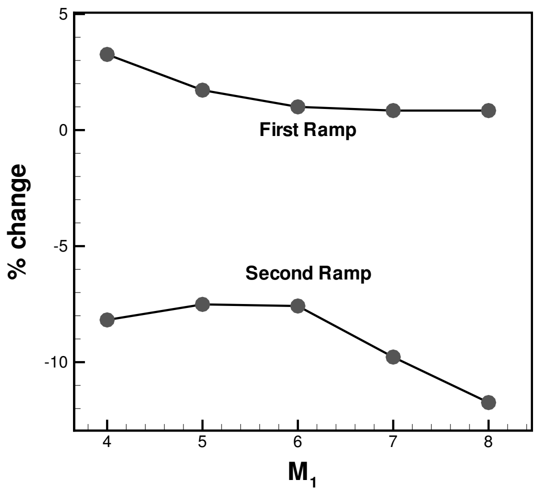

FIGURE 7.5: Percentage change in lift or drag forces acting on the two ramps for different flight Mach numbers.

difference indicates the computed pressure is lower than the inviscid whereas positive difference shows the computed pressure is higher than the inviscid). The reason for this is CFD computed pressure at ramp-2, i.e., P_3, is always lower than the inviscid solution. This difference further increases with an increase in flight Mach number. Thus, at higher Mach numbers (M_1 = 7, 8), the computed pressure jump is much lower than the inviscid, and hence, the percentage difference increases and the curve for ramp-2 follows a trend opposite to that expected, as seen in Fig. 7.5. Over the first ramp, the percentage difference is within 5% whereas over the second ramp it can be as high as 12% for highest of the off-design conditions. This high percentage difference for M_1 = 8 case is due to two effects - (i) presence of separation bubble which modifies the pressure distribution across the corner of the two ramps and (ii) pressure jump across the shock which is much lower than that obtained through Rankine-Hugoniot (inviscid) relations. The wall-pressure distribution over the first ramp is affected only by the separation bubble whereas that over the second ramp is affected by the separation bubble as well as the pressure jump across the shock. The contribution of skin-friction force is found to be very small (see Appendix-C), and hence its effect is not discussed for this as well as for other flight parameters.

7.3 Effect of first ramp length

The first ramp angle θ_1 is computed using the flow conditions at station-1 such that the shock-on-lip condition is satisfied. If the first ramp length L1 is changed, then to satisfy the shock-on-lip condition, the second ramp angle also has to be varied. Table 7.4 shows the required second ramp angle θ_2 for different lengths (L1) of first ramp to satisfy the shock-on-lip condition. The first ramp length cannot be taken lower than 1.50 m as the second ramp angle would be too small to have a shock of any considerable strength for flow to separate. On the other side, it cannot exceed 2.25 m as that would lead to a relatively much larger second ramp angle θ_2, which may lead to the formation of the detached bow shock.

TABLE 7.4: The second ramp angle θ_2 required for different first ramp lengths to satisfy the shock-on-lip condition

M_1	$L1$ (m)	M_2	θ_2
6	1.50	4.09	4.99
6	1.75	4.09	10.33
6	2.00	4.09	18.56
6	2.25	4.09	30.63

Using the same methodology, as discussed in section 7.1, first, the first ramp is simulated, boundary layer profiles are extracted at required locations and used as an inlet for simulations using different ramp angle θ_2, as given in Table 7.5. The displacement boundary layer thickness of the extracted boundary layer profile was 0.008992, 0.009859, 0.01081, and 0.01241 m for firs ramp lengths of 1.50, 1.75, 2.00 and 2.25 m, respectively. The effect of varying the first ramp length L1 is the cumulative effect of changes in Reynolds number Re_δ (or incoming boundary layer thickness) and the second ramp angle. Table 7.5 shows the conditions used for the simulations to study the effect of ramp length. The adiabatic wall temperature conditions are used for all the cases.

TABLE 7.5: Effect of varying the first ramp length L1 on the conditions at station-2.

L1 (m)	M_2	θ_2	ρ_2	T_2	Re_δ
1.50	4.09	4.99	0.053	426.55	9.12e+04
1.75	4.09	10.33	0.053	426.55	1.01e+05
2.00	4.09	18.56	0.053	426.55	1.16e+05
2.25	4.09	30.63	0.053	426.55	1.28e+05

Fig. 7.6a gives a comparison of the pressure rise with the inviscid pressure jump indicated by a dotted line for different lengths of first ramp. As the first ramp length L1 increases the required second ramp angle also increases, as given in Table 7.6. Accordingly, the pressure rise across the shock also increases. For the first case, the pressure rise occurs very near to the corner indicating no flow separation. For the other two cases (L1 = 1.75 and 2.00 m), the pressure rise occurs upstream of the corner, indicating the presence of flow separation. For the L1 = 2.25 case, the pressure rise is seen much upstream of

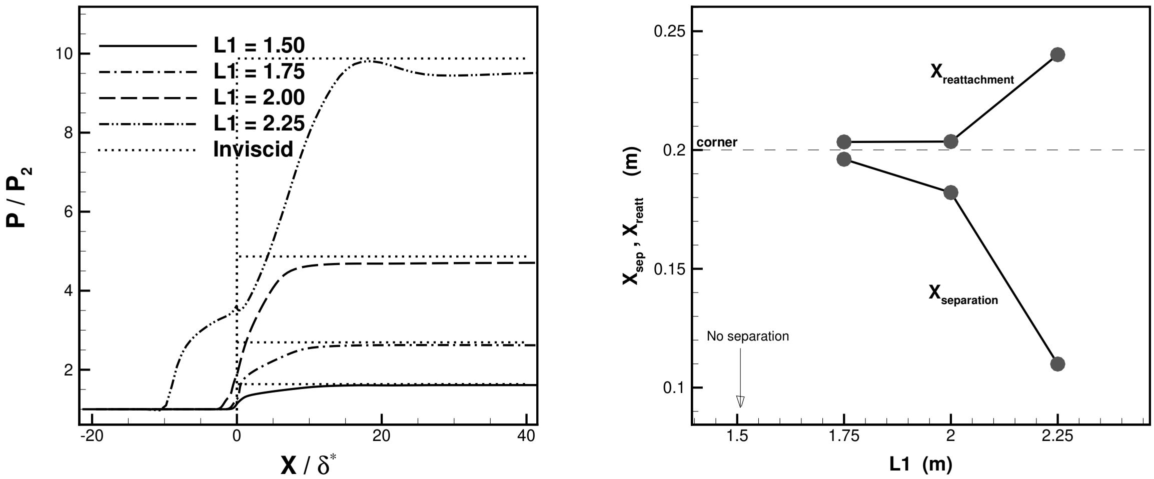

(a)

(b)

FIGURE 7.6: (a) wall-pressure distribution and (b) changes in location of separation and reattachment points from the corner for different lengths of first ramp.

corner indicating a larger separation bubble as the second ramp angle θ_2 is high for this case. From Fig. 7.6b it is seen that as the first ramp length increases, the separation and reattachment points move away from each other, thus increasing the separation bubble size. However, for the first case (L1 = 1.50) the flow does not separate, and hence, there is no separation or reattachment points.

The observed variation in separation length with different first ramp lengths L1 can be justified based on the study of canonical parameters discussed in the previous chapter. Increase in ramp length is the cumulative effect of changes in ramp angle and Reynolds number Re_δ. From the study of the canonical parameters affecting flow separation, it is known that as the ramp angle or the Reynolds number Re_δ increases, the size of the separation bubble increases, for both cases. Based on this, the size of the separation bubble is expected to increases with an increase in first ramp length L1, and observed results are consistent with it.

Since the effect of varying first ramp length is equivalent to increasing the ramp angle, the scaling parameter for this flight parameter is the shock-strength P_3/P_2. As seen in Table 7.6, the shock-strength increases with an increase in first ramp length, and thus, separation length is found to scale with it. Since the wall-temperature and outer flow parameters remain the same, the wall-to-recovery-temperature ratio T_w/T_r does not change with the first ramp length. This shows the product of ratios $\left(\dfrac{T_w}{T_r}\dfrac{P_3}{P_2}\right)$ is the scaling parameter for changes in separation length for different first ramp lengths.

TABLE 7.6: Changes in scaling parameter for different lengths of first ramp.

L1 (m)	θ_2	T_w/T_r	P_3/P_2	$\left(\frac{T_w}{T_r}\frac{P_3}{P_2}\right)$	$\frac{L_{sep}}{\delta^\star}$
1.50	4.99	1.00	1.63	1.63	0.00
1.75	10.33	1.00	2.62	2.62	0.74
2.00	18.56	1.00	4.88	4.88	2.04
2.25	30.63	1.00	9.88	9.88	12.14

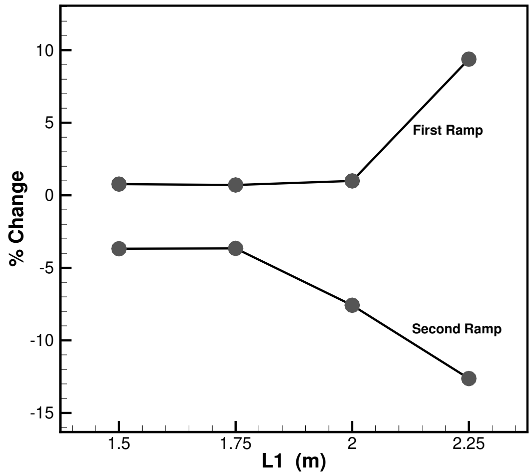

FIGURE 7.7: Percentage change in lift or drag forces acting on the two ramps for different lengths of first ramp.

As the first ramp length (L1) is increased, the size of separation length increases and hence the percentage difference in the computed lift and drag forces is always higher than the inviscid solution, over the first ramp. For the first two cases, there is no/negligible flow separation, and hence, the difference is small or insignificant whereas, for the other two cases, flow is separated, and accordingly, the percentage difference increases. Over the second ramp, for the first two cases, there is no/negligible flow separation, but the pressure jump is lower than the inviscid solution, and hence, the negative percentage difference is observed. For the remaining two cases, as the ramp length increases, the size of the separation bubble increases, and the difference in inviscid and computed pressure jump also increases. This deviation leads to a decrease in computed lift and drag force, which is lower than the inviscid values, and hence, the negative percentage difference increases. Thus, over the first ramp, the percentage difference can be as high as 10% whereas that over the second ramp, the percentage difference is within 15% for the largest ramp length case.

7.4 Effect of angle of attack

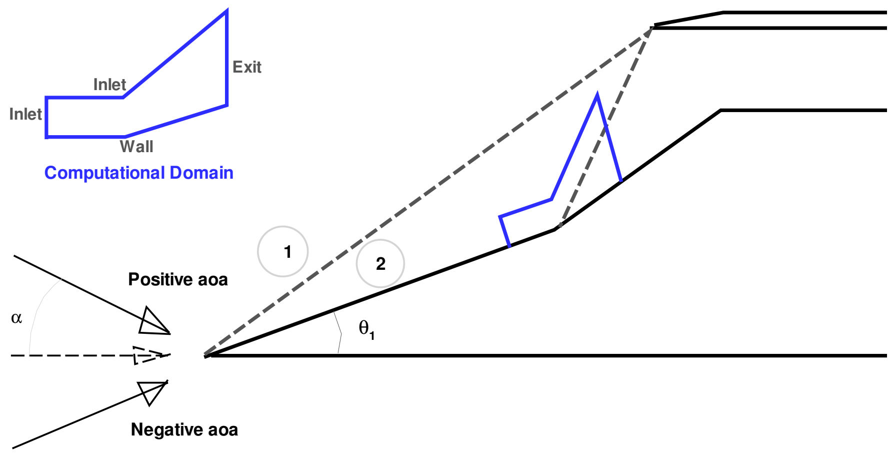

FIGURE 7.8: Schematic of scramjet intake subjected to positive (up), negative (down) and zero (dotted arrow) angles of attacks.

Fig. 7.8 shows the schematic of scramjet subjected to different angles of attack α. As the angle of attack increases (positive angle of attack), the apparent first ramp angle ($\theta_1^\star = \theta + \alpha$) increases and hence the Mach number M_2 at station-2 decreases and the shock angle β_1 increases as given in Table 7.7. For zero angle of attack (shown as a dotted arrow), the shocks would meet exactly at the cowl-tip. For the negative angle of attack, the shocks would hit the cowl at downstream of its tip and vice-versa. The apparent ramp angle here refers to actual obstruction (deflection angle) faced by the incoming free-stream flow with changes in angle of attack.

TABLE 7.7: Conditions at station-1 (free-stream) and station-2 for different angles of attack.

M_1	θ_1	α	$\theta_1^\star$	β_1	M_2	ρ_2	T_2
6	14.17	+4	18.18	26.17	3.59	0.063	517.90
6	14.17	+2	16.18	23.94	3.84	0.058	469.96
6	14.17	0	14.18	21.80	4.09	0.053	426.35
6	14.17	-2	12.18	19.73	4.35	0.048	387.11
6	14.17	-4	10.18	17.75	4.62	0.043	352.12

At the angle of attack increases, pressure, temperature, density, and Mach number across the shock are changing, so the effect of angle of attack is the combined effect of changes in Mach number and flow-variables (P, ρ and T) at station-2. Simulations of compression ramp were done to study the effect of angle of attack using conditions as given in Table 7.8 and keeping the wall temperature equal to 1300 K. The methodology followed is discussed in detail in section 7.1. First, the first ramp was simulated using conditions at station-2 for a different angle of attacks, and the boundary layer profile was extracted at the required location. The displacement boundary layer thickness of the boundary layer profiles were 0.01183, 0.01130, 0.01078, 0.01030 and 0.009832 m for -4, -2, 0, +2, and +4 values of angle of attack, respectively. This extracted boundary layer profile was used as an inlet to the computational domain for the different compression ramp simulations to study the effect of angle of attack. The wall-temperature was kept at 1300 K for all the simulations.

TABLE 7.8: Conditions to be used for ramp simulations to study effect of angle of attack.

α	M_2	θ_2	ρ_2	T_2
+4	3.59	18.56	0.063	517.97
+2	3.84	18.56	0.058	469.96
0	4.09	18.56	0.053	426.35
-2	4.35	18.56	0.048	387.11
-4	4.62	18.56	0.043	352.12

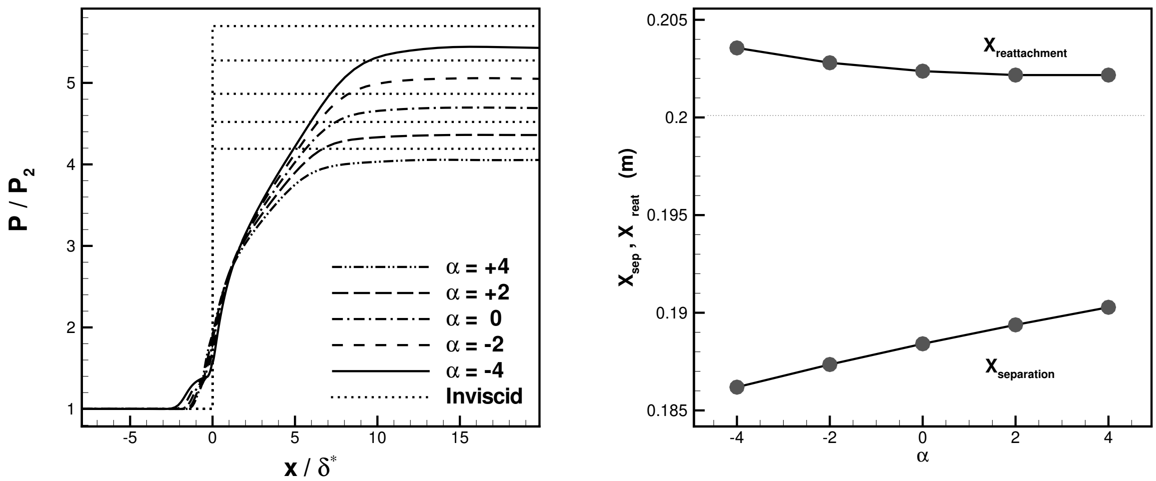

(a) (b)

FIGURE 7.9: Variation in (a) wall-pressure distribution and (b) movement of separation and re-attachment points from corner for different angles of attack.

Fig. 7.9a shows the wall-pressure distribution over the two ramps for different angles of attack. The computed wall-pressure distribution is compared with the inviscid solution, shown by a dotted line, and it is seen that the CFD computed values are always lower than the inviscid solution. With an increase in the angle of attack, the shock-strength decreases, and this leads to decrease in the pressure jump across the shock. The upstream influence is found to decrease with an increase in the angle of attack, which means the separation length is decreasing. From Fig. 7.9b, it is seen that as the angle of attack increases, the separation and reattachment point move closer towards the corner leading to a decrease in separation length.

The effect of angle of attack on separation length is the cumulative effect of changes in the Mach number and flow-properties (P, ρ, and T) at station-2. As shown in Table 7.8, with an increase in the angle of attack, the Mach number decreases (which should lead to an increase in separation length) and the flow-properties (P, ρ, and T) increases (which should lead to decrease in separation length). As per the results, the separation length decreases with an increase in the angle of attack and this probably implies that effect of flow-properties (P, ρ, and T) is dominant as compared to that of Mach number.

TABLE 7.9: Changes in scaling parameter different angles of attack.

α	$\frac{T_w}{T_r}$	$\frac{P_3}{P_2}$	$\left(\frac{T_w}{T_r}\frac{P_3}{P_2}\right)$	$\frac{L_{sep}}{\delta^\star}$
-4	0.768	4.19	4.37	1.46
-2	0.766	4.52	4.04	1.36
0	0.764	4.88	3.73	1.29
+2	0.762	5.27	3.44	1.24
+4	0.760	5.69	3.18	1.20

The trend in separation length changes is analyzed with the two ratios, T_w/T_r and P_3/P_2, see Table 7.9. As the angle of attack increases, the Mach number at station-2 decreases, which implies a decrease in shock-strength P_3/P_2 and in increase in separation length. However, the separation length is found to decrease with an increase in the angle of attack. With respect to the ratio T_w/T_r, as the angle of attack increases, the ratio T_w/T_r decreases and separation length also decreases. This shows the wall-to-recovery-temperature ratio T_w/T_r is dominant as compared to the shock-strength P_3/P_2, as discussed in the analysis based on the canonical study. Thus, both scaling parameters should be taken into account to include the effect of changes in Mach number and the flow-properties for different angles of attack. The changes in separation length are found to scale with the product of these two scaling parameters, $(T_w/T_r).(P_3/P_2)$, for different angles of attack, as shown in Table 7.9.

Fig. 7.10 shows the percentage difference (between the inviscid solution and the CFD computed values) for lift or drag forces acting on the first ramp and second ramp for different angles of attack. For the first ramp, the size of separation bubble decreases with increase in the angle of attack (from +2 to +4) and hence the percentage difference between the computed and the inviscid drag decreases. As the angle of attack decreases (for -2 to -4), the size of separation bubble increases and hence the percentage difference

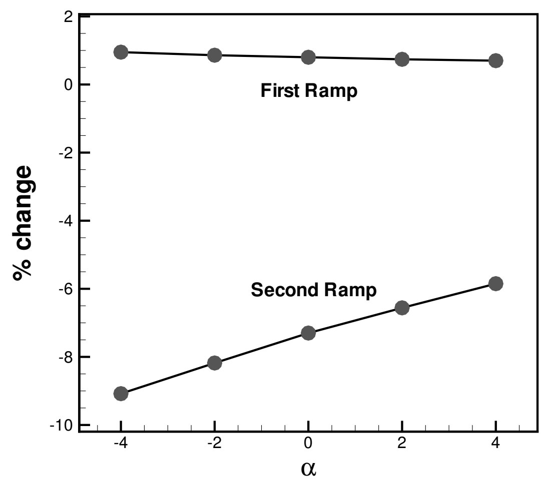

FIGURE 7.10: Percentage change in lift or drag forces acting on the two ramps for different angles of attack.

between the computed and analytical value increases. However, the percentage difference, between the inviscid solution and CFD computed lift and drag forces acting over the first ramp, is small and is within 1% range. Over the second ramp, this percentage difference ranges between 5 to 10%. This comparatively high percentage difference over the second ramp is due to the combined effect of the separation bubble as well as the separation shock. Due to this, the computed pressure jumps are much lower than the inviscid solution, especially at higher Mach numbers.

7.5 Effect of altitude

As the altitude changes, the properties of air - pressure, temperature, density - are the only parameters that get varied. The altitude is varied from 26 km to 34 km in steps of two, and the properties of air at each of these altitudes [71] is shown in Table 7.10. The pressure and density decrease with increase in altitude whereas the temperature has on opposite trend.

The properties of air downstream the shock at station-2 are shown in Table 7.11;computed keeping the first ramp angle, and free-stream Mach number constant. The methodology followed is discussed in detail in section 7.1.. The displacement boundary layer thickness of the extracted boundary layer profiles are 0.00977, 0.01025, 0.01081, 0.01127 and 0.01179 m for 26, 28, 30, 32, and 34 km altitude, respectively. Simulations of compression ramp were done to study the effect of cruise altitude using conditions as given in Table 7.11 keeping the wall temperature equal to 1700 K.

TABLE 7.10: The properties of air - pressure, temperature, density - at different altitudes in atmosphere.

z (km)	M_1	P_1	ρ_1	T_1
26	6	2188.00	0.034	222.50
28	6	1616.00	0.025	224.50
30	6	1171.90	0.018	226.65
32	6	889.00	0.013	228.50
34	6	663.40	0.009	233.70

TABLE 7.11: The changes in conditions at station-2 with increase in altitide.

z (km)	M_2	P_2	ρ_2	T_2
26	4.09	12311.00	0.102	418.74
28	4.09	9092.30	0.074	422.51
30	4.09	6592.20	0.053	426.55
32	4.09	5001.90	0.040	430.03
34	4.09	3732.60	0.029	439.82

Fig. 7.11a shows the wall-pressure distribution for different altitudes. Since the Mach number is kept constant for all cases, the shock-strength remains the same, and hence the pressure jump also remains the same for all altitudes. The upstream influence is found to increase with an increase in altitude indicating an increase in separation length. Fig. 7.11b shows the skin-friction distribution over the two ramps near the corner for different altitudes. The separation length normalized the respective incoming displacement boundary layer thickness is shown in Fig. 7.11c, and as seen, it increases with an increase in altitude.

As the altitude increases, the pressure and density decreases, whereas the temperature increases in the given altitude range. So the observed trend in separation length is due to the cumulative effect of these two contradictory changes - (i) decrease in pressure and density (which should lead to an increase in separation length) and (ii) increase in temperature (which should lead to decrease in separation length). As per the results, the separation length is found to increase with altitude, and this shows that the effect of the decrease in pressure and density is more dominant as compared to that of the increase in temperature.

Since only the altitude is changing, the shock-strength remains the same, and thus, the ratio P_3/P_2 does not change with the changes in altitude. The ratio $\frac{T_w}{T_r}$ decreases with increase in altitude, as shown in Table 7.12. The wall-to-recovery-temperature ratio T_w/T_r, which has scaled with the separation length for all the flight parameters studied till now, fails to be the scaling parameter with changes in altitude.

The ratio $\left(\frac{T_w}{T_r}\frac{P_3}{P_2}\right)$ fails to be a scaling parameter for changes in separation length

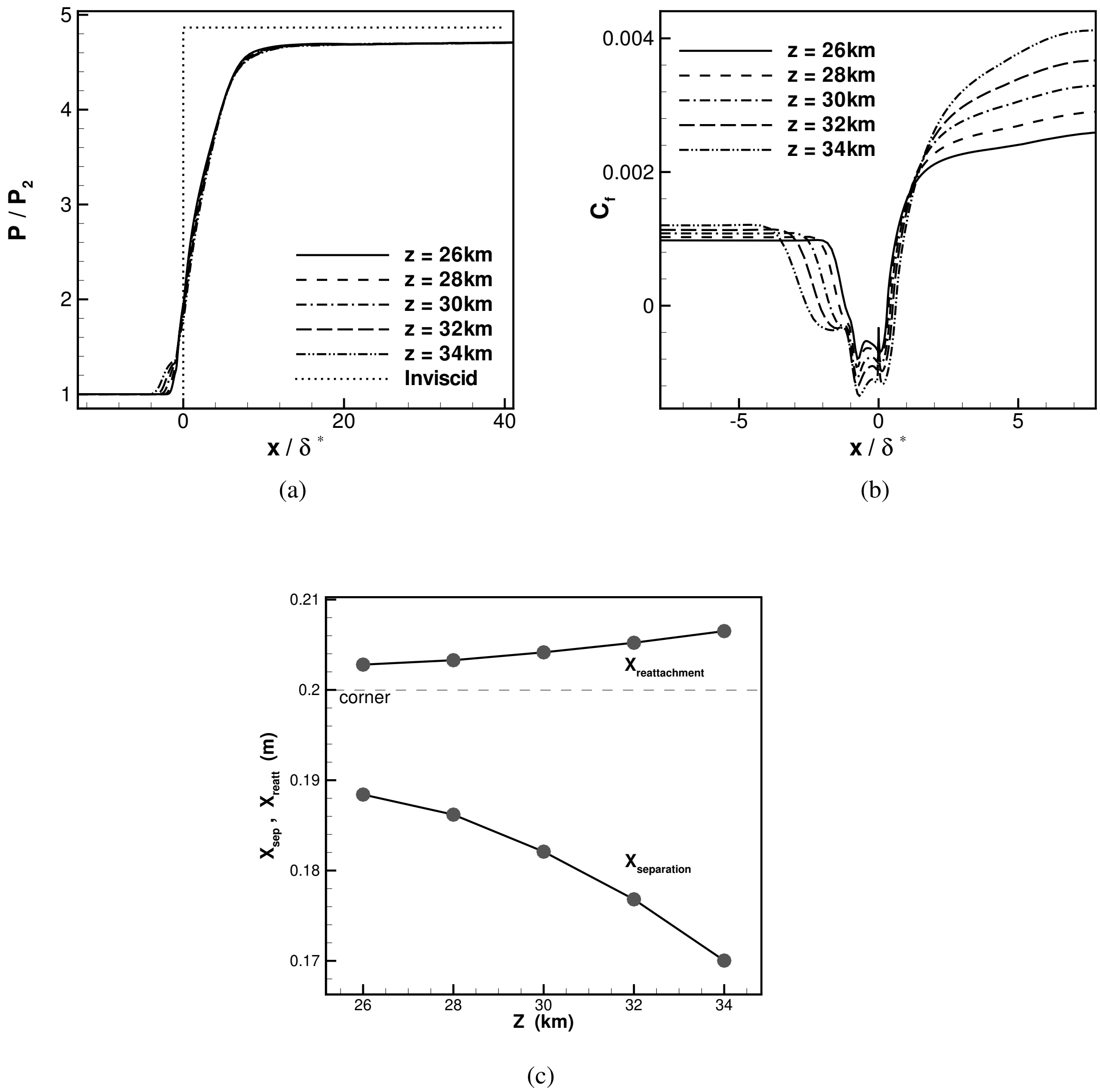

FIGURE 7.11: Variation in (a) wall-pressure distribution, (b) skin-friction distribution, and (c) normalized separation length for different altitudes.

TABLE 7.12: Variation in scaling parameter with altitude.

z (km)	$\dfrac{T_w}{T_r}$	$\dfrac{P_3}{P_2}$	$\left(\dfrac{T_w}{T_r}\,\dfrac{P_3}{P_2}\right)$	$\dfrac{L_{sep}}{\delta^\star}$
26	1.018	4.88	4.97	1.47
28	1.009	4.88	4.92	1.66
30	0.999	4.88	4.87	2.04
32	0.991	4.88	4.84	2.52
34	0.969	4.88	4.73	3.09

with altitude. The factor P_3/P_2 takes into account the effect of shock-strength and the factor T_w/T_r takes into account the effect of the wall-temperature, Mach number and temperature. However, it does not take into account the effect of upstream pressure and density. Since the changes in pressure and density are opposite to that of temperature, only the temperature can not take into account the effect of flow-properties on separation length. From the boundary layer analysis of all the flight parameters, it is seen that the near-wall density is an important parameter as the separation length has scaled with it for all the flight parameters considered in this work. This shows there is a need to modify the above existing scaling parameter $\left(\frac{T_w}{T_r}\frac{P_3}{P_2}\right)$ such that it takes into account the effect of upstream density as well as upstream pressure along with the other parameters.

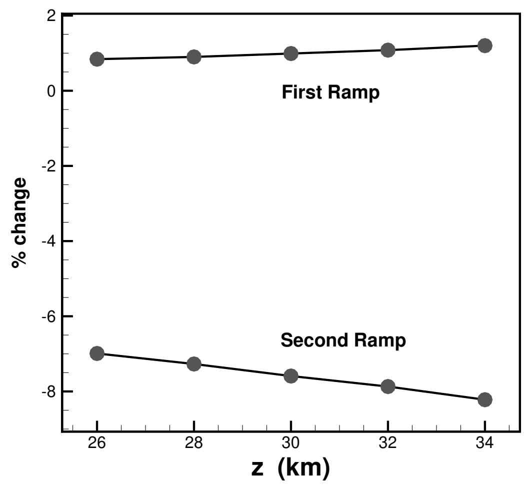

FIGURE 7.12: Percentage change in lift or drag forces acting on the two ramps for different altitudes.

Fig. 7.12 shows the percentage difference between the inviscid and the computed values of lift and drag forces acting over the first ramp and second ramp for different altitudes. As the altitude increases, the separation length increases, and hence, the percentage difference in the computed lift and drag forces over the two ramp increases (for the second ramp, the increase is in absolute values). Over the first ramp, the percentage difference in lift and drag force continuously increases, and this percentage difference is positive (indicating CFD computed lift and drag are higher than the inviscid solution) and within 2% range. While over the second ramp, the computed values are less than the inviscid, and this percentage difference increases with an increase in altitude, and it ranges approximately from 6 to 8% for the range of altitudes considered.

7.6 Overall analysis of scaling parameter

The changes in separation length are directly related to boundary layer thickness (δ or $\delta^{\star}$) and the wall-temperature T_w. It is inversely related to Mach number M_2 and flow-properties - pressure P_2, temperature $T2$, and density ρ_2 (appendix D). Further, the separation length is found to increase with an increase in shock-strength P_3/P_2 due to changes in the ramp/deflection angle. Thus, the separation length is related to different parameters as given below.

$$\frac{L_{sep}}{\delta^{\star}} \quad \propto \quad T_w \left(\frac{1}{M_2}\right) \left(\frac{1}{T_2\, P_2\, \rho_2}\right) \left(\frac{P_3}{P_2}\right) \tag{7.1}$$

The recovery temperature T_r is function of Mach number and temperature, as given in Eq. 7.2.

$$T_r = T_2 \left(1 + \frac{\gamma - 1}{2} M_2^2\right) \tag{7.2}$$

Thus, the wall-to-recovery-temperature-ratio T_w/T_r takes into account the effect of wall-temperature, Mach number and temperature at the edge of boundary layer. Using Eq. 7.2, the Eq. 7.1 can be re-written as

$$\frac{L_{sep}}{\delta^{\star}} \quad \propto \quad \frac{T_w}{T_r}\, \frac{P_3}{P_2} \left[\frac{1}{P,\, \rho}\right] \tag{7.3}$$

The scaling parameter $\left(\frac{T_w}{T_r}\, \frac{P_3}{P_2}\right)$, which is proposed based on the study of canonical parameters (chapter-6) and flight parameters (chapter-7) affecting separation length, takes into account the effect of all the relevant flow parameters except pressure and density. There is need to modify this scaling parameter such that it takes into the effect of density and pressure as well.

In summary, for supersonic flow over a compression ramp, a non-dimensional parameter (S) is proposed for the scaling of the separation length, and is given as,

$$S = \frac{T_w}{T_r}\, \frac{P_d}{P_u} \tag{7.4}$$

where P_d/P_u is shock-strength with P_d and P_u being pressure downstream and upstream of shock, respectively. The ratio T_w/T_r is the wall-to-recovery-temperature ratio where

T_w is the wall-temperature and T_r is the recovery temperature given as,

$$T_r = T_\infty \left(1 + \frac{\gamma - 1}{2} M_\infty^2\right) \tag{7.5}$$

where T_∞ is the free-stream temperature and M_∞ is the free-stream Mach number.

TABLE 7.13: The variation in separation length and the scaling parameter with different flight parameters.

Flight parameters	Separation length: L = $L_{sep}/\delta^\star$	Scaling Parameter: S = $\frac{T_w}{T_r}\frac{P_d}{P_u}$
$M \uparrow$	$L \downarrow$	S $\downarrow$
$L1 \uparrow$	$L \uparrow$	S $\uparrow$
$\alpha \uparrow$	$L \downarrow$	S $\downarrow$
$z \uparrow$	$L \uparrow$	S $\downarrow$

Table 7.13 shows the variation in scaling parameter S and the separation length with different flight parameters. It has scaled with the separation length for all the flight parameters studied except the cruise altitude. As the altitude changes, all the three flow-properties - pressure, temperature and density - are changing, and further, the changes in pressure and density is opposite to that in temperature. However, the scaling parameter S takes into account the effect of temperature only; effect of pressure and/or density is not considered. Hence, it fails to scale with separation length with changes in altitude. Based on the study of changes in separation length with different flight parameters, the non-dimensional parameter S = $\left(\frac{T_w}{T_r}\frac{P_d}{P_u}\right)$ is found to be potential scaling parameter for separation length studies.

7.7 Summary

From the study of the flight parameters affecting flow-separation, it is found that (i) as the altitude increases, the size of the normalized separation length increases, (ii) as the flight Mach number increases, the normalized separation length increases, (iii) as the first ramp length is increased, the normalized separation length increases, and (iv) as the angle of attack increases, the normalized separation length decreases. The trend in separation length changes, with different flight parameters, is justified by analyzing the results with (i) boundary layer analysis, (ii) conclusions drawn from the canonical study, and (iii) scaling parameter analysis. Effect of the separation bubble on the intake generated lift and is quantified in terms of percentage difference (between inviscid solution and CFD computed pressure forces - lift and drag - acting over the two ramps). It is observed that the difference is maximum for high altitude, high flight Mach number, larger length of the first ramp, and negative angles of attack. The percentage difference, over the second ramp, is higher than that over the first ramp, as both the separation bubble and the separation shock are altering the pressure distribution over the second ramp. Lower flight Mach number looks more critical due to large separation bubble, but its effect is mainly felt on the first ramp. Whereas for higher Mach numbers, both separation bubble and separation shock alter the pressure distribution, which is much higher than that at lower Mach numbers. If variable ramp length is considered, the first ramp length of value L1 = 2.25 m is the worst-case scenario, wherein the percentage difference can be more than 12%.

Chapter 8

Conclusions

8.1 Conclusions

This thesis studies the effect of shock-induced boundary layer separation in intake of the scramjet engines. A conventional double ramp mixed compression intake is considered, where the on-design condition corresponds to a flight Mach number M = 6 at an altitude of z = 30 km. Off-design conditions are considered by varying the flight parameters above and below the design point conditions. The effect of different flight parameters on separation length changes and its effect on the pressure generated lift and drag are discussed in detail, in terms of percentage difference.

The separation bubble predicted depends on the turbulence model used for the closure of unknown terms in Reynolds Averaged Navier-Stokes (RANS) equation. The shock modified k - ε of Sinha et al. [18] has shown good potential in shock dominated flows. However, it is developed for an inviscid scenario where Reynolds number Re $\rightarrow \infty$. The model predictions are extended to finite Reynolds number encountered in realistic flows by adding the turbulent diffusion terms in the governing equations. The effect of the diffusion terms, on the amplification of the turbulent kinetic energy across shock-wave, is studied. It is found the addition of diffusion leads to a reduction in the amplification of turbulent kinetic energy across the shock. The amplification of turbulent variables increases on successive grid refinement. Overall, the diffusion term is found to have a small effect on the turbulence amplification across the shock waves. Thus, the shock-unsteadiness model, originally proposed for an inviscid scenario where $Re \rightarrow \infty$, is extended to realistic flows at finite Reynolds number.

An increase in ramp angle leads to an increase in shock strength leading to an adverse pressure gradient, and hence, the separation length increases. With respect to changes in Mach number, there are two competing effects - pressure gradient and flow kinetic energy - acting on the separation bubble. Both are equally important and should be taken into consideration while studying flow-separation with Mach number. The separation length is found to increase with the increase in Reynolds number Re_δ. However, the normalized separation length is found to decrease with the increase in Re_δ. This contradiction occurs because the increase in separation length is small as compared to the increase in displacement boundary layer thickness $\delta^\star$. Consequently, the separation length, when normalized by displacement boundary layer thickness, decreases with the increase in Reynolds number Re_δ.

The changes in separation length with the flight parameters - flight Mach number, angle of attack, first ramp length and cruise altitude - is justified based on the understanding drawn from the study of canonical parameters affecting flow separation. Based on the analysis of the separation length with different canonical parameters, a non-dimensional parameter S = $\left(\frac{T_w}{T_r}\frac{P_d}{P_u}\right)$ is proposed for the scaling of the separation length. The ratio T_w/T_r is the wall-to-recovery-temperature ratio and P_d/P_u is the pressure jump across the shock. As the flight Mach number increases, the separation length decreases, and the scaling parameter S is also found to reduce. As the angle of attack increases, the separation length decreases, and the scaling parameter is also found to decrease. As the first ramp length is increased, the scaling parameter S increases, and the separation length is also found to increase. Altitude is the only flight parameter where the scaling parameter S fails to scale with the separation length. Deviations in computed forces with the inviscid solution increases with an increase in the separation length. For the range of flight parameters considered, the off-design condition operation of flight Mach number M = 8 is identified to be the worst-case scenario wherein the percentage difference in computed forces (lift or drag) can be as high as 12%, and vehicle stability is comparatively most affected at this condition.

8.2 Contributions

- The shock-unsteadiness turbulence model has shown potential in predicting shock-induced flow separation accurately. It is applied to scramjet intake geometry to study the effect of flow separation on the pressure generated lift and drag forces.

- Both on-design and off-design flight conditions are considered to identify the worst-case scenario, with the largest separation bubble at the junction of the intake ramps. It occurs at a flight Mach number of M = 8. The percentage difference in computed forces (lift or drag) can reach high up to 12%, and the vehicle stability would be worst affected at such condition.

- The shock-unsteadiness model was developed on the basis of an inviscid framework, representative of infinite Reynolds number. Its performance at finite Reynolds number, characteristics of realistic flight conditions, is tested by including the effect of diffusion terms in the governing equations. It is found that the diffusion terms have a small effect and it decreases further with grid refinement.

- The variation of separation length with canonical parameters is used to study the underlying physical trends. In particular, variation of Mach number is accompanied by two competing effects - increase in the adverse pressure gradient and increase in the flow kinetic energy. Both the effects should be considered in separation length analysis with respect to Mach number.

- The separation length is found to increase with an increase in Reynolds number, and it shows an opposite trend when normalized with an incoming displacement boundary layer thickness. Detailed analysis carried out shows the changes in separation length is very small as compared to that in displacement boundary layer thickness, and hence the trend reversal occurs.

- The scaling parameter $S = \left(\frac{T_w}{T_r}\frac{P_d}{P_u}\right)$ is proposed for separation length analysis for varying flight parameters. Changes in separation length with Mach number, angle of attack and first ramp length have scaled with this scaling parameter. Thus, the scaling parameter S is found to be the potential non-dimensional parameter for separation length studies.

8.3 Future work

The effect of leading-edge radius, which leads to the formation of a bow shock, on the separation length can be analyzed to the include the effect of the leading-edge radius in the scaling parameter. The effect of the interaction of second ramp shock with the first ramp shock or with the expansion fan at the shoulder of the second ramp, on the separation length, can be analyzed. The corner between the two ramps is sharp. However, it can be made curved by applying a sweep radius. The future work can involve studying the effect of sweep radius on the separation length with a possibility of including it in the scaling parameter. For the altitude range (26 to 34 km) considered in the above study, the pressure and density are decreasing, whereas the temperature is increasing. An alternate altitude range can be examined, where all three flow-properties (pressure, temperature, and density) are reducing, to check whether the proposed scaling parameter scales with separation length in this altitude range. The present simulations were performed for supersonic flow over a 2D compression corner geometry. Simulations can be performed for 3D geometries (cone-flare, cylinder-flare, or 3D compression ramp) where the separation bubble will be three dimensional.

ANSWER TO REVIEWER-1 COMMENTS

1. **The authors have listed some literature relating to DNS/LES of shock-turbulence interaction in chapters 5 and 6. In my opinion, these and other relevant literature on DNS and LES should appear in the introduction of the background chapter. Since, the shock-turbulence interaction problems are routinely dealt with using LES, the author may discuss the limitation of LES and utility of RANS in this context.**

   Response: The literature relating to DNS/LES of shock-turbulence interaction and shock boundary layer interactions is moved to a separate chapter titled 'Literature Review' in the updated thesis (chapter-3 on page-25). The problem of shock-turbulence interaction is considered as a model problem for improvement in RANS turbulence model. The simulations presented in this work are based on the RANS turbulence model. The proposed improvements apply to the RANS turbulence model, and hence RANS simulations were performed. LES simulations would be helpful in understanding the physics or validating the performance of RANS turbulence models. Further, LES has two main limitations (i) LES simulations are too expensive computationally to perform practical engineering simulations on a routine basis and (ii) LES has not yet reached the level of maturity that users, without significant experience and knowledge, can obtain the level of solution fidelity that can be expected from LES.

2. **In chapter 3, the discussion on turbulence modelling is limited to just k-epsilon model. Here a brief mention of Reynolds stress models would be welcome.**

   Response : A brief discussion regarding the Reynolds stress turbulence models and eddy viscous turbulence models are added to the updated thesis (page-46, section 4.3, second paragraph).

3. **The thermal wall boundary condition should be clearly specified in chapter 5 and 6.**

   Response : The thermal wall boundary conditions are added to the writeup in the revised thesis. The above details are added on page-82, line-7 for ramp angle, page-88, line-11 for Mach number and page-91, fourth line from the bottom for Reynolds number case in chapter-6. In the chapter on the effect of flight parameters (chapter-7), the above details are added at page-100, second last line from the bottom for flight Mach number, page-105, line-15 for Ramp length, page-108, second last line for an angle of attack and page-111, last line for altitude case.

4. **Section 3.1.6: The sentence 'The first variable determines the energy in turbulence...' needs to be modified.**

   Response: The above sentence is modified in the updated thesis (page-47, line-9).

5. **Section 4.1.5: 'shear stress' instead of 'sheer-stress'** [Correction/Addition]

   Response: The above spelling mistake is corrected in the updated thesis. Due to re-arrangement of a few sections, the above is discussed in section-2.5 on page-20 in the updated thesis.

6. **The discussion regarding eddy viscosity is wrong and needs to be modified.**

   Response: The discussion regarding the eddy viscosity is corrected in the updated thesis. The write-up is modified, and relevant references are added (page-20, last paragraph).

7. **Turbulence Reynolds number maybe defined using urms. Please provide a reference for this definition**

   Response : In the updated thesis, the turbulence Reynolds number is now defined in terms of the turbulent variables k and ε (rather than in terms of u_{rms}), and the reference is added for the above definition (page-21, first paragraph).

8. **The simulations presented in Chapters 5 and 6 are two-dimensional - assuming the mean flow in the third direction is zero. The author may comment on the effect of side walls in this context and what may be then be the limitations of the present study.**

Response : In the presence of side-walls (with finite span-wise direction), the flow-field would be close to that in fin induced shock boundary layer interactions. Fig. 8.1 shows Mach 2 fin generated shock wave boundary layer interactions [72]. The fin in Fig. 8.1 acts as ramp, whereas the flat-plate (in the x-z plane) acts as side-wall. Thus, in the presence of a side wall, the 3D compression ramp geometry would resemble the fin induced shock boundary layer interaction. The shock would split and take a lambda structure near the wall [72], as shown in Fig. 8.1. The flow-field would become complex due to three-dimensional nature of the separation bubble with varying size and shape.

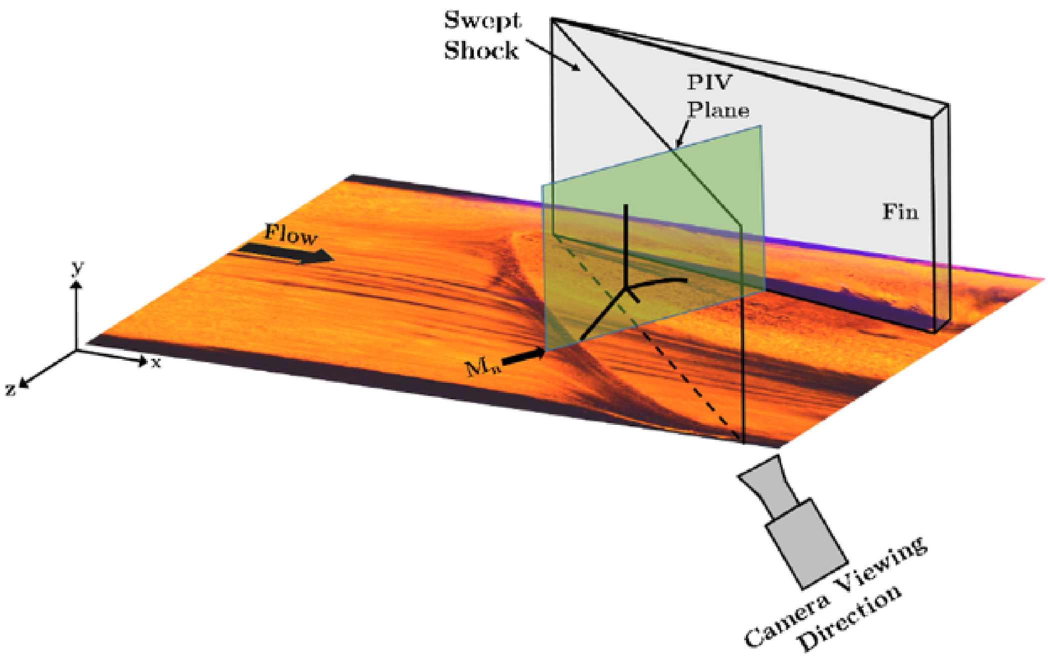

FIGURE 8.1: Schematic of PIV setup for fin induced shock wave boundary layer interaction [72].

Appendix A

Averaging

In turbulent flows, the instantaneous flow variables fluctuate and are a random function of space and time. Hence instantaneous flow variables are decomposed into their mean and fluctuating component.

A.1 Reynolds averaging

In Reynolds averaging [21], which is based on time-averaging, the instantaneous flow quantities are decomposed into the mean and the fluctuating component. The mean components are shown by bar on top ($\bar{x}$) and are addressed as Reynolds averaged quantity. The fluctuating components are shown by a prime (x') and are addressed as Reynolds fluctuation respectively.

$$\phi(x,t) = \bar{\phi}(x,t) + \phi'(x,t) \tag{A.1}$$

The time averaged mean part is expressed as [21]

$$\bar{\phi}(x,t) = \frac{1}{T} \lim_{T \to \infty} \int_{t}^{T+t} \phi(x,t) dt \tag{A.2}$$

where T is long enough time to average out the fluctuations in ϕ. Thus the flow variable can be expressed in terms of the Reynolds-averaged variable and the fluctuating variable as following:

$$\begin{aligned} \rho(x,t) &= \bar{\rho}(x,t) + \rho'(x,t) \\ p(x,t) &= \bar{p}(x,t) + p'(x,t) \end{aligned} \tag{A.3}$$

Reynolds averaging is used in incompressible as well as compressible flows. However, for highly compressible flows and hypersonic flows, it is necessary to perform complex Favre-averaging.

A.2 Favre averaging

In Favre averaging [21], which is based on the density-weighted time averaging, the instantaneous flow quantities are replaced by their mean (shown by tilde on top, e.g., $\tilde{x}$) and the fluctuating components (indicated by double prime, e.g. x'') and addressed as Favre averaged quantities and Favre fluctuations respectively.

$$\phi(x,t) = \tilde{\phi}(x,t) + \phi''(x,t) \tag{A.4}$$

The density-weighted time averaged mean part is expressed as [21]

$$\tilde{\phi}(x,t) = \frac{1}{\bar{\rho}} \lim_{T\to\infty} \int_t^{T+t} \rho(x,t)\phi(x,t)dt \tag{A.5}$$

where the $\bar{\rho}$ is the Reynolds averaged density and $\tilde{\phi}(x,t)$ represents the Favre-averaged quantity. Thus the flow variable can be expressed in terms of the Favre-averaged variable and the flutuating variable as following:

$$\begin{aligned} u(x,t) &= \tilde{u}(x,t) + u''(x,t) \\ T(x,t) &= \tilde{T}(x,t) + T''(x,t) \\ h(x,t) &= \tilde{h}(x,t) + h''(x,t) \\ e(x,t) &= \tilde{e}(x,t) + e''(x,t) \end{aligned} \tag{A.6}$$

Correlations

The time average of the differential of a quantity is given by the differential of the average of the quantity $\overline{\dfrac{\partial \phi}{\partial t}} = \dfrac{\partial \bar{\phi}}{\partial t}$ The time average of the product of the quantity with a constant is given by $\overline{k\phi} = k\overline{\phi}$. The density-weighted average of a Favre fluctuating velocity is zero ($\widetilde{\rho u''} = 0$), but the Reynolds average of a $\overline{u''}$ is not equal to zero. Similarly the Reynolds average of Reynolds fluctuating quantity is zero but is Favre average is not equal to zero. For further details on the correlations used in the averaging, refer to [73]. By substituting the instantaneous variable into the mean and the fluctuating part and using the above relations, the Reynolds-averaged Navier-Stokes equations can be obtained from the instantaneous governing equations.

Appendix B

Jacobian Matrices

The unsplit Jacobians A and Jacobian matrices that are used to construct the split Jacobian are presented in this appendix (from [61]). The unsplit Jacobian A is given by

$$A = \begin{bmatrix} 0 & s_x & s_y & 0 \\ \frac{\partial p}{\partial \rho} s_x - uu' & u' + us_x + \frac{\partial p}{\partial \rho u} s_x & us_y + \frac{\partial p}{\partial \rho v} s_x & \frac{\partial p}{\partial E} s_x \\ \frac{\partial p}{\partial \rho} s_y - uu' & us_x + \frac{\partial p}{\partial \rho u} s_y & u' + vs_y + \frac{\partial p}{\partial \rho v} s_y & \frac{\partial p}{\partial E} s_y \\ u' \left(\frac{\partial p}{\partial \rho} - (E+p)/\rho \right) & u' \frac{\partial p}{\partial \rho u} + \frac{(E+p)}{\rho} s_x & u' \frac{\partial p}{\partial \rho v} + \frac{(E+p)}{\rho} s_y & u' \left(1 + \frac{\partial p}{\partial E} \right) \end{bmatrix} \tag{B.1}$$

where

$$\begin{aligned} \frac{\partial p}{\partial \rho} &= (\frac{\gamma}{2}(u^2 + v^2) \\ \frac{\partial p}{\partial \rho u} &= (1-\gamma)u \\ \frac{\partial p}{\partial \rho v} &= (1-\gamma)v \\ \frac{\partial p}{\partial E} &= \gamma - 1 \end{aligned} \tag{B.2}$$

By diagonalization, the unsplit Jacobian A is split into components as given in equation-4.45. The diagonal matrix of eigen values is

$$\Lambda = \begin{bmatrix} u & 0 & 0 & 0 \\ 0 & u+a & 0 & 0 \\ 0 & 0 & u & 0 \\ 0 & 0 & 0 & u-a \end{bmatrix} \tag{B.3}$$

The left and right eigenvector matrices are

$$R = \begin{bmatrix} 1 & \rho & 0 & \rho \\ 0 & as_x & -s_y & -as_x \\ 0 & as_y & s_x & -as_y \\ 0 & \rho a^2 & 0 & \rho a^2 \end{bmatrix} \tag{B.4}$$

$$R^{-1} = \begin{bmatrix} 1 & 0 & 0 & -1/a^2 \\ 0 & s_x/2a & s_y/2a & 1/2\rho a^2 \\ 0 & -s_y & s_x & 0 \\ 0 & -s_x/2a & -s_y/2a & 1/2\rho a^2 \end{bmatrix} \tag{B.5}$$

The transformation matrices between the primitive and conserved variables are given by

$$S = \frac{\partial V}{\partial U} = \begin{bmatrix} 1 & 0 & 0 & 0 \\ -u/\rho & 1/\rho & 0 & 0 \\ -v/\rho & 0 & 1/\rho & 0 \\ \dfrac{\partial p}{\partial \rho} & \dfrac{\partial p}{\partial \rho u} & \dfrac{\partial p}{\partial \rho v} & \dfrac{\partial p}{\partial \rho} \end{bmatrix} \tag{B.6}$$

$$S^{-1} = \frac{\partial U}{\partial V} = \begin{bmatrix} 1 & 0 & 0 & 0 \\ u & \rho & 0 & 0 \\ v & 0 & \rho & 0 \\ (u^2+v^2)/2 & \rho u & \rho v & \dfrac{1}{\gamma - 1} \end{bmatrix} \tag{B.7}$$

Appendix C

Skin-friction Force in Intake

C.1 Introduction

The skin-friction lift or drag is caused due to the force exerted by the fluid over a moving object. The skin-friction force is parallel to surface, whereas the pressure force is normal to the surface. The skin-friction coefficient is given as,

$$c_f = \frac{\tau_w}{\frac{1}{2}\rho_\infty u_\infty^2} \tag{C.1}$$

$$\tau_w = \mu_w \frac{\partial u}{\partial y}\Big|_w \tag{C.2}$$

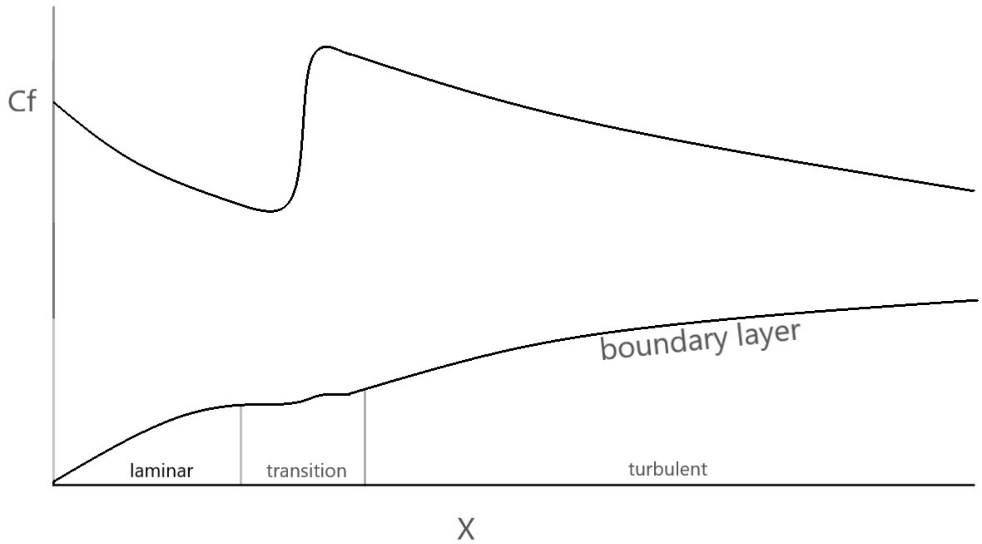

FIGURE C.1: Variation of skin-friction coefficient over the flat plate boundary layer

A schematic showing variation of the skin-friction coefficient over a flat plate boundary layer is shown in Fig. C.1. The force due to the skin-friction is given as

$$F_{cf} = \int_{1}^{n} c_{f,i}\, dx_i \left(\frac{1}{2}\rho_\infty u_\infty^2\right) \tag{C.3}$$

where $c_{f,i}$ is the skin-friction over the elemental length dx_i and F_{cf} is the total integrated force acting due to the skin-friction. The lift and drag due to the skin-friction force is given as

$$F_{cf,x} = F_{cf}\ sin\theta \tag{C.4}$$

$$F_{cf,y} = F_{cf}\ cos\theta \tag{C.5}$$

C.2 Literature

The skin-friction coefficient can be calculated from the CFD results and analytical relations as well. The analytical relation given by Van Driest is most commonly for skin-friction coefficient predictions.

Van Driest Method

The skin-friction coefficient for turbulent boundary layers cannot be predicted analytically as the mechanism of exchange of moment is not uniform. Assuming the shear-stress distribution in the boundary layer is linear and varies with wall distance, Von Karman arrived at relations for recovery factor as a function of laminar and turbulent Prandtl number. Van Driest adapted these relations and arrived at the relationship between Mach number, temperature, Reynolds number, and skin-friction coefficient. It is given as [74]

$$\frac{0.242}{c_f^{1/2}\left(\frac{\gamma-1}{2}M_e^2\right)^{1/2}}(sin^{-1}\alpha + sin^{-1}\beta) = 0.41 + log_{10}(Re_x C_f) - 0.76\ log_{10}\left(\frac{T_w}{T_e}\right) \tag{C.6}$$

where

$$\alpha = \frac{2A^2 - B}{\sqrt{B^2 + 4A^2}} \tag{C.7}$$

$$\beta = \frac{B}{\sqrt{B^2 + 4A^2}} \tag{C.8}$$

$$A = \frac{\frac{1}{2}(\gamma - 1)M_e^2}{T_w/T_e} \tag{C.9}$$

$$B = \frac{1 + \frac{1}{2}(\gamma - 1)M_e^2}{T_w/T_e} - 1 \tag{C.10}$$

$$Re_x = \frac{\rho_e u_e x}{\mu_e} \tag{C.11}$$

where T_w is the wall-temperature and γ is ratio of specific heats. M_e, u_e, ρ_e, and T_e are the Mach number, velocity, density, and temperature at the edge of boundary layer, respectively. Re_x is the Reynolds number at the required location.

Extension to Flows Involving Shocks

The Van Driest method was originally developed for boundary layer flows; thus, it does not take into consideration the effect of shock-wave. However, different modifications were proposed to the original Van Driest method to take into account the effect of shock-waves due to flow deflection (ramp or cone). The Reynolds number for flows involving boundary layers is given as $Re_x = \frac{\rho_e u_e x}{\mu_e}$, and flows involving shock-waves, due to flow deflection, is given by $Re_x = \frac{1}{2}\frac{\rho_e u_e x}{\mu_e}$. Further, skin-friction c_f over the cone/ramp is related to skin-friction over the boundary layer flow with following equation:

$$G = \frac{C_{f,\,cone}}{C_{f,flatplate}} \tag{C.12}$$

where G is the transformation parameter and different researchers have proposed different values, which ranges from 1.08 to 1.20 [75]. In the present analysis, $Re_x = \frac{\rho_e u_e x}{\mu_e}$ is for calculation of skin-friction over the first ramp whereas $Re_x = \frac{1}{2}\frac{\rho_e u_e x}{\mu_e}$ is used for ramp-2 along with the transformation parameter G given in Eq. C.12.

C.3 Predictions

Validation

The skin-friction from the CFD results can be predicted using the Eq. C.1 and C.2. The CFD predicted skin-friction coefficient in turbulent region is always higher than the analytical predictions [75] and this difference is within 20 % depending on the flow conditions. Fig. C.2 shows the comparison the skin-friction coefficient as predicted using the analytical (Van Driest method) with the CFD results over the first ramp. The Reynolds number is taken to be as $Re_x = \frac{\rho_e u_e x}{\mu_e}$ and the results obtained are shown in Fig. C.2. The difference in predicted skin-friction is within the 20% range reported in literature [75]. In computation of skin-friction over the two ramp, the transformation parameter G and the $Re_x = \frac{1}{2} Re_{x,flatplate}$ needs to be taken into account.

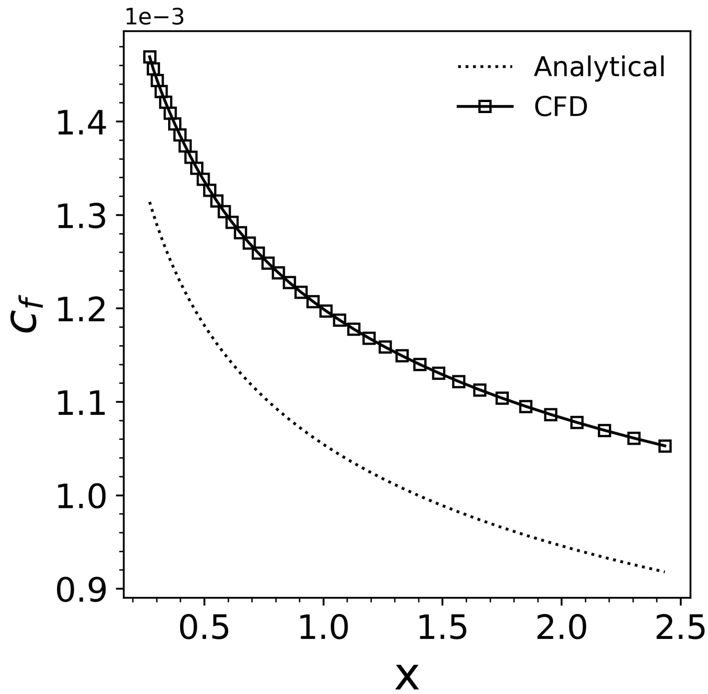

FIGURE C.2: Comparison of analytical (Van Driest) skin-friction with the CFD results over the first ramp.

Contribution of Skin-friction Force

Fig. C.3 shows the contribution of the skin-friction generated force as compared to the total force acting the two ramps under different flight conditions. The contribution of

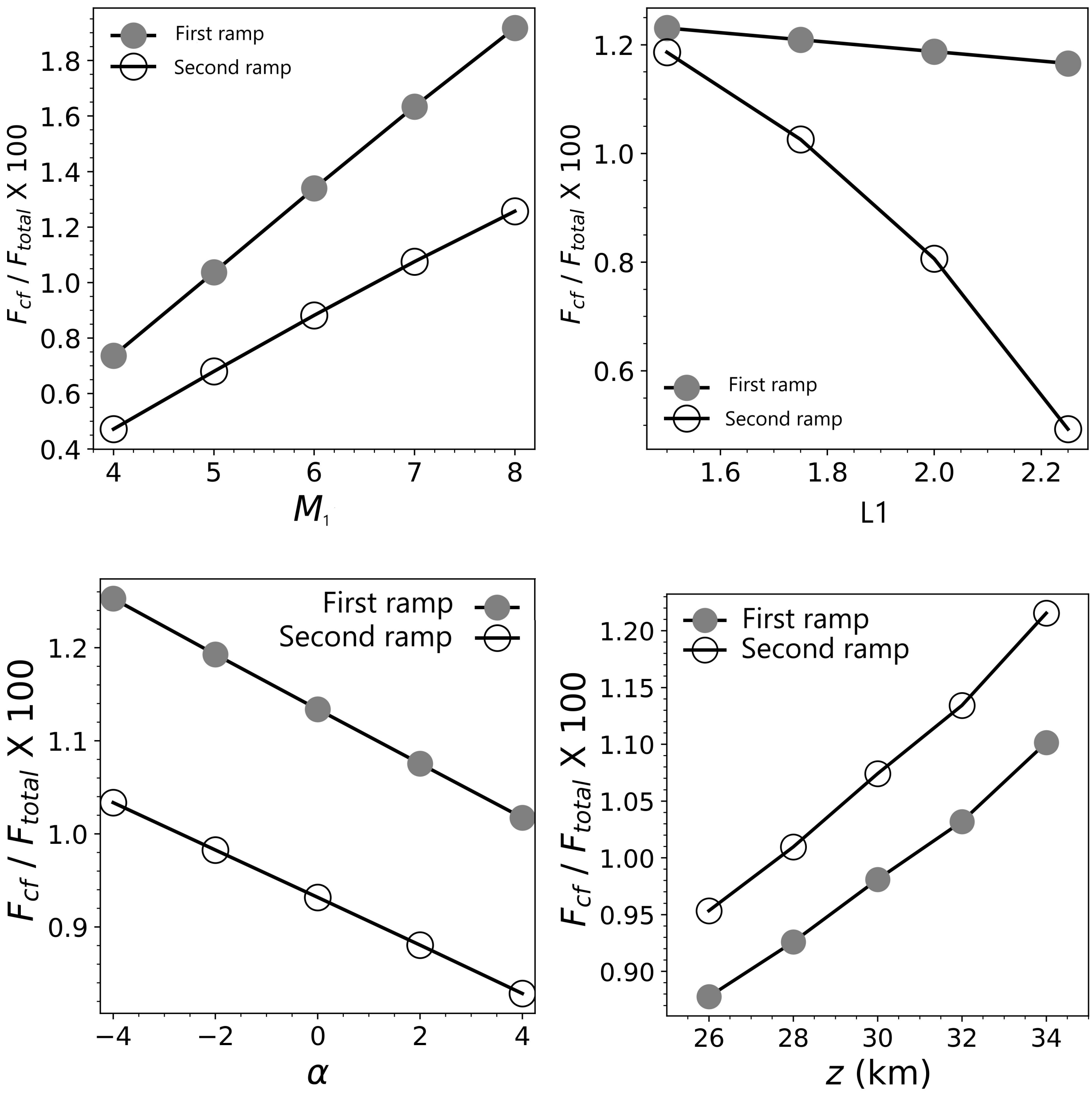

FIGURE C.3: Contribution of skin-friction generated force to the total force acting on the intake over the two ramps under different flight condtions. M_1 - flight Mach number, L1 - first ramp length, α - angle of attack, and z - altitude.

skin-friction generated force is given as

$$F_{cf}\ contribution = \frac{F_{cf}}{F_{cf} + F_P}\ X\ 100 \tag{C.13}$$

where F_{cf} designates the force due to skin-friction coefficient and F_{total} is the total force due to both skin-friction (shear-stress) and pressure. The contribution of skin-friction force calculated using the above equation takes into account only the forces acting due to pressure and skin-friction forces acting over the two ramps of the intake. From Fig. C.3, it is seen that the contribution of skin-friction force acting over the ramps is within 2% range for all the flight parameters. Based on the above, it is conjectured that the pressure generated lift or drag is dominant as compare to that by skin-friction in scramjet intakes. However, the above analysis does not take into consideration the effect of forces acting over the external surface of the intake, where skin-friction might play a major role.

C.4 Summary

Based on the results presented, it is observed that the effect of skin-friction force is minimal as compared to that of pressure force. Of the total forces (pressure and skin-friction) acting on the internal surface of intake over the two ramps, the contribution of skin-friction generated force is about 1 - 2 %. This shows that, at the intake, the pressure generated lift or drag is dominant, and the effect of skin-friction is minimal.

Appendix D

Effect of flow-properties

This appendix shows the effect of flow-properties (Pressure, Temperature, and Density) on the separation length, and is referred in section 6.4 of chapter 6. Supersonic flow over a compression corner geometry (shown in Fig. D.1) is considered for this study. The flow-conditions (Mach number, pressure, density, temperature and wall-temperature) at the free-stream (upstream of the shock boundary layer interaction) are M = 4.097, P = 6592.30 Pa, ρ = 0.05385 kg/m^3, T = 426.55 K and T_w = 400 K.

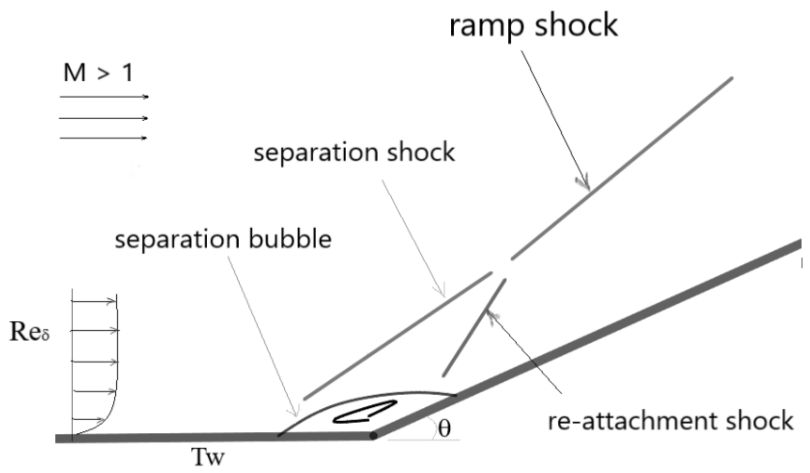

FIGURE D.1: Supersonic flow separtion over a compression corner geometry.

D.1 Effect of temperature

The upstream (free-stream) temperature is varied keeping all other parameters constant to study the effect of temperature on separation length, see schematic in Fig. D.1. The upstream temperature T is varied in the range of 250, 300, 350, 426, and 500 K, to study the effect of free-stream temperature on separation length.

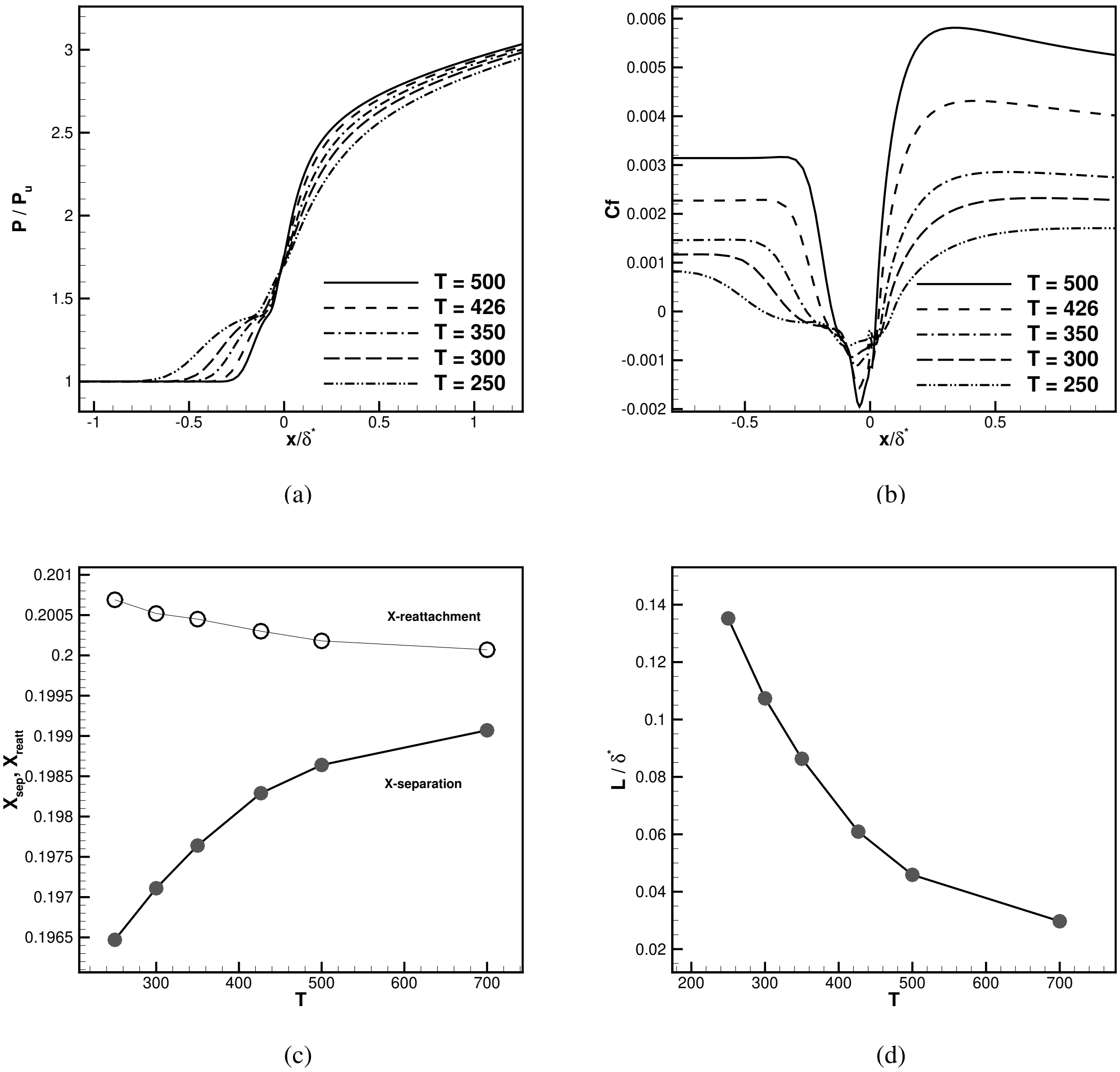

FIGURE D.2: Variation in (a) wall-pressure distribution, (b) skin-friction distribution, (c) movement of separation and re-attachment points from corner, and (d) normalized separation length - for different temperatures.

Fig. D.2 shows the effect of changes in temperature on the separation length. Fig. D.2a shows the wall-pressure distribution over the two ramps for different temperatures. The wall pressure distribution is normalized by the wall pressure upstream of the interaction. As the temperature increases, the upstream influence (distance of pressure rise from corner x = 0) decreases indicating decrease in separation length. Fig. D.2b shows the skin-friction distribution over the surface for different temperatures. It is seen that as the temperature increases, the distance between the separation and reattachment points (location where $c_f = 0$) decreases, which means the separation length is decreasing. Fig. D.2c

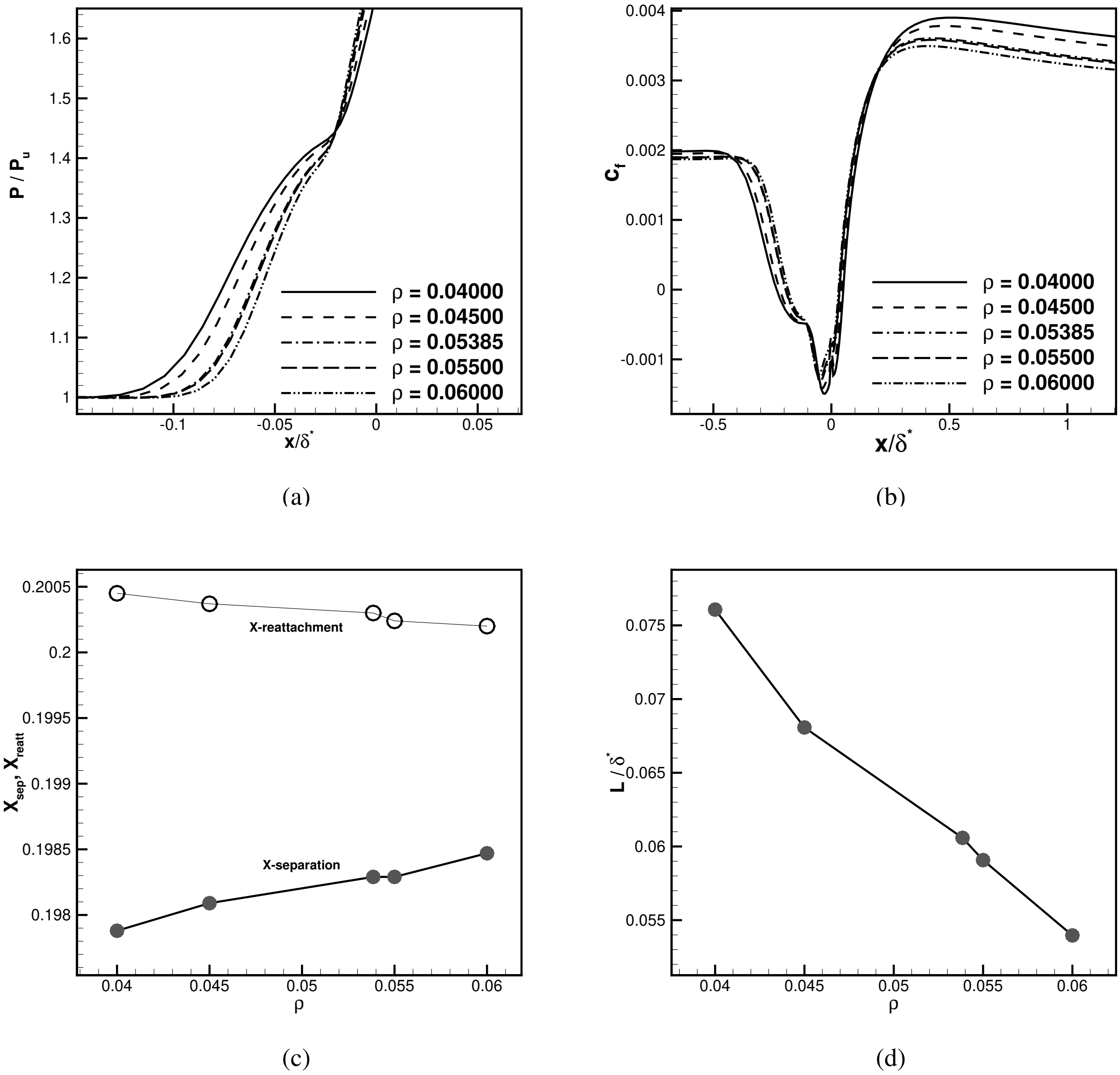

FIGURE D.3: Variation of (a) wall-pressure distribution, (b) skin-friction distribution, (c) movement of separation and re-attachment points from corner, and (d) normalized separation length - for different densities.

shows the movement of the separation and reattachment points with respect to corner for increase in temperature. As the free-stream temperature increases, the separation and reattachment points move closer towards the corner which leads to decrease in separation length. Fig. D.2d shows the variation in normalized separation length with temperature. The normalized separation length decreases with increase in temperature. The results presented here are consistent with that reported in literature [10] [35], [42], [76].

D.2 Effect of density

The free-stream density is varied keeping all other parameters constant to study the effect of temperature on separation length, see schematic in Fig. D.1. The free-stream density ρ_{inf} is varied in the range of 0.40, 0.45, 0.5385, 0.55, and 0.60 kg/m^3, to study the effect of free-stream density on separation length.

Fig. D.3 shows the effect of changes in density on the separation length. Fig. D.2a shows the wall-pressure distribution over the two ramps for different densities. The wall pressure distribution is normalized by the wall pressure upstream of the interaction. As the density increases, the upstream influence (distance of pressure rise from corner x = 0) decreases indicating decrease in separation length. Fig. D.3b shows the skin-friction distribution over the surface for different densities. It is seen that as the density increases, the distance between the separation and reattachment points (location where $c_f = 0$) decreases, which means the separation length is decreasing. Fig. D.3c shows the movement of the separation and reattachment points with respect to corner for increase in density. As the density increases, the separation and reattachment points move closer towards the corner which leads to decrease in separation length. Fig. D.3d shows the variation in normalized separation length with density. The normalized separation length decreases with increase in density. The results presented here are consistent with that reported in literature [42], [76].

D.3 Effect of pressure

Based on the results presented in above sections, it is observed that as the free-stream temperature or density increases the separation length decreases. Since pressure is directly related with density and temperature, with the relation P = ρRT, the pressure will also have same effect on the separation length. Thus the flow-properties (pressure, temperature, and density) are found to have same effect on the separation length, i.e., increase in pressure, temperature or density leads to decrease in separation length.

Appendix E

Analysis of diffusion terms

In this appendix, the analysis of non-conservative diffusion terms is presented. The discretization error for an equation of the form given by

$$\frac{\partial h}{\partial x} = \psi \tag{E.1}$$

in the region of flow discontinuity is discussed. Here h represents the convective flux and ψ is the non-conservative source term, like the production term in the k or ε equation of $k-\varepsilon$ equation. The convective term on the left-hand side is discretized in terms of the fluxes evaluated at the cell interfaces given as below.

$$\frac{\partial h}{\partial x} \simeq \frac{h_{i+1/2} - h_{i-1/2}}{\delta x} \tag{E.2}$$

An upwind method is usually employed to compute the fluxes $h_{i+1/2}$ and $h_{i-1/2}$. Using the Taylor series to expand the RHS gives

$$\left(\frac{\partial h}{\partial x}\right)_i + \frac{1}{3}\frac{\Delta x^2}{8}\left(\frac{\partial^3 h}{\partial x^3}\right)_i + ... \tag{E.3}$$

where the second term is the leading-order truncation error. On integration over the finite-volume cell, leads to

$$\left[h_{i+1/2} - h_{i-1/2}\right] + \frac{\Delta x^2}{24}\left[\left(\frac{\partial^2 h}{\partial x^2}\right)_{i+1/2} - \left(\frac{\partial^2 h}{\partial x^2}\right)_{i-1/2}\right] + ... \tag{E.4}$$

where the integrated error is a function of the derivatives evaluated at the cell interfaces.

The second term ψ involves non-conservative derivative of the shock-normal flow velocity. A symmetric second-order discretization of the velocity derivative yields

$$\psi \simeq -\frac{2}{3}c_0\rho k\left(\frac{u_{i+1} - u_{i-1}}{2\Delta x}\right) \tag{E.5}$$

$$= -\frac{2}{3}c_0\rho k\left[\left(\frac{\partial u}{\partial x}\right)_i + \frac{\Delta x^2}{3}\left(\frac{\partial^3 u}{\partial x^3}\right)_i + ...\right] \tag{E.6}$$

where the Taylor series expansion is used again to identify the leading order error. Integration over the finite-volume cell gives

$$-\frac{2}{3}c_o\int_{x_{i-1/2}}^{x_{i-1/2}}\rho k\frac{\partial u}{\partial x}dx - \frac{2}{3}c_o\frac{\Delta X^2}{3}\int_{x_{i-1/2}}^{x_{i-1/2}}\rho k\frac{\partial^3 u}{\partial x^3}dx - ..... \tag{E.7}$$

Here the first term represents the integrated production of the TKE in the cell, and the second term is the discretization error.

If the solution is continuous, then the derivatives are finite and the magnitude of error decreases monotonically as the grid is refined. This is not true in regions of flow discontinuity. The shock thickness computed using a shock-capturing method decreases with successive grid refinement, such that the derivative

$$\frac{\partial u}{\partial x} \sim \frac{\Delta u}{\Delta x} \sim \frac{\Delta u}{\delta} \tag{E.8}$$

where Δ u is the jump in the flow variable across the shock, Δ x is the grid spacing and δ is the computed shock thickness. The higher order derivative scale as

$$\frac{\partial u^2}{\partial x^2} \sim \frac{\Delta u}{\delta^2} \qquad \textit{and} \qquad \frac{\partial u^3}{\partial x^3} \sim \frac{\Delta u}{\delta^3} \tag{E.9}$$

and therefore unbounded in the limit Δ x $\to 0$.

The total error accrued in the region of shock wave can be estimated when the contributions of all the cells spanning the shock are taken together. Summation of the conservative flux terms for all the cell between $x_u p$ and $x_d n$ gives

$$[h_{dn} - h_{up}] + \frac{\Delta x^2}{24}\left[\left(\frac{\partial^2 h}{\partial x^2}\right)_{dn} - \left(\frac{\partial^2 h}{\partial x^2}\right)_{up}\right] + ... \tag{E.10}$$

where the leading error term involves derivatives evaluated outside the region of discontinuous solution and is therefore small in magnitude. Similarly, the discretized source term [Eq.B7] for all the cells add up to

$$-\frac{2}{3}c_o\int_{x_{dn}}^{x_{up}}\rho k\frac{\partial u}{\partial x}dx - \frac{2}{3}c_o\frac{\Delta X^2}{3}\int_{x_{dn}}^{x_{up}}\rho k\frac{\partial^3 u}{\partial x^3}dx - ..... \tag{E.11}$$

where the non-conservative error term involves higher-order derivatives evaluated in the region of shock wave. The derivatives attain large values, as per Eq.(A8), and the integrated error remains finite as the grid is refined. In some cases (for example strong shock waves), it can be comparable or larger than the production term in magnitude.

The convection terms in non-conservative form of SU modifed k-ε turbulence model can be written in conservative form using the mass conservation equation across the shock wave [66]. The discretization error in the convective terms therefore vanish as the grid is refined. The dissipation term does not include derivative of flow variables, and is therefore well-behaved in the high-gradient region of a shock wave. By comparison, the diffusion terms are non-conservative in nature and can potentially lead to large error at flow discontinuities. In the finite-volume formulation, they are discretized in terms of fluxes computed at the cell faces $i \pm 1/2$

$$\frac{1}{Re}\rho^{-\frac{2}{3}c_0}\left(\frac{h_{i+1/2}-h_{i-1/2}}{\Delta x}\right), \quad \text{where} \quad h = \left(\mu + \frac{\mu_t}{\sigma_k}\right)\frac{\partial k}{\partial x} \tag{E.12}$$

and Δx is the cell size. Taylor series expansion leads to

$$\frac{1}{Re}\rho^{-\frac{2}{3}c_0}\left[\left(\frac{\partial h}{\partial x}\right)_i + \frac{\Delta x^2}{24}\left(\frac{\partial^3 h}{\partial x^3}\right)_i + \mathscr{O}(\Delta x^4)\right], \tag{E.13}$$

where the second term is the leading order truncation error. Consider only the first term in the series and integration by parts leads to,

$$\frac{1}{Re}\int_{i-\frac{1}{2}}^{i+\frac{1}{2}} \rho^{-\frac{2}{3}c_0}\frac{\partial h}{\partial x}dx \quad = \quad \frac{1}{Re}\left[\rho^{-\frac{2}{3}c_0}h\right]_{i-\frac{1}{2}}^{i+\frac{1}{2}} - \frac{1}{Re}\int_{i-\frac{1}{2}}^{i+\frac{1}{2}} -\frac{2}{3}c_0\rho^{-\left(\frac{2}{3}c_0+1\right)}\frac{\partial \rho}{\partial x}h dx \tag{E.14}$$

The integrated effect across the entire shock is thus given by,

$$\frac{1}{Re}\left[\rho^{-\frac{2}{3}c_0}\left(\mu + \frac{\mu_t}{\sigma_k}\right)\frac{\partial k}{\partial x}\right]_{up}^{dn} + \frac{2}{3}\frac{c_0}{Re}\int_{up}^{dn} \rho^{-\left(\frac{2}{3}c_0+1\right)}\frac{\partial \rho}{\partial x}\left(\mu + \frac{\mu_t}{\sigma_k}\right)\frac{\partial k}{\partial x}dx. \tag{E.15}$$

The first term is conservative and its contribution across the shock is small, because of negligible k-gradient at the upstream (up) and downstream (dn) edges of the shock wave. The second term is non-conservative and can be written as

$$\frac{4}{9}\frac{c_0^2}{Re}\int_{up}^{dn} f\left(\frac{1}{\rho}\frac{\partial \rho}{\partial x}\right)^2\left(\mu + \frac{\mu_t}{\sigma_k}\right)dx \tag{E.16}$$

by assuming that $f = k\rho^{-\frac{2}{3}c_0}$ is constant across the shock. This is true for inviscid shock waves [18], and is approximately valid for eddy-viscous shock waves, as per the simulation results presented in the next section.

The magnitude of the different terms is estimated as given below.

$$\left(\frac{1}{\rho}\frac{\partial \rho}{\partial x}\right)^2 \simeq \left[\frac{1}{\rho_{av}}\frac{2(\rho_{av}-1)}{\delta}\right]^2 \sim \frac{1}{\delta^2} \tag{E.17}$$

where ρ_{av} is the average density across the shock and the upstream density is normalized to 1. Also, for highly turbulent flows $\mu + \mu_t/\sigma_k \sim \mu Re_t$, where the fluid viscosity $\mu \propto T^{0.75} \sim M^{1.5}$, as the temperature jump across a normal shock scales as M^2 for high Mach numbers. For normalized $f \simeq 1$ across a shock,

$$\frac{4}{9}\frac{c_0^2}{Re}\int_{up}^{dn} f\left(\frac{1}{\rho}\frac{\partial \rho}{\partial x}\right)^2\left(\mu + \frac{\mu_t}{\sigma_k}\right)dx \quad \sim \quad \frac{1}{\delta}\frac{Re_t}{Re}M^{1.5} \tag{E.18}$$

The non-conservative part of the diffusion term (E.14) is proportional to Re_t, and hence its effect is larger at higher turbulence levels. The effect is inversely proportional to the Reynolds number of the flow and the shock thickness. Its magnitude is higher for stronger shock waves with higher downstream value of the dynamic viscosity μ.

As per (E.18), the non-conservative contribution of the diffusion terms scale as Re_t/Re; typical values of this ratio are 10^{-2} or lower for realistic flows Its effect is expected to increase with grid refinement, as δ decreases. For fine enough grids, the shock thickness is determined by the balance of the diffusion terms and the inertial terms in the governing equations. An equivalent Reynolds number defined in terms of the shock thickness and the sum of molecular and turbulent viscosity is therefore order 1 in magnitude. This can be used to show that the shock thickness scales as $\delta \sim Re_t/Re$ for very fine mesh. Thus, the overall non-conservative effect of the diffusion terms, given by (E.18), is bounded for finite Mach numbers, and a well-behaved solution is expected in the limit of $\Delta x \to 0$.

A similar analysis of the truncation error in (E.13) leads to an integrated effect across the shock

$$\begin{aligned}\frac{\Delta x^2}{24}\frac{1}{Re}\int_{up}^{dn}\rho^{-\frac{2}{3}c_0}\frac{\partial^3}{\partial x^3}\left[\left(\mu+\frac{\mu_t}{\sigma_k}\right)\frac{\partial k}{\partial x}\right]dx &\sim \frac{1}{Re}\frac{\Delta x^2}{24}\rho_{av}^{-\frac{2}{3}c_0}\mu_{av}Re_t\frac{[k]}{\delta^4}\int_{up}^{dn}dx \\ &\sim \frac{\Delta x^2}{24}\frac{Re_t}{Re}M^{1.5}\frac{1}{\delta^3},\end{aligned} \tag{E.19}$$

where the jump $[k]$ across the shock is taken to be order 1 in magnitude (supported by the simulation results presented in the next section), and the average viscosity μ_{av} is assumed to scale as $M^{1.5}$, as earlier. For shock capturing schemes, $\Delta x \propto \delta$ and therefore the above scaling of the truncation error is comparable to the estimate of the non-conservative diffusion term in (E.18), possibly lower by a factor of 1/24. The magnitude of both (E.18) and (E.19) are small compared to convection and production at the shock for realistic combinations of Re and Re_t. The foregoing analysis indicates that the error is also bounded in the limit of infinitely fine grid, and the same can be shown for the ε-diffusion term.

Bibliography

[1] Hoose K. *Hypersonic air-breathing propulsion: The key to affordable nanosatellite launch*. http://www.thespacereview.com/article/3315/1. Accessed: 2019-03-02.

[2] NASA. *What's a Scramjet?* https://www.nasa.gov/missions/research/f_scramjets.html. Accessed: 2019-03-02.

[3] NASA Langley Research Center. *How Scramjets Work?* https://www.nasa.gov/centers/langley/news/factsheets/X43A_2006_5.htmll. Accessed: 2019-08-05.

[4] The Hindu. *ISRO successfully test-fires scramjet engine*. https://www.thehindu.com/news/national/ISRO-successfully-test-fires-scramjet-engine/article14599899.ece. Accessed: 2019-03-02.

[5] Wikipedia. *Scramjet*. https://en.wikipedia.org/wiki/Scramjet. Accessed: 2019-03-02.

[6] Marini M. "Effects of flow and geometry parameters on shock-wave boundary-layer interaction phenomena". In: *8th AIAA International Space Planes and Hypersonic Systems and Technologies Conference*. 1998, p. 1570.

[7] Verma S. B. and Hadjadj A. "Supersonic flow control". In: *Shock Waves* 25.5 (2015), pp. 443–449.

[8] Curran E. T. and Murthy S. N. B. *Scramjet propulsion*. Vol. 189. AIAA, 2001.

[9] Childs M.E., Hijman R., and Miller D.S. "Mach 8 to 22 studies of flow separations due to deflected control surfaces". In: *AIAA* 20 (1964), pp. 312–321.

[10] Marini M. "Analysis of hypersonic compression ramp laminar flows under sharp leading edge conditions". In: *Aerospace science and technology* 5.4 (2001), pp. 257–271.

[11] Mahesh K., Lee S.K., and Moin P. "The interaction of an isotropic field of acoustic waves with a shock wave". In: *Journal of Fluid Mechanics* 300 (1995), 383–407.

[12] Larsson J. and Lele S. K. "Direct numerical simulation of canonical shock/turbulence interaction". In: *Physics of Fluids* 21.12 (2009), p. 126101.

[13] Larsson J., Bermejo-Moreno I., and Lele S. K. "Reynolds-and Mach-number effects in canonical shock–turbulence interaction". In: *Journal of Fluid Mechanics* 717 (2013), pp. 293–321.

[14] Livescu D. and Ryu J. "Vorticity dynamics after the shock–turbulence interaction". In: *Shock Waves* 26.3 (2016), pp. 241–251.

[15] Chen C. H. and Donzis D. A. "Shock–turbulence interactions at high turbulence intensities". In: *Journal of Fluid Mechanics* 870 (2019), 813–847.

[16] Sethuraman Y. P., Sinha K., and Larsson J. "Thermodynamic fluctuations in canonical shock–turbulence interaction: effect of shock strength". In: *Theoretical and Computational Fluid Dynamics* 32.5 (2018), pp. 629–654.

[17] Sinha K., Mahesh K., and Candler G. V. "Modeling the effect of shock unsteadiness in shock/turbulent boundary-layer interactions". In: *AIAA journal* 43.3 (2005), pp. 586–594.

[18] Mahesh K., Sinha K., and Candler G. V. "Modeling shock unsteadiness in shock/turbulence interaction". In: *Physics of Fluids* 15.8 (2003), pp. 2290–2297.

[19] Babinsky H. and Harvey J. K. *Shock wave-boundary-layer interactions*. Vol. 32. Cambridge University Press, 2011.

[20] Davidson P. A. *Turbulence: an introduction for scientists and engineers*. Oxford University Press, 2015.

[21] Wilcox D. C. *Turbulence modeling for CFD*. Vol. 2. DCW industries La Canada, CA, 1998.

[22] Lee J., Taublee D. B., and Holden M. S. "Study of turbulence on supersonic compression surfaces using Reynolds stress model". In: *AIAA Journal* 30.7 (1992), pp. 1738–1746.

[23] Leontiev A. I., Lushchik V. G., and Makarova M. S. "The temperature recovery factor in a boundary layer on a permeable plate". In: *High Temperature* 55.2 (2017), pp. 246–252.

[24] Kurganov V.A. *Adiabatic wall temperature*. http://www.thermopedia.com/content/291/. Accessed: 2019-09-10.

[25] Needham D. and Stollery J. "Boundary layer separation in hypersonic flow". In: *3rd and 4th Aerospace Sciences Meeting*. 1966, p. 455.

[26] Kubota T., Lees L., and Lewis J. E. "Experimental investigation of supersonic laminar, two-dimensional boundary-layer separation in a compression corner with and without cooling." In: *AIAA journal* 6.1 (1968), pp. 7–14.

[27] Holden M. S. “Boundary-layer displacement and leading-edge bluntness effects on attached and separated laminar boundary layers in a compression corner. II-experimental study”. In: *AIAA journal* 9.1 (1971), pp. 84–93.

[28] Spaid F. W. and Frishett J. C. “Incipient separation of a supersonic, turbulent boundary layer, including effects of heat transfer”. In: *AIAA Journal* 10.7 (1972), pp. 915–922.

[29] Elfstrom G. M. “Turbulent hypersonic flow at a wedge-compression corner”. In: ().

[30] Law C. H. “Supersonic, turbulent boundary-layer separation”. In: *AIAA Journal* 12.6 (1974), pp. 794–797.

[31] Coleman G.T. and Stollery J. L. “Heat transfer from hypersonic turbulent flow at a wedge compression corner”. In: *Journal of Fluid Mechanics* 56.4 (1972), pp. 741–752.

[32] Roshko A. and Thomke G. J. “Flare-induced interaction lengths in supersonic, turbulent boundary layers”. In: *AIAA Journal* 14.7 (1976), pp. 873–879.

[33] Settles G. S., Bogdonoff S. M., and Vas I. E. “Incipient separation of a supersonic turbulent boundary layer at high Reynolds numbers”. In: *AIAA Journal* 14.1 (1976), pp. 50–56.

[34] Katzer E. “On the lengthscales of laminar shock/boundary-layer interaction”. In: *Journal of Fluid Mechanics* 206 (1989), pp. 477–496.

[35] Ciani A., Paris S., and Fletcher D. G. “Studies of wall temperature effects on shock-wave / boundary layer interactions in hypersonic flow”. In: *6th International conference on quantitative infrared thermography QIRT 2002*. September 24-27. 2002, pp. 120–125.

[36] Morgan B., Kawai S., and Lele S.K. “A Parametric Investigation of Oblique Shock-wave / Turbulent Boundary Layer Interaction Using LES”. In: 2011-3430. 2011, pp. 1–19.

[37] Childs M.E., Hijman R., and Miller D.S. “Mach 8 to 22 studies of flow separations due to deflected control surfaces”. In: *AIAA* 20 (1964), pp. 312–321.

[38] Bernardini M. et al. “Heat transfer and wall temperature effects in shock wave turbulent boundary layer interactions”. In: *Physical Review Fluids* 1.8 (2016), p. 084403.

[39] Jaunet V., Debieve J. F., and Dupont P. “Length scales and time scales of a heated shock-wave/boundary-layer interaction”. In: *AIAA Journal* 52.11 (2014), pp. 2524–2532.

[40] John B., Kulkarni V.N., and Natarajan G. "Shock wave boundary layer interactions in hypersonic flows". In: *International Journal of Heat and Mass Transfer* 70 (2014), pp. 81–90.

[41] Zhang D., and B. Wang W. Liu, and Su Y. "Numerical simulation on the shock wave/boundary layer interaction with heating/cooling effect". In: *Procedia Engineering* 126 (2015), pp. 194–198.

[42] Kumar V., and A. Hussain M. Nishant, and Kalita P. "Effect of Freestream Parameters on the Laminar Separation in Hypersonic Shock Wave Boundary Layer Interaction". In: *ADBU-Journal of Engineering Technology* 4.1 (2016).

[43] Davis J. P. and Sturtevant B. "Separation length in high-enthalpy shock/boundary-layer interaction". In: *Physics of Fluids* 12.10 (2000), pp. 2661–2687.

[44] Pasha A. A. "Study of Parameters Affecting Separation Bubble Size in High Speed Flows using k-ω Turbulence Model". In: *Journal of Applied and Computational Mechanics* 4.2 (2018), pp. 95–104.

[45] Pasha A. A. and Sinha K. "Shock-unsteadiness model applied to oblique shock wave/turbulent boundary-layer interaction". In: *International Journal of Computational Fluid Dynamics* 22.8 (2008), pp. 569–582.

[46] Gnoffo P. A., Berry S. A., and Van Norman J. W. "Uncertainty Assessments of 2D and Axisymmetric Hypersonic Shock Wave - Turbulent Boundary Layer Interaction Simulations at Compression Corners". In: *42nd AIAA Thermophysics Conference*. Reston, Virigina: American Institute of Aeronautics and Astronautics, 2011.

[47] Raje P. and Sinha K. "A physically consistent and numerically robust k-e model for computing turbulent flows with shock waves". In: *Computers & Fluids* 136 (2016), pp. 35–47.

[48] Settles G.S., Fitzpatrick T.J., and Bogdonoff S.M. "Detailed study of attached and separated compression corner flowfields in high Reynolds number supersonic flow". In: *AIAA journal* 17.6 (1979), pp. 579–585.

[49] Holden M.S. et al. "Experimental studies of shock wave/turbulent boundary layer interaction in high Reynolds number supersonic and hypersonic flows to evaluate the performance of CFD codes." In: *40th Fluid Dynamics Conference and Exhibit*.

[50] HOLDEN M. "Studies of the mean and unsteady structure of turbulent boundary layer separation in hypersonic flow". In: *22nd Fluid Dynamics, Plasma Dynamics and Lasers Conference*.

[51] Pasha A. A. and Sinha K. "Simulation of hypersonic shock/turbulent boundary-layer interactions using shock-unsteadiness model". In: *Journal of Propulsion and Power* 28.1 (2012), pp. 46–60.

[52] Schulein E. "Optical Skin Friction Measurements in Short-duration Facilities (Invited)". In: *24th AIAA Aerodynamic Measurement Technology and Ground Testing Conference*.

[53] Pasha A. A., Vadivelan C., and Sinha K. "Simulation of a practical scramjet inlet using shock-unsteadiness model". In: *28th Shock Waves Symposium* (2011), pp. 1–6.

[54] Mallinson S. G., Gai S. L., and Mudford N. R. "High-enthalpy, hypersonic compression corner flow". In: *AIAA journal* 34.6 (1996), pp. 1130–1137.

[55] Sriram R. and Jagadeesh G. "Correlation for length of impinging shock-induced large separation bubble at hypersonic speed". In: *AIAA Journal* 53.9 (2015), pp. 2771–2776.

[56] Souverein L. J., Bakker P. G., and Dupont P. "A scaling analysis for turbulent shock-wave/boundary-layer interactions". In: *Journal of Fluid Mechanics* 714 (2013), pp. 505–535.

[57] Wilcox D. C. "Formulation of the k-w turbulence model revisited". In: *AIAA journal* 46.11 (2008), pp. 2823–2838.

[58] Pope S. B. *Turbulent flows*. Cambridge university press, 2000.

[59] Launder B. E., Reece G. J., and Rodi W. "Progress in the development of a Reynolds-stress turbulence closure". In: *Journal of Fluid Mechanics* 68.3 (1975), 537–566.

[60] Launder B. E. and Sharma B. I. "Application of the energy-dissipation model of turbulence to the calculation of flow near a spinning disc". In: *Letters in heat and mass transfer* 1.2 (1974), pp. 131–137.

[61] Wright M. J. "A family of data-parallel relaxation methods for the Navier-Stokes equations". In: (1997).

[62] Steger J. L. and Warming R. F. "Flux vector splitting of the inviscid gasdynamic equations with application to finite-difference methods". In: *Journal of computational physics* 40.2 (1981), pp. 263–293.

[63] Hirsch C. *Numerical computation of internal and external flows*. Wiley, 1997.

[64] LeVeque R. J. *Finite volume methods for hyperbolic problems*. Vol. 31. Cambridge university press, 2002.

[65] Culbert B. L. *Computational Gasdynamics*. Cambridge University Press, 1998.

[66] Sinha K. and Balasridhar S. J. “Conservative formulation of the k-e turbulence model for shock–turbulence interaction”. In: *AIAA journal* 51.8 (2013), pp. 1872–1882.

[67] Bookey P. et al. “New experimental data of STBLI at DNS/LES accessible Reynolds numbers”. In: *43rd AIAA Aerospace Sciences Meeting and Exhibit*. 2005, p. 309.

[68] Holden M. S. et al. “Measurements in Regions of Shock Wave/Turbulent Boundary Layer Interaction with Large Shock Generator/Hollow Cylinder and Hollow Cylinder/Cavity Configurations at Mach Numbers between 5 and 7 at Flight Matched Enthalpies and in Cold Flows”. In: *22nd AIAA International Space Planes and Hypersonics Systems and Technologies Conference*. 2018, p. 5198.

[69] Settles G. S. and Bogdonoff S. M. “Scaling of two-and three-dimensional shock/turbulent boundary-layer interactions at compression corners”. In: *AIAA Journal* 20.6 (1982), pp. 782–789.

[70] Kuehn D. M. “Experimental investigation of the pressure rise required for the incipient separation of turbulent boundary layers in two-dimensional supersonic flow”. In: (1959).

[71] *ATMOSPHERE PROPERTIES*. http://www.braeunig.us/space/atmos.htm. Accessed: 2019-03-02.

[72] Arora N. et al. “Flowfield Measurements in a Mach 2 Fin-Generated Shock/Boundary-Layer Interaction”. In: *AIAA Journal* 56.10 (2018), pp. 3936–3974.

[73] Tennekes H. and Lumley J. L. *A first course in turbulence*. MIT press, 1972.

[74] Van Driest E. R. “Turbulent Boundary Layer on a Cone in a Supersonic Flow at Zero Angle of Attack”. In: *Journal of the Aeronautical Sciences* 19.1 (1952), pp. 55–57.

[75] Roy C. and Blottner F. “Review and assessment of turbulence models for hypersonic flows: 2D/asymmetric cases”. In: *44th AIAA Aerospace Sciences Meeting and Exhibit*. 2006, p. 713.

[76] Nagaraj B. and Zakiuddin M.D. “Effect of Reynolds Number and Wall Temperature on Shock Wave / Boundary Layer Interaction”. In: *International Journal & Magazine of Engineering, Technology, Management And Research* 3.10 (2016), pp. 527–539.

Acknowledgements

I hereby acknowledge the support and guidance provided to me by my guide Prof. Krishnendu Sinha . I would like to convey my sincere thanks for the continuous support of the PhD work and related research work, for the patience, motivation and guidance. His guidance has played an important role in research work and writing of this thesis.

I would also like to thank the faculty members of the research progress committee - Prof. Amitabh Bhattacharya and Prof. Avijit Chatterjee. Their involvement in the yearly discussions, their feedback and their suggestions has been pivotal in bringing about a depth in the development of this work.

I am very thankful to all my friends in lab for providing me their untiring support in the research and compilation of this work.